Alma Mater Studiorum
Università di Bologna

SCUOLA DI SCIENZE
Corso di Laurea Magistrale in Astrofisica e Cosmologia
Dipartimento di Fisica e Astronomia

MULTI-FREQUENCY RADIO CONTINUUM OBSERVATIONS OF BROAD ABSORPTION LINE QUASARS

Candidato:
Marisa Brienza

Relatore:
Prof.ssa Loretta Gregorini

Co-relatore:
Dr. Karl-Heinz Mack
Dr. Gabriele Bruni

Anno Accademico 2012-2013

Sessione I

This thesis work was done as part of the research activity of the Istituto di Radioastronomia - INAF and the Italian ALMA Regional Centre, in collaboration with Dr. Arturo Mignano and Dr. Rosita Paladino.

Abstract

About 20% of the observed quasar (QSO) population shows Broad Absorption Lines (BALs) in their UV-optical spectra, regularly connected to resonance emission lines. The blueshifts and the widths of these troughs are interpreted as the evidence of high-velocity wind-like outflows along the line of sight, which can even reach few percent of the light speed and are probably associated to the central supermassive black hole accretion phenomenon. Understanding the details of this ejection mechanism would thus be a crucial step towards the comprehension of the physics of the central engine of quasars. These phenomena probably also play a fundamental role in removing angular momentum from the gas, allowing a continuous accretion process. Moreover, these outflows carry mass, momentum and energy into the surrounding medium, and therefore they may also be important to better understand the Active Galactic Nuclei (AGN) feedback on the overall host galaxy evolution process. Nowadays, in fact, the potential impact of quasars outflows on their environment has widely been recognized, starting from the enrichment of the IGM, to cluster cooling flows and star formation processes.

There is still no consensus about the origin of the absorbing gas in BAL QSOs, the mechanism which accelerates it, or the relationship between BAL QSOs and the quasar population as a whole. Over the years the debate on their nature has concentrated on two different scenarios. An orientational approach suggests that all QSOs present these outflows, but they only manifest their presence when observed along a particular line of sight (orientation scenario - Elvis 2000, Punsly et al. 1999). Alternatively, BAL QSOs could represent a short, primordial phase of the QSO life (evolutionary scenario - Briggs et al. 1984). In this case the newborn QSO would still be expelling its dust cocoon while transforming into a normal QSO.

Until recently, astronomers were convinced that BALQSOs were only associated to radio-quiet AGN (Stocke et al. 1992). Thanks to the extended radio survey projects of the last decade it has become plain that, contrary to some previous observations, radio-loud BAL QSOs exist, although in small percentage, and share quite the same characteristics of ’normal’ radio-loud QSOs (Becker et al. 1997, 2000). In this context the study of BAL QSO radio emission can be used as an additional diagnostic tool to explore the dichotomy.

In fact, it can be crucial to constrain some source properties such as age, magnetic field, local column density and orientation providing new means of interpretation. A complete description of the BAL QSOs population is presented in Chapter 2.

In this thesis we worked on a Radio-Loud BAL QSO sample and an equivalent comparison sample of Radio-Loud non-BAL QSO both selected by Bruni et al. (2012). In particular, the samples consist of 25 BAL QSOs and 34 non-BAL QSO chosen from the 4th edition of the Sloan Digital Sky Survey (SDSS) QSOs catalogue. More details about the sample selection and the previous work on the samples are presented in Chapter 3.

Here we perform a full polarization continuum study exploiting both sigle-dish and interferometric observations at various frequencies (see Chapter 4 for a full description).

The principal investigation performed in this thesis concerns a spectral ageing analysis of both the BAL and the non-BAL sample. One way to characterize the sources and possibly disantangle the two population of quasars would be in fact to measure the age of their radio emission. The power-law synchrotron spectrum of a radio source is generated by a distribution of electrons emitted by the central engine through two polar jets and then partly deposited in two lobes. Although in first approximation the radiative losses of the electrons always cause a steepening of the power law spectrum, the precise trend of the high-frequency tail is indicative of a peculiar energy input evolution within the source. Moreover, by measuring the so-called break frequency an estimate of the age of the electrons population can be inferred. Making use of the multi-frequency radio campaign by Bruni et al. (2012) and of the flux densities measured during this work, we constructed the Spectral Energy Distribution (SED), in the GHz range, for all sources and performed spectral fitting using various models. For sources showing a break frequency we then computed the spectral age. The results of this analysis show other then firm indications in favor of an evolutionary scenario. The comparison between BAL QSO and non-BAL QSO samples does not reveal in fact any evident difference in their age distribution, both showing typical ages of young sources.

In addition to that, when multi-epoch observations were available, the radio variability properties of the sources were also investigated. Nowadays it is generally accepted that radio flares in AGN can be present when shocks propagate in the relativistic jets and have typical timescales of 1-2 years. Moreover, if the line of sight is close to the object axis of symmetry, Doppler-beaming effects can greatly amplify the variability intensity. This would thus be a method to check the orientation of the studied sources. Once again no clear indication is present able to clarify the dichotomy. Very low flux density variations are actually observed for both samples. The entire analysis is discussed in Chapter 5

Sinossi

Circa il 20% della popolazione dei quasar osservati (QSO) presenta nello spettro ottico-UV larghe righe di assorbimento (Broad Absorption Lines, BALs) regolarmente connesse a righe di risonanza in emissione. A causa del loro blushift e della loro larghezza questi assorbimenti sono comunemente attribuiti a forti venti e outflow lungo la linea di vista. Essi possono raggiungere, nei casi più estremi, velocità di qualche per cento della velocità della luce e si rintengono essere associati al processo di accrescimento del buco nero centrale. Per questo motivo, indagare i dettagli riguardanti il fenomeno di espulsione di materia risulta cruciale per una completa comprensione della fisica dell'accrescimento. Inoltre, depositando energia e materia all'interno dell'ambiente circostante, essi avrebbero un ruolo chiave nei fenomeni di feedback sul processo di evoluzione dell'intera galassia ospite. E' attualmente accertato, infatti, il forte impatto che questi fenomeni avrebbero sul mezzo circostante, a partire dall'arricchimento del Mezzo Intergalattico, ai 'cooling flow' negli ammassi di galassie, al processo di formazione stellare.

Al giorno d'oggi non si è ancora raggiunto un consenso circa l'origine del gas responsabile di questi assorbimenti, i meccanismi in gioco per accelerarlo e la loro relazione con i quasar 'normali'. Nel corso degli anni il dibattito circa la loro natura si è concentrato su due differenti scenari. Da un lato, è stato suggerito che l'elemento chiave per l'interpretazione dei BAL QSOS sia la loro orientazione. In particolare, si potrebbe pensare che tutti i quasar siano soggetti a questo tipo di fenomeno ma che esso possa essere notato dagli spettri solo se il QSO viene osservato lungo una particolare linea di vista. Usando un diverso approccio, i BAL QSO potrebbero rappresentare una breve fase primordiale della vita del quasar. In questo scenario evolutivo, il quasar nascente starebbe ancora espellendo il guscio di polveri e gas da cui si sarebbe creato (es. Briggs et al.1984).

Fino a non troppo tempo fa, esisteva la generale convinzione che i BAL QSO fossero solo associati ad AGN radio-quieti (Stocke et al. 1992). Grazie alle vaste survey radio effettuate nell'ultimo decennio però, si è scoperto che BAL QSOs radio-loud esistono, sebbene in piccola percentuale ($\sim$ 15%, Becker et al. 2000). In questo contesto, lo studio dell'emissione radio dei BAL QSO può essere utilizzata come ulteriore strumento diagnostico per esplorare questa dicotomia. Infatti, questa può essere utilizzata per caratterizzare molte proprietà delle sorgenti come l'età, i campi magnetici, la densità di colonna, fornendo

nuovi spunti per interpretazioni. Una descrizione completa della popolazione di BAL QSO allo stato attuale è presente nel Capitolo 2.

In questo lavoro di tesi si è lavorato su un campione di BAL QSOs radio-loud ed un corrispettivo campione di riferimento, selezionati da Bruni et al. (2012). In particolare i due campioni consistono rispettivamente di 25 BAL QSOs e 34 non-BAL QSOs scelti all'interno della quarta edizione del catalogo di QSO della Sloan Digital Sky Survey (SDSS). I dettagli sulla selezione del campione e sui precendi studi effettuati può essere trovata nel Capitolo 3.

Durante questo lavoro abbiamo condotto uno studio radio continuo in full polarization sfruttando dati provenienti sia da strumenti a singola parabola sia interferometrici (vedere Capitolo 4 per i dettagli). La principale analisi condotta durante questa tesi riguarda lo studio dell'età spettrale delle sorgenti presenti nei due campioni precedentemente descritti. Un modo per indagare le differenze tra le due categorie di oggetti e dare supporto ad uno dei due scenari prima illustrati, sarebbe quello di indagarne le caratteristiche spettrali ed in particolare misurare le età dell'emissione radio. Lo spettro di sincrotrone osservato nelle radiosorgenti è generato da una distribuzione di elettroni accelerati nelle regioni centrali dell'AGN. Sebbene in prima approssimazione le perdite radiative degli elettroni nel tempo causino un irripidimento della legge di potenza alle alte frequenze, la forma esatta di questo ultimo è indicativo di un particolare rifornimento di energia all interno della sorgente. Misurando la frequenza al quale avviene il cambio di pendenza - la *frequenza di break* - è possibile inoltre avere una stima dell'età della popolazione di elettroni. Facendo uso dei dati raccolti da Bruni et al. (2012) e delle densità di flusso misurate durante questo lavoro, si sono costruiti le SED delle sorgenti in questione e si sono fittati con diversi modelli spettrali. Quando possibile è stata quindi stimata l'età radiativa della sorgente. I risultati dell'analisi mostrano tutt'altro che informazioni chiare in direzione di uno scenario. Il confronto tra BAL QSOs e non-BAL QSOs non porta alla luce nessuna importante differenza nella distribuzione delle età che risultano in entrambi i casi quelle tipiche di radio sorgenti giovani.

Avendo inoltre a disposizione osservazioni multi epoca, sono state indagate le proprietà di variabilità delle sorgenti in questione. Al momento attuale è generalmente diffusa l'idea che brillamenti radio possano presentarsi a seguito di shock all'interno dei getti relativistici su scale tipiche di 1-2 anni. Se la linea di vista dell'osservatore è allineata all'asse di simmetria dell'AGN effetti di beaming possono inoltre amplificare notevolmente queste variazioni di luminosità. Alla luce di ciò, lo studio delle variazioni radio può fornire indicazioni sull'orientazione delle sorgenti in questione. Ancora una volta non è presente alcuna indicazione chiara che permetta di distinguere le due popolazioni. Per entrambi i campioni sono osservate solo lievi variazioni di luminosità. L'intera analisi è illustrata nel Capitolo 5.

Contents

Chapter 1

Active Galactic Nuclei

At present it is generally believed that all kinds of galaxies contain in their nuclear region a supermassive black hole of $10^6 - 10^{10} M_\odot$. The origin of these objects represents a crucial cosmological issue but still remains under debate. Some of these black holes are thought to accrete material from the surrounding medium, releasing this way a huge amount of energy of the order of $10^{11} - 10^{14} L_\odot$, well above the normal galaxy power produced by its own stellar populations, including an ordinary supernovae activity. This kind of galaxies, with such extreme bolometric luminosities, are said to host an Active Galactic Nucleus (AGN). The study of this phenomenon is of great interest, not only to understand the structure of the galaxy nucleus itself but also in terms of feedback on the parent galaxies. Indeed it is now almost clear that the AGN plays a key role in the overall galaxy evolution process, having a direct impact on the surrounding medium. The strict correlation between the black hole mass and the bulge mass (Magorrian et al. 1998; Ferrarese & Merritt 2000) is thought to be one of the clearest evidence of this link. For the current model, energy is generated by gravitational infall of material which is heated to high temperature in a dissipative accretion disc lying around the black hole. Because of the conservation of the angular momentum, the gas orbiting around the black hole distributes in a disk-like shape. The rate, at which the potential energy of the infalling material can be converted to radiation, is given by

$$L \approx \frac{dU}{dt} = \frac{d}{dt}\frac{GMm}{r} = \frac{GM}{r}\frac{dm}{dt} = \frac{GM\dot{M}}{r} \tag{1.1}$$

where GMm/r is the potential energy of a mass m at a distance r from the central source of mass M. The efficiency factor of mass-energy conversion is very uncertain and depends on the details of the accretion phenomenon itself, however, in first approximation a value of $\eta = 0.1$ is often used. The maximum luminosity the system can reach is called Eddington Luminosity whose expression can be easily obtained comparing the gravitational force with the outward radiation force:

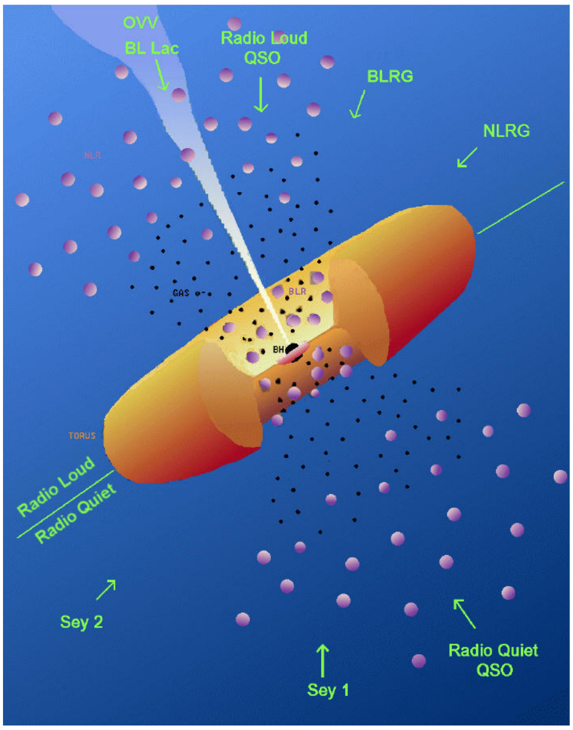

Figure 1.1: Representation of the Unified AGN model by Urry & Padovani (1995)

$$L_E = \frac{4\pi G c m_p}{\sigma_e} M \tag{1.2}$$

where σ_e is the Thomson scattering cross-section. If this luminosity is exceeded, the radiation pressure is strong enough to halt the accretion mechanism or even to destroy the disc.

In order to explain the variety of AGN observational properties studied in the last decades, astronomers have built up a model, the so-called *Unified Scheme* (Urry & Padovani 1995), which describes the AGN structure and tries to reproduce the observational properties found, by playing on variables like the black hole mass, the accretion rate, the magnetic field and the line of sight. A representation of this model is shown in Fig. 1.1.

In this picture the black hole is surrounded by an accreting disc whose emission is constituted by the superposition of black body spectra with different temperatures around 10^6 K. The gas in the disc has indeed different temperatures depending on its distance from the black hole and will emit in every band of the electromagnetic spectrum: in X-ray from the innermost parts and in the radio band from the more external layers.

From the edge of the disc ($\sim 0.1 pc$) an absorbing toroidal structure starts, composed by dense molecular clouds and dust with typical temperatures of $\sim 10^3$ K and densities of 10^7 cm^{-3}. It is not clear yet whether it consists of a smooth dust distribution, whose temperature is only function of the distance from the central source or whether different dust temperatures coexist at the same distance from the radiation source. In any case, dust is thought to intercept some fraction of radiation produced by the disk and re-emitting it in the infrared.

Orbiting close to the central engine (distances < 1 parsec) there is a gas clouds system called Broad Line Region (BLR), responsible for the broad line emission features in AGN optical spectra. The widths of these lines are much higher than the ones expected by only thermal excitation which is interpreted as due to turbulent gas motions (~ 3000 km s^{-1}), thus giving information on the gas dynamics in the innermost regions of the AGN. Here the density should be so high, n $> 10^8$ cm^{-3}, to prevent the formation of forbidden lines which are indeed not seen in observed spectra. The BLR can provide useful probes of the central black hole first of all because the gas exciting source is actually the continuum of the central engine. This is clear by observing that an intensity variation of the continuum produces, with some delay, a variation in the broad lines too. From the observed temporal delay one can deduce the BLR dimensions of the order of 1 parsec. Another important aspect is that bulk motions in the BLR are almost certainly determined by the central source, with gravity and radiation pressure competing. From this we can get information about the mass of the black hole itself.

Moving away from the nuclear region, the medium changes its properties and it is now called Narrow Line Region (NLR), always referring to the line width of the optical spectrum. Here the gas density is much lower, typically $n_e = 10^3 - 10^6$ cm^{-3}, allowing the production of forbidden lines. Since no variability in the lines coming from this region has ever been observed, one deduces that it is much more extended (100-1000 pc). This is actually the only region to be optically resolved and shows, contrary to expectation, an anisotropic morphology, the ionization cones, regardless of the presence of polar jets.

The AGN emission extends over the whole electromagnetic spectrum from the radio band to gamma rays. In Figure 1.2 a theoretical AGN continuum is shown which is the sum of the emissions of the substructures previously described. Starting from lower frequencies we find in red the thermal dusty torus emission whose peak lies at 10 micron, then in blue the black body superposed emission originated in the accretion disc which presents a detection gap due to the high opacity of the Milky Way interstellar medium. In the X-band we have the contribution of the hot corona which seems to be a region of ionized and optically thin gas at very high temperature ($T = 10^8 - 10^9 K$) just overlying the disc. This gas produces a comptonization of the thermal photons coming from the disc which then in part leave the AGN more energetic and in part fall back on the disc where they are then reflected.

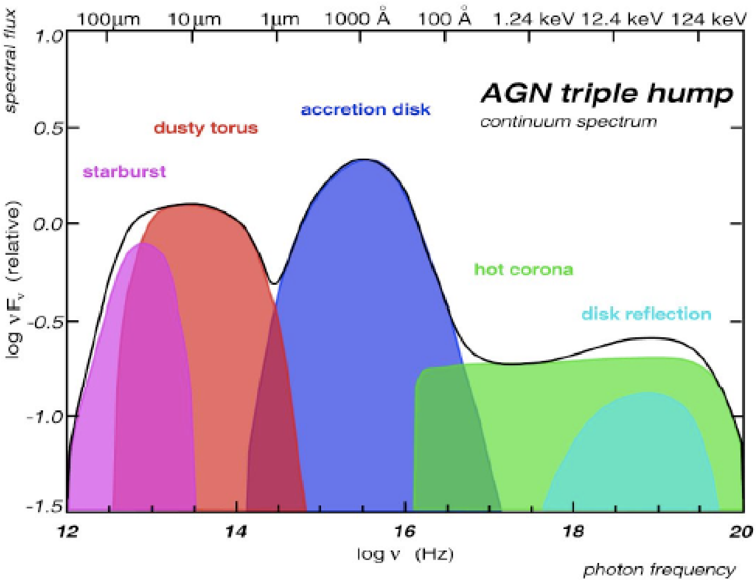

Figure 1.2: Theoretical AGN spectral energy distribution. Different colours represent the various emission contributions as specified in figure.

1.1 Radio-loud AGN

About 10% of the totality of the AGN population also shows some non-thermal radio emission from which the distinction radio-loud or radio-quiet AGN is defined. Kellermann et al. (1989) first defined the two categories on the basis of the ratio between radio and optical emission, naming radio-loud AGN those objects whose radio luminosity at 5 GHz was at least ten times greater than the optical luminosity in B band (445 nm). Within this category the first big morphological classification is made between extended radio sources and core-dominated radio sources. At present, astronomers think that the origin of the wide radio structures seen in the first category lies in two jets of relativistic particles and magnetic fields which are in turn generated in the inner regions of the accreting disc and expand in polar directions collimated by the strong magnetic field. In this way, charged particles are accelerated by the Lorentz force and as a consequence irradiate synchrotron radiation. The physical mechanism at the origin of the jets is a difficult and controversial issue and it is probably linked to the spin of the black hole. In the powerful cases these jets can expand for even some Mpc, well beyond the associated optical source. When they impact on the Intergalactic Medium, a shock is created, which amplifies the magnetic field and thus the emission. These edge-brightened regions are called hot spots. As the accelerated particles diffuse, two extended ellipsoidal regions, called lobes, are created around the jets. The weaker the jets the more they will interact with the surrounding medium and will lose energy during their path thus creating distorted and extended lobes. An example of these kind of emissions is shown in Fig. 1.3.

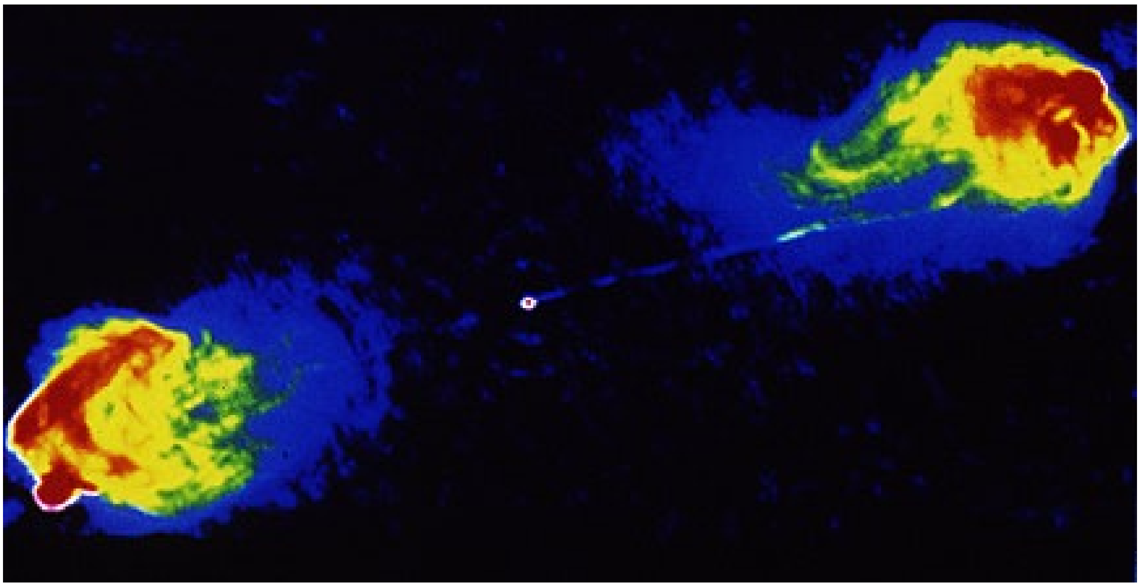

Figure 1.3: Radio image of Cygnus A showing twin radio lobes stretching 50 kpc from the nucleus. Jets and hot-spots are also evident. The most of the emission comes from the hotspot (red) in particular at the boundary where the jets impact on the surrounding medium and shocks are created (white).

As seen from Figure 1.1, depending on the line of sight, the observer will intercept only some of the substructures previously described and will find this way a variety of different morphologies actually for the same kind of object. A general classification of AGN is :

- Seyfert Galaxies: spiral galaxies with strong IR, UV, X-ray spectra but weak radio emission. They are classified depending on the emission lines present in their optical spectra:
  - type 1 objects present broad emission lines and narrow forbidden lines that means the observer is intercepting both the BLR and the NLR.
  - type 2 objects present both permitted and forbidden narrow lines and no broad emission lines that means the observer is looking through the dusty torus which obscures the BLR and probably attenuates the continuum emission.
- Radio Galaxies: generally elliptical galaxies with a high radio power $P_{1.4GHz} = 10^{23} - 10^{28}$ Watt/Hz seen from an equatorial point of view. Depending on their power and morphology they are classified in two different categories FRI and FRII, from Fanaroff and Riley (1974) who first defined that.
  - FRI radiogalaxies have $P_{1.4GHz} < 10^{24.5}\ Watt/Hz$, they present bright jets, symptom of an inefficient transport mechanism and extended and distorted lobes.

  - FRII radiogalaxies have $P_{1.4GHz} > 10^{24.5}\ Watt/Hz$ they present weak and well collimated jets and also well-aligned lobes with bright and compact hot spots.

- Blazars are radio-loud AGN with relativistic jets oriented close to the observers line of sight. This perspective should explain the observed characteristics like the rapid variation of the luminosity and superluminal motions.

- Quasars are the most powerful AGN and can be both radio-quiet and radio-loud. Their emission is always dominated by a very compact nuclear region which is often not resolved by terrestrial telescopes (<1").Their power is so high to hide the host galaxy, making them appear as point-like source from which the name Quasi Stellar Radio Sources (Quasars) originates. Based on the unification model (Urry & Padovani 1995), radio-loud quasars can be considered the beamed counterparts of FR II type galaxies, viewed at small angles towards the observer. Typically they are seen with an angle comprised between 5 and 45 degrees from the pole.

1.1.1 Synchrotron emission

As explained before, about 10% of the observed QSO population is classified as radio-loud sources. The broad band radio spectra of these objects are typically well represented by non-thermal power law spectra. Because of the presence of intrinsic magnetic fields and relativistic particles, the main emission mechanism in action in radio sources is thought to be the synchrotron mechanism.

When charged particles move in a magnetic field $\vec{B}$, they are accelerated by the Lorentz force whose expression is:

$$\frac{d\vec{p}}{dt} = e(\frac{\vec{v}}{c} \times \vec{B}) \tag{1.3}$$

where $\vec{p} = \gamma m_0 \vec{v}$ is the particle momentum, γ is the Lorentz factor, e, $\vec{v}$ and m_0 are the particle charge, velocity and rest mass and $\vec{B}$ is the magnetic field. The parallel and perpendicular components are:

$$F_{L||} = e\frac{v_{||}}{c}B = 0 \longrightarrow a_{||} = 0 \tag{1.4}$$

$$F_{L\perp} = \gamma m_0 \frac{d\vec{v_\perp}}{dt} = e\frac{v_\perp}{c}B \longrightarrow a_\perp = \frac{evBsin\theta}{\gamma m_0 c} \tag{1.5}$$

Here θ denotes the angle that the velocity vector makes with the magnetic field lines which is called *pitch angle*. Eq. 1.4 represents a uniform motion along the field lines of the magnetic field, Eq. 1.5, on the other hand, indicates a circular motion with constant velocity $v_\perp$. The radius and pulsation of this orbit can be written in the following way:

$$r_L = \frac{\gamma m_0 c\beta}{eB} v_\perp \tag{1.6}$$

$$\omega_L = \frac{2\pi}{T_L} = \frac{eB}{m_0 c} \tag{1.7}$$

The total trajectory of the particle will thus be helicoidal with propagation axis parallel to the field lines of $\vec{B}$, radius equal to the Larmor radius r_L and pulsation equal to ω_L.

From the electromagnetism theory it is known that when a charged particle is accelerated, it creates a radiation field by losing part of its own energy. The power irradiated by the particle is given by the Larmor formula which, in case of relativistic energies, is:

$$w(t) = \frac{2}{3}\frac{e^2}{(m_0^2 c^3)}\gamma^2 \left(\frac{d\vec{p}}{dt}\right)^2 \tag{1.8}$$

Note that, since the difference in mass between electrons and protons is in the order of 10^3, electrons will irradiate 10^6 times more than protons, other things being equal. For this reason synchrotron emission in radio sources is attributed mostly to electrons. Substituting $a_\perp$ in Eq. 1.8 one gets:

$$w_s(E) = \frac{2}{3}\frac{e^4}{m_0^2 c^5}\gamma^2 v^2 (Bsin\theta)^2 = C_E E^2 (Bsin\theta)^2 \tag{1.9}$$

which is the synchrotron power produced by a single electron in the magnetic field $\vec{B}$, where $\gamma = E/m_0 c^2$ and $C_E = 2.37 \cdot 10^{-3}$ in c.g.s. units.

The spectral distribution, i.e. the synchrotron emission per unit frequency, of a single electron can be obtained by mean of a Fourier analysis of the impulse. The final spectrum is made by the superposition of all the harmonica and extend until a critical frequency ν_c defined as:

$$\nu_c \equiv \frac{3}{2}\nu_s sin\theta \tag{1.10}$$

where ν_s is the typical synchrotron frequency. Talking about non-relativistic particles, ν_s would simply indicate the inverse of the revolution period of the electron itself. Instead, when $\vec{v}$ gets close to the light speed, ν_s represents the inverse of the time interval, for each orbit, during which the radiation reaches the observer. Because of the aberration of light indeed, half of the radiation is emitted in a cone of semi-aperture angle $1/\gamma$ called beaming angle. The expression of ν_s is the following:

$$\nu_s = \gamma^2 \frac{eB}{2\pi mc} \tag{1.11}$$

For $\nu \ll \nu_c$ the irradiated power $w_s(E,\nu)$ is $\propto (\nu/\nu_c)^{1/3}$ and does not contribute much to the total power.

For $\nu \gg \nu_c$ the irradiated power $w_s(E,\nu)$ is $\propto (\nu/\nu_c)^{1/2} exp(-\nu/\nu_c)$ rapidly declining.

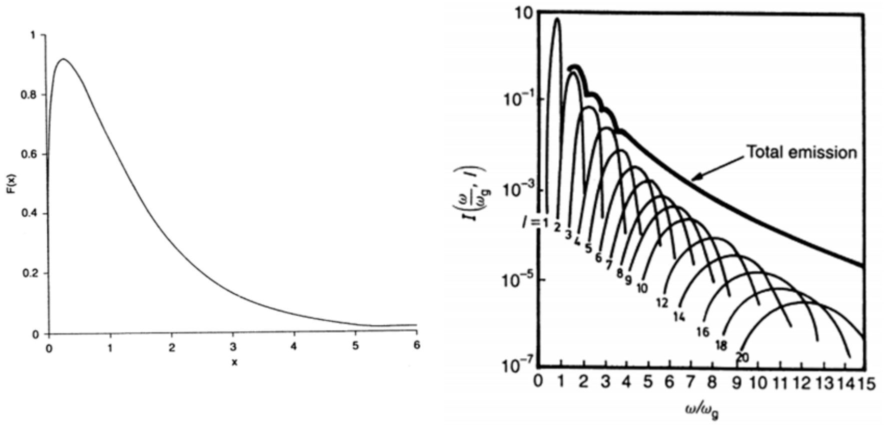

Figure 1.4: Power spectrum produced by a single electron as the result of superposition of Fourier harmonicas.

What is actually interesting from an astrophysical point of view is the total emission of an electron distribution. If no absorption mechanisms are present within the source and particle emissions can be considered independent from the emission of other particles, the total power emitted by the electron population is the convolution of the emission spectrum of a single electron with the energy distribution of all particles:

$$S(\nu)d\nu = \int_{E_1}^{E_2} w_s(E,\nu) \cdot N(E)dE \tag{1.12}$$

where N(E)dE is the number of particles per unit volume having energy in the range $E_1 - E_2$ and w_s(E, ν) is the power spectrum of the single particle.

If the energy particle distribution is assumed to be a power-law

$$N(E)dE = N_0 E^{-p} dE \tag{1.13}$$

then the total emissivity per unit frequency is:

$$S(\nu) \propto B_{\perp}^{\alpha} \nu^{-\alpha} \tag{1.14}$$

where the spectral index α is

$$\alpha = \frac{p-1}{2} \tag{1.15}$$

It can be noticed that a power-law energy distribution of electrons produces a power-law spectrum and that the two spectral indices are related. On the contrary, the emission

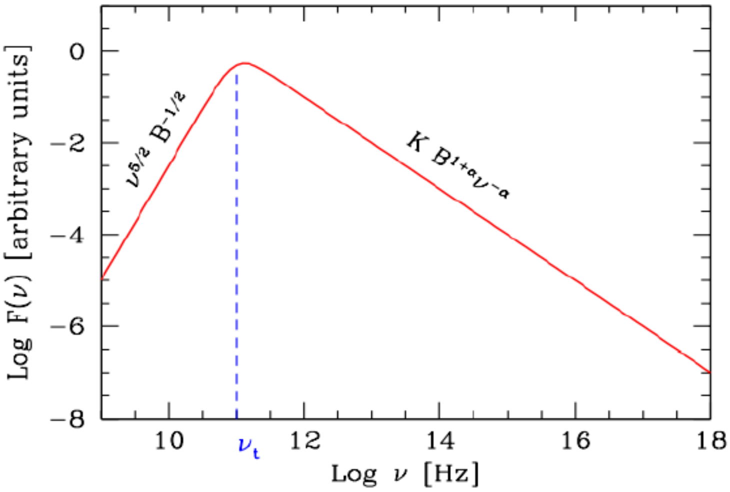

Figure 1.5: Self-absorbed theoretical spectra. The optically thin region has a power-law trend with spectral index α as suggested by the synchrotron emission mechanism while the optically thick region presents a sharp decline with index = 2.5.

produced by an electron population results to be totally independent from the radiation distribution of a single particle.

The observed AGN spectra are actually more complicated than a simple power-law. This happens because of several phenomena that can alter the particle conditions. A decrease in power at low and high frequencies as shown in Fig. 1.7 is commonly observed. The two phenomena responsible for these drops in the power law are thought to be synchrotron self-absorption (SSA) and particle ageing.

Sychrotron self-absorption

Until now we have assumed that electrons are transparent to their own radiation. This does not happen if the intensity of synchrotron radiation within the source becomes sufficiently high and the source brightness temperature approaches the kinetic temperature of the electrons In this situation the same electrons responsible for the emission will begin to absorb part of their own synchrotron radiation causing an appreciable decrease of the source luminosity. Since the opacity τ of a relativistic plasma increases as the frequency decreases, self-absorption is a typical feature of low frequencies. As a consequence of this phenomenon the source radio spectra can present an emission peak at a certain frequency called ν_{peak} which represents the border between the optically thin ($\tau < 1$) and optically thick ($\tau > 1$) regimes of the medium. Photons with frequencies smaller than ν_{peak} are actually absorbed and do not contribute to the source luminosity anymore (see Fig. 1.5).

If the synchrotron mechanism was a thermal process one could easily calculate the absorption coefficient by means of the Kirchhoff's law. Since the distribution of the relativistic electrons is almost never Maxwellian, this cannot be done. To make things easy, one can anyway think of power law energy distribution of the electrons as a superposition of Maxwellians, of different temperatures. In this way one can relate the energy $\gamma c^2 m$ of a given electron to the energy kT of a Maxwellian. One can write then:

$$kT \approx \gamma c^2 m \approx c^2 m \left(\frac{\nu}{\nu_L}\right)^{1/2} \tag{1.16}$$

For an absorbed source the brightness temperature T_b, defined by

$$I(\nu) \equiv 2kT_b \frac{\nu^2}{c^2} \tag{1.17}$$

must be equal to the "kinetic temperature" of the electrons, and so

$$I(\nu) \approx 2kT_b \frac{\nu^2}{c^2} \approx c^2 m \left(\frac{\nu}{\nu_L}\right)^{1/2} \propto \frac{\nu^{5/2}}{B^{1/2}} \tag{1.18}$$

This means that, independently of the electron energy distribution, the absorbed spectrum always has a slope $\propto \nu^{5/2}$.

Now, integrating $I(\nu)$ over the angular dimension of the source (i.e. θ), one gets the flux density which thus shows the following dependencies:

$$F(\nu) \propto \theta^2 \frac{\nu^{5/2}}{B^{1/2}} \tag{1.19}$$

From the previous expression it is clear that the smaller the source is the higher the Synchrotron Self-Absorption (SSA) i.e. the peak frequency is. A self-absorbed spectrum is thus quite always indication of compact radio sources. Moreover, if one could observe a self-absorbed source, of known angular size, one could then derive its magnetic field even without knowing its distance. The frequency ν_{peak} at which the brightness reaches its maximum can be written as:

$$\nu_{peak} \propto I_{max}^{2/5} \theta^{-4/5} B_{\perp}^{1/5} (1+z)^{1/5} \tag{1.20}$$

It is worthwhile noting that no absolute reason exists for considering the SSA the only mechanism causing self-absorption. In principle, the free-free absorption (FFA) could be likewise responsible for the turnover in radio sources spectra (Bicknell et al. 1997). In this case though, we should assume that the local Interstellar Medium (ISM) has a density and ionization level sufficiently high to permit the FFA to play an important role. To support this scenario, shocks created by lobe and jet expansions into the ISM are taken in consideration as responsible for the high ionization level and density required.

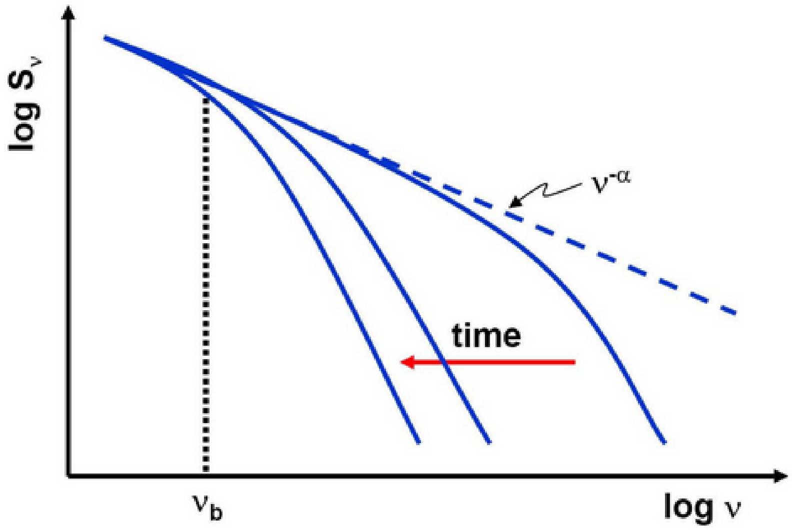

Figure 1.6: Representation of the synchrotron spectral evolution with time. Assuming no injection mechanisms in action, the break frequency moves as time passes to lower frequencies.

Spectral ageing

Another spontaneous phenomenon which contributes to the modification of the power-law shape of the synchrotron spectrum is particle ageing. In fact, as time passes, electrons lose part of their energy by emitting synchrotron radiation. In this case, the energy distribution N(E) of the electron population and, consequently, the radiation spectrum transforms. As the electrons lose their energy they will be less accelerated by the Lorentz force, i.e. they will emit at lower frequencies, causing a drop in the spectral distribution with respect to the power-law. Since the most energetic electrons lose energy first (see Eq. 1.9), the high-frequency region of the spectrum first undergoes a steepening. The frequency at which the change of index in the power-law radiation distribution is observed is commonly called *break frequency* (ν_b).

We now consider a population of particles confined in a region in which a constant and uniform magnetic field is present. Assume then, that the region is not expanding and that no fresh particles are injected. We thus only consider radiative losses. In this situation we can integrate the Eq. 1.9, which describes the radiative losses of a single particle via synchrotron emission, obtaining:

$$E(t) = \frac{E_0}{1 + c(Bsin\theta)^2 t E_0} = \frac{E_0}{1 + E_0/E_b} \tag{1.21}$$

where E_0 is the particle energy at an initial time t_0 and E_b is the *break energy* which represents the maximum energy a particle can have at a certain time t:

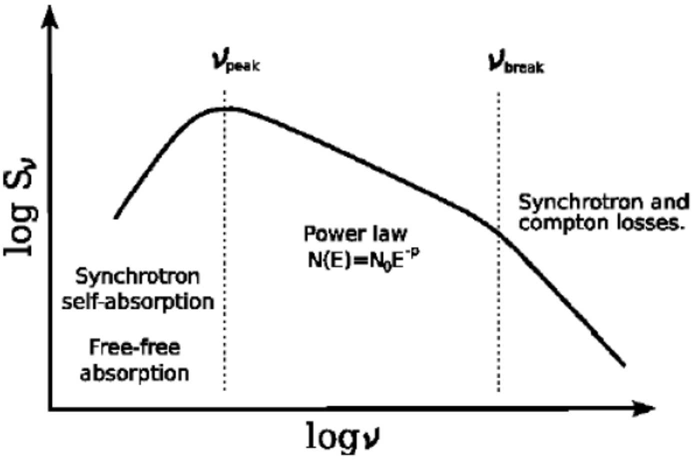

Figure 1.7: Theoretical synchrotron spectrum showing self-absorption at low frequencies and spectral ageing at high frequencies.

$$E_b = \frac{1}{C_E(Bsin\theta)^2t} \tag{1.22}$$

Eq. 1.21 describes how the energy of a particle is modified with time. It is important that at any time $t > t_0$ the particle has an energy $E(t) < E_b$. Moreover, since the break energy does not depend on E_0, whatever the initial particle energy distribution is, one knows for sure that at a certain time t every particle will have an energy smaller than E_b.

As shown in Fig. 1.6, as time passes, ν_b moves at lower frequencies. Just for this reason studying its value one can constrain the age of the electron population. Note that the magnetic field plays a crucial role in particle ageing as well, accelerating the steepening when being stronger. A more detailed description of the spectral ageing technique is described in Chapter 5.1.

Chapter 2

Broad Absorption Line Quasars

2.1 Quasars

At the end of the 1950s radio telescopes already had enough resolution to permit the identification of the optical counterparts of radio sources. Among all the radio sources seen in radio surveys, some strange objects were found, showing strong radio emission but appearing to be star-like at optical wavelengths with unexpected broad emission lines at unknown wavelengths. Schmidt (1963) first realized that these lines belonged to the Balmer series and were red-shifted. Exploiting especially the strength of the Lyman-α line they realized that all these sources were other than Galactic stellar objects. At that time the nature of those objects remained a mystery.

As already said in Chapter 1, these sources are now thought to be one face of the AGN phenomenon, in particular the most luminous AGN subclass at any frequency. Although the first quasar to be discovered was radio-loud, we now know that these radio-loud AGN are only the 10% of all AGNs. At low redshifts, the optical images of these sources show weak and diffuse emissions surrounding the object, which can be interpreted as coming from the host galaxy. Moreover, they typically show an ultraviolet excess, i.e. small U-B colour, with respect to the stellar spectral energy distribution.

At present, quasars are seen at any redshift, from about z=0 to z=6. Only because of their luminosity they are the only objects that can be seen at such a great distance, making them a unique tool to explore the early Universe. Moreover in optical high resolution spectra, narrow absorption lines are frequently seen which hardly correspond to the quasar redshift. These ones are interpreted as coming up from the material interposed between the source and the observer, providing this way the possibility to study the nature and properties of the extragalactic medium. Quasars are seen with a small angle from the pole, typically comprised between 5° and 45° from the polar axis, that means one jet is actually pointing towards the observer resulting in high luminosity because of relativistic

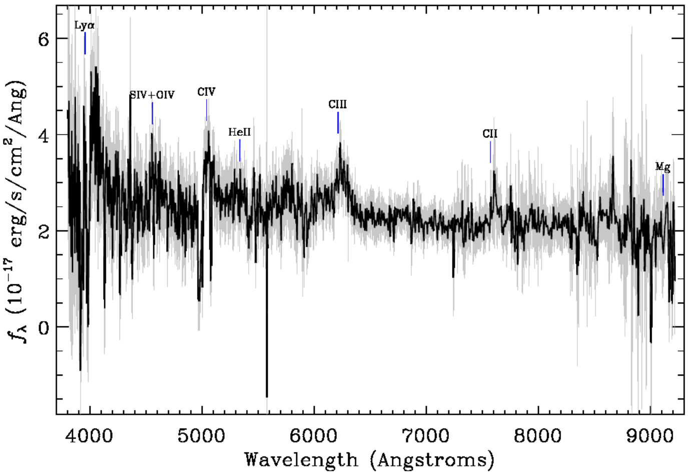

Figure 2.1: Optical spectrum of BAL QSO 0044+00 (SDSS-III)

beaming effects. Quasars appear variable at any frequency both in the continuum and in the emission lines. Optical variability has timescales of the order of weeks or months and an amount of some tens of magnitudes well beyond the radio variability timescales. The linear scales implied by the variations duration is $d < ct/(1+z)$ typically less than 10^{17} cm.

2.2 Broad absorption line QSOs

At the end of the sixties Lynds et al. (1967) discovered that the QSO PHL 5200 showed an atypical optical spectrum with wide and blueshifted absorption features regularly connected to resonance emission lines. With some assumption on the geometry of the object they suggested, as simplest explanation for the observation, "‘a source of continuum radiation surrounded by a relatively quiescent region responsible for the emission lines. The emitting region is surrounded by an expanding envelope in which the absorption bands originate."’ Lynds et al. (1967).

Nowadays around 15% of the observed quasars have been found to show broad absorption lines (BALs) in their optical spectra (see Fig. 2.1). The most prominent BALs are due to high-ionization species, particularly Li-like ions with one electron in the outer orbit. The typical line profile is a P Cygni type, apart from some cases in which the absorption feature is separated from the emission line up to $\sim 30,000$ km s^{-1}. Actually the most common feature is made of multi-component absorptions as shown in Fig. 2.2 and 2.3. These distinctive features can be hardly reconcile with absorption by individual clouds. On the contrary, the blueshift and the widths of these troughs are interpreted as the evidence of high-velocity wind-like outflows within the source, moving along the line of sight with velocities which can even reach several percent of the light speed (up to 0.2c in the most extreme cases). This kind of phenomenon is also observed in other classes of AGN, for example Seyfert-1 galaxies (Crenshaw et al. 2002), albeit always with velocities smaller than few hundred km s^{-1}. NV 1240-BALs often absorb part of the Ly α emission line, so the BAL region must lie outside the broad emission-line region (BLR), i.e. 0.1 pc from the quasar nucleus.

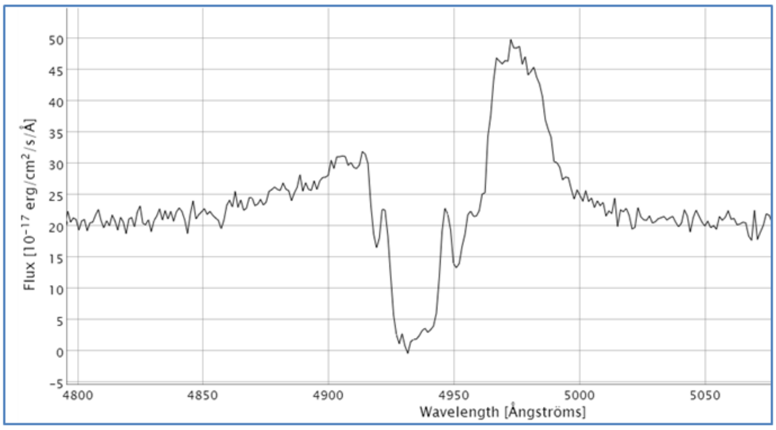

Figure 2.2: 1129+44 optical spectrum (SDSS-III)

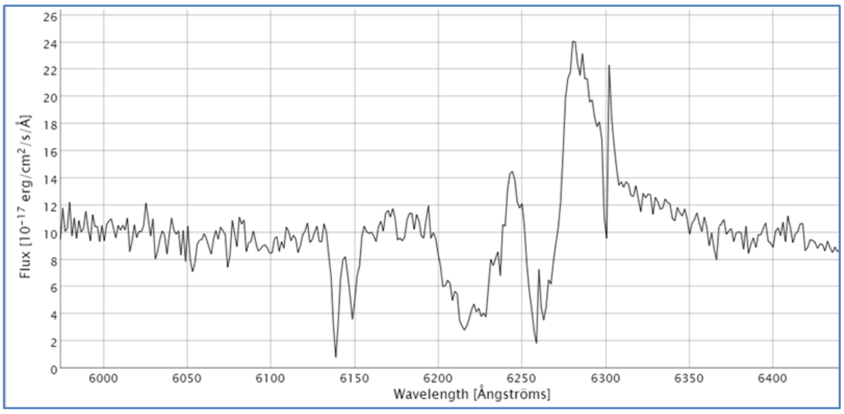

Figure 2.3: 1337-02 optical spectrum (SDSS-III)

In some cases there is no doubt about whether an absorption feature should be classified as BAL or not. In many more other cases instead, often because of poor resolution or signal-to-noise ratio, this identification becomes tricky (see Knigge et al. 2008). To make some order in the multiplicity of structures that have been observed, some quantitative criteria of selection between BALs and non-BALs have been defined. The most common ones are the *Balnicity Index* and the *Absorption Index*.

Balnicity Index and Absorption Index

Defined by Weymann et al. (1991), the Balnicity Index (BI) has been the first attempt to discriminate between BAL and non-BAL QSOs. According to this definition, the absorption feature must have a depth higher than 10% of the estimated continuum, in order to exclude false BAL QSOs, and a width at least as large as 2,000 km s^{-1}. The range, in which the trough is expected, starts from 3,000 km s^{-1} blueward the emission peak, because the inner region is considered affected by other absorptions disconnected from the BAL system, until 20,000 km s^{-1} blueward of the emission peak. The index basically evaluates some kind of equivalent width (in km s^{-1}) integrating the area below 10% of the continuum level as function of velocity. With this definition quasars which have weak or narrow absorption features have BI equal to zero.

$$BI = -\int_{25,000}^{3,000} \left[1 - \frac{f(v)}{0.9}\right] Cdv \tag{2.1}$$

where f(v) is the normalized flux density as a function of velocity displacement from the line center and C is a constant which can vary between 0 and 1. In particular, it is set to 1 when the integral results to be continuously positive during the previous 2000 km s^{-1} and it is reset to zero whenever the integral becomes negative. In this way, the first 2000 km s^{-1} of any absorption feature do not contribute to the balnicity index.

Studying the results from the Sloan Digital Sky Survey (SDSS) early data release (EDR), Hall et al. (2002) realized how variegated the Broad Absorption Line QSO population could be, from extremely reddened objects to objects with absorptions from unusual species, with unusual line ratios or absorption that extends longward of the systemic redshift. In this context they were led to elaborate a new BAL indicator which would not exclude troughs within 3,000 km s^{-1} of systemic velocity, Śmini-BALŠ troughs (Hemann 2001) that have widths less than 2000 km s^{-1} but for the rest appear equal to ŚnormalŠ BAL and troughs which extent further than 25,000 km s^{-1}. For these reasons they extended the integrated equivalent width range to 0 - 25,000 km s^{-1} or more, i.e. from the emission peak to some upper limit established for each spectrum individually paying attention not to confuse the trough with absorption features from other species at different wavelengths. The definition of the Absorption Index (AI) is the following:

$$AI = \int_{0}^{25000} \left[1 - \frac{f(v)}{0.9}\right] Cdv \tag{2.2}$$

where f(v) and C represent the same quantities as in the BI definition.

Although one can determine a statistical error for the former expression (see Hall et al. 2002), the greatest uncertainty on this value remains, as for the BI, the choice of the continuum level.

As can be easily imagined, neither of these two formal definitions completely describes the observed situations. On the one hand, the BI offers a strict but reliable criterion to recognize BAL features being sure to avoid contamination. The drawback of this rigid selection obviously lies in the exclusion of a great amount of cases which present narrower features than 2000 km s^{-1} or which are located outside the permitted range but which, in the end, share the same characteristics of the BAL systems. This heavily affects the selection of BAL quasars samples which then result incomplete, giving the wrong estimate on the BAL quasars fraction. On the other hand, the AI criterion, which reduces the restrictions, allows one to conduct a more complete selection with the risk though of creating too heterogeneous BAL quasars samples, including objects which do not seem to share the same properties (Knigge et al. 2008). Other criteria have been also proposed to overcome these difficulties but in any case some compromise has to be found. In conclusion, no universal method can probably be established. The BI remains a safe starting point for a sample selection but probably needs to be integrated, in a further step, by some 'case-by-case' classification.

2.3 Classification

On the basis of the ionizing level of the species, BAL QSOs can be classified in the following categories:

- High-ionization BAL QSOs (HiBALs) containing absorption features only from high-ionization state species e.g. C IV 1549, N V 1240, SI V 1400
- Low-ionization BAL QSOs (LoBALs) exhibit absorption troughs in low-ionization species e.g. Mg II 2800 and Al III 1857 in addition to the high-ionized transitions. Besides the presence of low-ionization troughs, the optical continua of LoBAL QSOs are more reddened compared to HiBAL QSOs. This IR excess, interpreted as strong extinction, suggests the presence of a high amount of dust in the central region of the AGN, maybe probing a relatively obscured and young quasar population which are still expelling their cocoon of gas and dust (Dai et al. 2011, Voit et al. 1993).
- Low-ionization BAL QSOs with Fe absorptions (FeLoBALs) are a subclass of LoBAL QSOs which show strong absorption by metastable excited states of Fe II and Fe III.

The majority of the BAL QSOs, about 90%, seem however to be HiBAL QSOs.

2.4 BAL variability

Since BALs in quasar spectra are interpreted as signatures of strong accretion disk outflows, they are expected to reflect any variation in shape, density and velocity of these wind-like structures. For this reason studying BAL variability should help to constrain morphology and changes of the outflow itself. For instance, variability on shorter time-scales provides information on the distance of the absorbing material from the central supermassive black hole; the more quickly the absorption varies, the closer the absorber is to the central engine. On the contrary, longer multi-year time-scales can give information on the homogeneity and stability of the outflowing gas. If no variability on long time-scales is observed one can deduce a persistent, smooth structure.

Two are the possible causes for BAL variability: the ionizing radiation is for some reason changing intensity, or the covering factor is evolving. The covering factor is discussed as parameter to quantify the fraction of the continuum source covered by the absorber. A change of covering factor fundamentally underlines a movement of the absorbing gas across the line of sight. In particular, the rotation of a non-axisymmetric outflow loosely anchored to the accretion disk can be, for example, responsible of that.

Since BAL troughs are often saturated and for this reason are weakly influenced by a change in the ionizing flux, the most favoured variability interpretation is, at the moment, linked to a change of the covering factor. However, many multi-year variability studies have been done in the last years which lead to different conclusions (Filiz Ak et al. 2012).

For example in individual objects, Capelluppo et al. (2012), found coordinated variability between absorption regions with different velocities. For this reason they were led to favour a change in the ionizing flux as cause of the observed variability. On the contrary, Gibson et al. (2008) found that line variation does not correlate with changes in the observed continuum, i.e. in the ionizing flux, so they proposed a change in the covering factor as cause of variations. Moreover, Filiz Ak et al. (2012) in their multi-year study found that both radio-loud and radio-quiet quasars are involved in this phenomenon and reported the first cases of complete transformation from BAL quasar to non-BAL quasar. Indeed, in most of the observed cases variations regarded only some of the absorption troughs. With their work they also discovered that when one absorption feature disappears the other troughs often weaken appearing quite well coordinated. Some explanations to these observations are a rotation of the wind or a variation of the shielding gas which then influence the ionization flux.

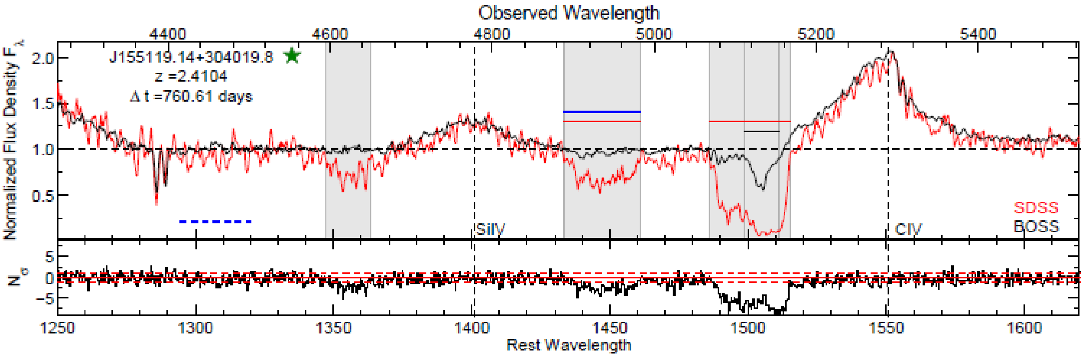

Figure 2.4: Multi-epoch spectra of quasars with disappearing BAL troughs obtained from SDSS-I/II (red) and BOSS (black) by Filiz AK et al. (2012)

2.5 Models and physical phenomenon

Since the discovery of BAL QSOs, it has been tried to understand the reason why only few QSOs exhibit blueshifted broad absorption features in their optical spectra and whether they could be considered as part of the standard QSO population. Different unifying models have been proposed to interpret their physical nature but no agreement has been reached yet. A good model should explain both the dynamical structure, in particular how to generate gas with velocities approaching 30,000 km s^{-1} and the observed range of ionization states, as well as justify the percentage of the objects observed and their phenomenology.

As previously mentioned, the first simple model was proposed by Lynds et al. (1967) in their article "A Quasi-Stellar Source with a Rapidly Expanding Envelope". They imagined a source of radiation with spherical symmetry surrounded by an expanding envelope in which emission lines and absorption bands originate. Because of an extensive velocity range in the absorbing region the absorption troughs show a great variety of width, in particular they assumed that the expansion velocity of the shell increases from most inner parts of the envelope to the outskirts. This first interpretation was already able to explain why these absorption features appeared in optical spectra, the reason for their blueshift and the variety of widths appealing to some kind of outflow within the source.

Although, since then, many speculations on this objects have been done, current models still describe broad absorption troughs as coming from material outflows within the source. In particular, in the light of the unified scheme, in which the black hole is thought to be accreted by gas orbiting around it, outflows and winds are considered to be an integral part of the accretion process. Understanding the details of this ejection mechanism would thus be a crucial step toward understanding the physics of the central engine of quasars. These phenomena probably also play a fundamental role in removing angular momentum from the gas, allowing a continuous accretion process. Moreover these outflows carry mass, momentum and energy into the surrounding environment, and therefore they may be also important to better understand the AGN feedback on the host galaxy evolution e.g. on the enrichment of the Intergalactic Medium and on the star-formation process (Arav et al. 2010, Cano-Dìaz et al. 2012).

Unfortunately, BAL QSOs are til now too distant to be resolved with the current optical telescopes, leaving many details about the physical nature of the disk and its surroundings unconstrained. For this reason, much of the discussion of BAL geometry is based on deductive reasoning. The three acceleration mechanisms present in literature, which can most probably lead these wind-like outflows, are here only briefly summarized:

Cosmic-ray pressure

Beyond radiation losses, a conspicuous part of the energy produced by the central engine can be released through a flux of ultrarelativistic neutrons. These particles are generated by inelastic proton-proton collisions which have been accelerated to very high energies ($\gamma \sim 10^7 - 10^8$) by shocks in the central engine with local photons or other protons. Because of relativistic time dilatation these neutrons can travel a distance $10^{-5}\gamma$ pc before decaying, typically from 1 to 10 pc. The protons resulting from these decays remain trapped by the local magnetic field and depositing there their energy can represent a steady energy injection mechanism able to accelerate the local gas giving life to outflows. This model quite well describes the observed absorption features but suffers of significant fine tuning of the parameters (Begelman et al. 1991).

Magnetic pressure

Cool clouds of gas can emerge from the disk surface pushed by the magnetic field lines which are anchored to the disk. As a consequence of encounters or magnetic buoyancy some clouds can acquire a small velocity perpendicular to the disk becoming this way the target of the UV radiation flux coming from the central source. In this way they are heated to about 10^4 K. These warm clouds can move outward but are always confined by the magnetic field that prevent their escape or dissipation in the perpendicular direction (see Fig. 2.5). Being tied to the field lines clouds are forced to corotate with the whole disk being subject to a centrifugal force which brings them to acquire a velocity much greater than the local Keplerian force (de Kool et al. 1997). A similar model was also proposed by Emmering et al. (1992) to explain the formation of the broad emission-line clouds which can be easily extended to the broad absorption-line clouds too (see Fig. 2.6)

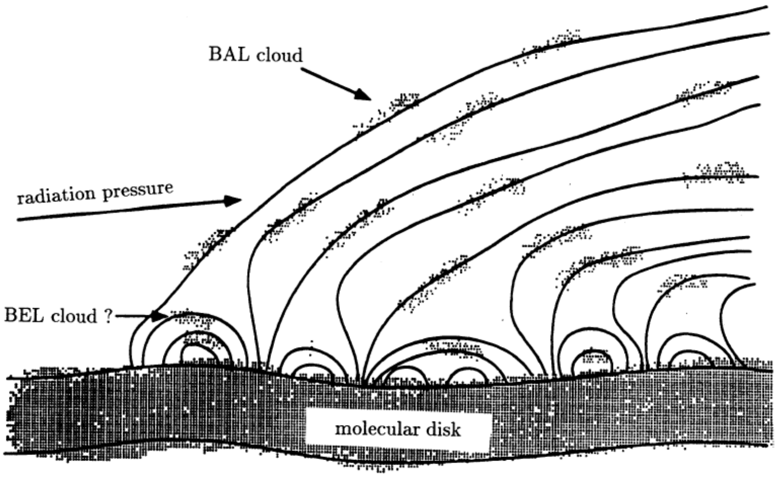

Figure 2.5: Illustrative picture of the magnetic field role and radiation pressure in the formation of BAL clouds from de Kool et al. (1995)

Radiation pressure

Inspired by wind models of massive O-stars, some AGN outflow descriptions based on radiation pressure have been elaborated. Since stars have a spherical geometry and can be supposed to emit isotropically, some revisions to the models have been done in order to fit them to the axial symmetry of AGN flat disks. In principle it can easily be shown that the UV photon flux coming from the central source has enough momentum to accelerate the absorbing material responsible for the broad absorption lines features. From the BALs themselves one can indeed estimate the energy deposited in the outflowing gas. The difficulty of this scenario is to find out how to prevent the wind plasma from being totally ionized allowing the existence of partially ionized species like C IV, N V or Mg II observed. To avoid this problem two pictures can be taken into consideration: the ouflowing wind consists actually of dense, small clouds (filling factor less than 1) the inner ones shielding the more external from receiving the totality of the radiation flux, or it has a continuous distribution (filling factor equal to 1), but something between the nucleus and the wind must be assumed for the shielding. The problem of describing the wind plasma as composed by small independent clouds has been preferred by many authors but it easily introduces the problem of cloud confinement. In order to go over this issue magnetic field or hot thermal plasma are invoked but no certainties have been reached yet. (e.g. de Kool et al. 1995, de Kool et al. 1997, Proga et al. 2000).

Independently from the exact physical mechanism responsible for these outflows, a more general question still remains open: why are they observed in a small number of objects only? That is, what is the discriminant between a BAL quasar and a 'normal' quasar? Over the years the debate on their nature has concentrated on two different scenarios. An orientational approach suggests that all quasars present this kind of outflows,

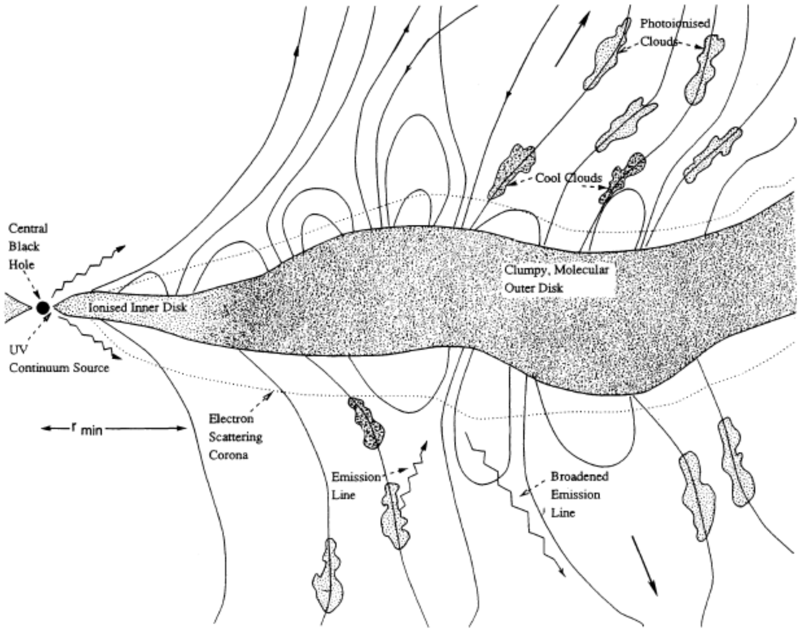

Figure 2.6: Schematic representation of magnetic disk wind model for broad emission-line region from Emmering et al. (1992)

but they only manifest their presence when observed along a particular line of sight. On the other hand, BAL QSOs could represent a short, primordial phase of the quasar's life. In the following paragraphs these two perspectives will be briefly discussed.

Orientation scenario

Due to the fact that, apart from broad absorption lines in optical spectra, BAL QSOs seem to share the same properties as non-BAL QSOs, some astronomers are led to hypothesize that they could be the same object but seen from a different point of view. This would mean that all quasars produce, during their accretion process, some outflows and winds; nevertheless we find evidence of that only if our line of sight intersects the ouflowing gas. This assumption obviously leads to elaborate a wind geometry model which must explain the observed percentage of BAL objects i.e. $\sim 20\%$ of the total population. The BAL outflow can be either equatorial, i.e. observed just above the molecular torus at low latitudes (Murray et al. 1995), or bipolar following the jets produced during the accretion process.

Elvis et al. (2000) proposed a funnel-shaped geometry to describe the outflow. The model was elaborated to explain both the broad and the narrow absorption features found in quasar spectra, as well as the variety of emission lines. The idea is that a flow of gas rises vertically from the rotating accretion disk accelerated by one of the mechanisms previously described. Then, it deflects radially and accelerates to velocities observed for

BALs, until it creates a 60° angle with the polar axes. If the observer is looking at the quasar just along the flow, he will then see broad absorption features in its spectrum. On the contrary if one looks along the symmetry axis no absorbers will be observed. Lastly, when viewed across the flow, narrow absorption lines (NALs) and X-ray warm absorbers are seen. The whole geometry of the model is defined to reproduce the correct ratios of NALs, BALs and non-absorbed quasars. The outflow is supposed to be made of a warm highly ionised medium (WHIM) whose temperature is around 10^6 K and density around 10^9 cm^{-3}. This gas can also be interpreted as the confining medium of the broad emission line clouds which are embedded in it and comove with it.

In the context of an orientation interpretation the model elaborated by Punsly (1999a, 1999b) is also worth mentioning. In these papers, the author describes a bipolar BAL wind coexisting with a relativistic jet as shown in picture. According to this model, the jet (red) is nested inside a cloud of BAL wind (grey) which has an opening angle of $\sim 25^\circ - 30^\circ$. The density of the BAL wind is supposed to increase in the proximity of the polar axis (black). This density gradients together with different line of sights, would hence be responsible for the different attenuation levels of the X-ray and UV ionizing radiation observed. In particular, viewing angles close to the polar axis ($< 15^\circ$) are more likely to suffer the maximum absorption and thus to represent LoBALQSOs. On the basis of radio variability considerations, Zhou et al. (2006) found agreement with this picture by measuring inclination angles $< 7^\circ$.

Evolutionary scenario

Another perspective for the interpretation of the BAL phenomenon is that they can represent a short moment of the entire quasar life. The high IR luminosity observed for these objects suggests the presence of a dense environment with a great amount of dust. This picture could be coherent with an early age in which the newborn quasar is still expelling the cocoon of material in which it is embedded.

On the basis mainly of these IR properties, Sanders et al. (1988) proposed an evolutionary sequence between warm ULIRGs and QSOs. In this scenario all quasars may start in an ultraluminous infrared phase, probably consequent to merger events. These ULIRGs are thought then to evolve in normal quasars by expelling great quantities of gas and dust and thus disclosing the active nucleus. The outflows which characterize BAL QSOs are then interpreted as typical of this transition phase.

Moreover, in support of this picture, recent VLBI observations allowed a high-resolution investigation of BAL QSOs. The results of these studies seem to show more compact morphologies if compared to non-BAL QSOs and often Gigahertz-Peaked Spectrum (GPS)

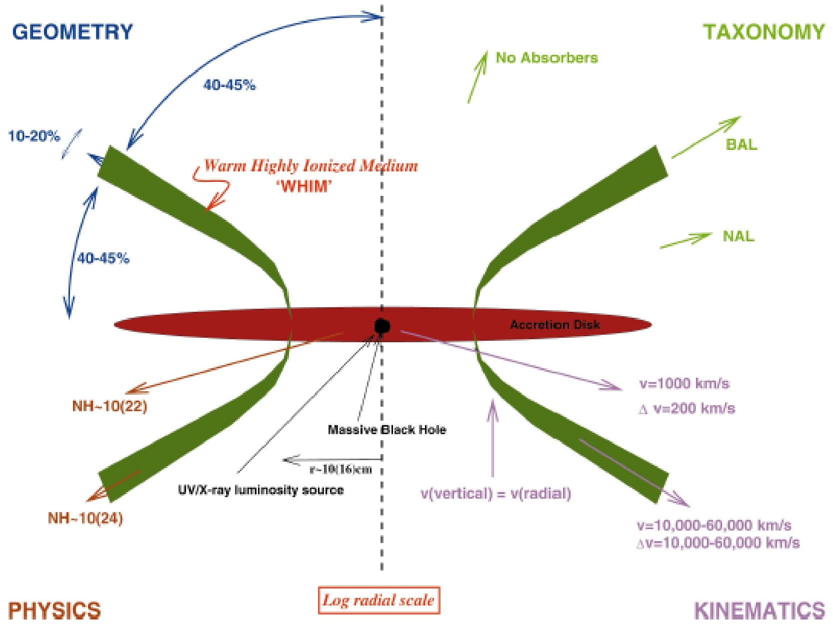

Figure 2.7: BAL geometry proposed by Elvis (2000). The four symmetric quadrants illustrate the following (clockwise from top left) : the opening angles of the structure, the spectroscopic appearance to a distant observer at various angles, the outflow velocities along different lines of sight, and some representative radii (appropriate for the Seyfert 1 galaxy NGC 5548) and some typical column densities.

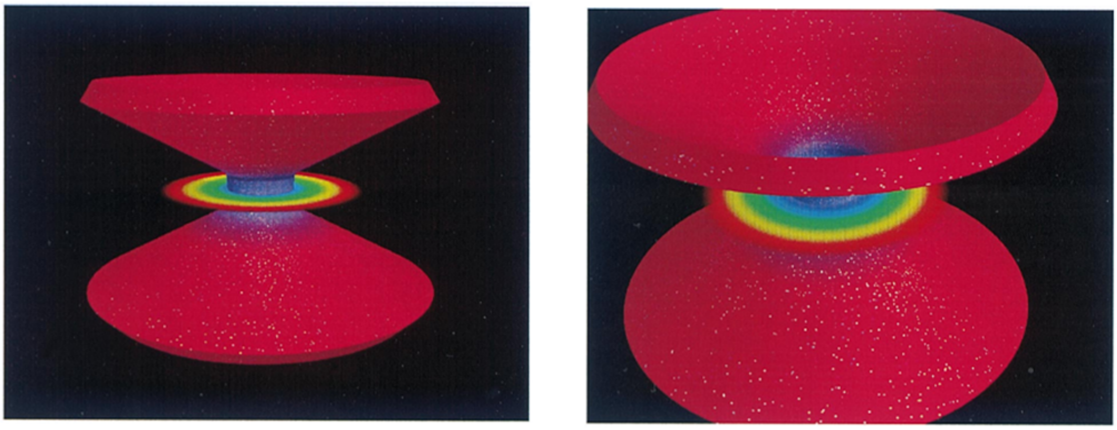

Figure 2.8: Three-dimensional views of the funnel-shaped structure proposed by Elvis (2000)

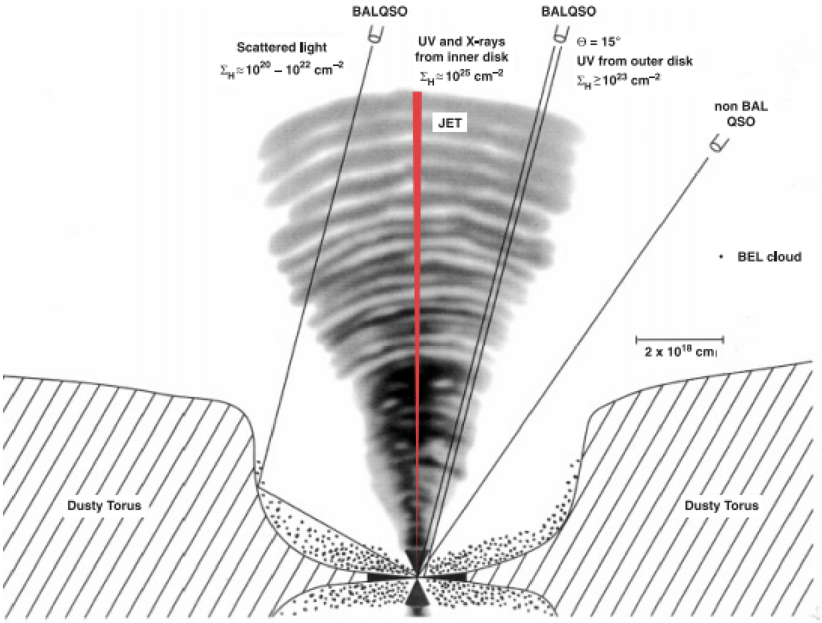

Figure 2.9: Sketch of the model proposed by Punsly et al. (1999). The jet (red) is nested inside a cloud of BAL wind (grey) which has an opening angle of $\sim 25° - 30°$. Depending on the line of sight the observer intercepts different amount of gas resulting in different absorption features on the optical spectra.

or Compact-Steep Spectrum (CSS) spectra. One must also consider the hypothesis that these outflows can be created not necessarily during the youngest age of the AGN but during a new AGN activity after a quiescent period. We already know indeed from radio observations that at least some black holes can experiment different phases of radio activity, in particular can restart some radio activity after a period in which it has been absent, the so called newborn quasars.

2.6 Radio-loud BAL QSOs

In order to understand whether BAL and non-BAL quasars could be considered as part of a single parent population, many multi-wavelength studies have been performed during the years. Until recently, astronomers were convinced that BALQSOs were only associated to radio-quiet AGN and that they could even be used to explore the difference between radio-loud and radio-quiet QSOs (Stocke et al. 1992). Many of the previously described models were actually elaborated on the basis of optical observations only. Thanks to the extended radio survey projects of the last decade it has become plain that, contrary to some previous observations, radio-loud BALQSOs exist, although in small percentage, and share quite the same characteristics of radio-loud QSOs (Becker et al. 1997, 2000). In this context the study of BAL QSO radio emission can be used as an additional diagnostic tools to explore the dichotomy. In fact, it can be crucial to constrain some source properties such as age, magnetic field, local column density and orientation providing new means of interpretation. Since the discovery is quite recent, however, only few studies have been conducted in this direction. The first complete sample present in literature has been created by Montenegro-Montes et al. (2008b) which is composed of the 15 radio brightest BAL QSOs known until 2005, with flux densities $S_{1.4GHz} > 15mJy$.

In principle, if the source is resolved at radio frequencies, one can even directly recognize jets and lobes from the map and determine the source orientation. However, most of the observed objects appear point-like at an arcsecond scale. In these cases though, the spectral index of a radio source contains information about the orientation of the object, being flatter ($\alpha < 0.5$) if the observer is looking right along the quasar polar axis or steeper in case of other inclinations ($\alpha > 0.5$). To support the orientation scenario one would expect to find two different radio spectral index distributions. What is observed instead is that the spectral index distribution of BAL quasars, even if centred at steeper spectral index, does not seem to favour any particular line of sight appearing almost identical to non-BAL QSOs. From this kind of study many authors conclude that a simple orientation model cannot explain the totality of observations and some more factors have to be included. In figures 2.10 results from Bruni et al. (2012) and DiPompeo et al. (2012) are presented which almost show the same trend.

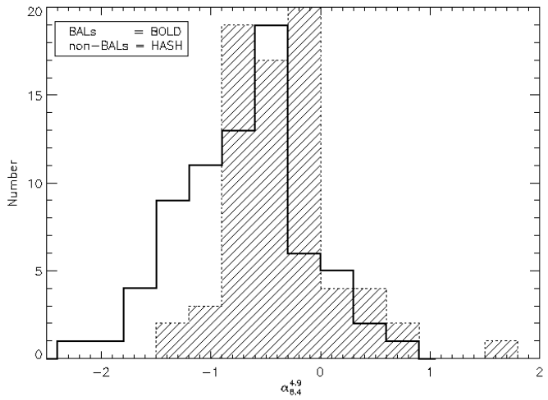

Figure 2.10: $\alpha_{8.4}^{4.9}$ comparison for BAL QSOs and non-BAL QSOs by DiPompeo et al. 2012

Another way to check the orientation of the sources is to look for variability in the radio emission (Zhou et al. 2006). Since extrinsic flux density oscillations, generally associated to refractive interstellar scintillation, are responsible for an amplitude variation

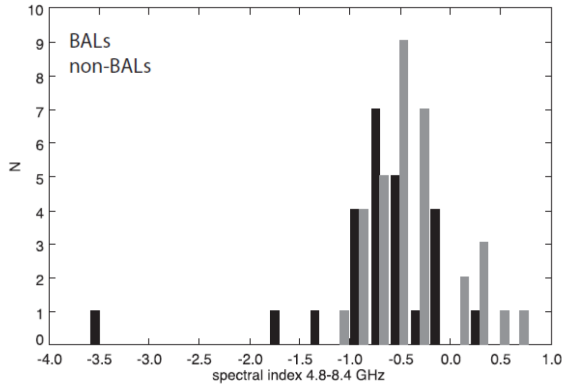

Figure 2.11: $\alpha_{8.4}^{4.9}$ comparison for BAL QSOs (black) and non-BAL QSOs (grey) by Bruni et al. 2012

within 2-3% (e.g. Blandford et al. 1986), change in flux densities greater than these values can be considered as intrinsic phenomenon. Nowadays it is generally accepted that the radio flares in AGN are produced by shocks propagating in the relativistic jet (Blandford & Rees 1978, Marscher & Gear 1985) and have typical timescales of 1-2 years (Hovatta et al. 2007). Moreover, if the line of sight is close to the object axis of symmetry, Doppler beaming effects can greatly amplify the variability intensity. Sometimes this could also be a better approach because it overcomes the difficulty of studying the object morphology with low resolution and sensitivity or of determining spectral slopes which are subject to intrinsic variations of flux densities.

The spectrum of a radio source can give information about the physical processes involved in the emission of the observed light, as well as on its evolutionary stage. Both the synchrotron break frequency and turn-over frequency can be used, for different theoretical reasons, to calculate an estimate of the radio source age. If it is true that young sources are also compact because their radio emission is at the beginning of its expansion, measuring the source size from the turn-over frequency can provide information on the age (Dallacasa 2000, O'Dea 1997). Great support to the evolutionary model would be given if the number of GPS BAL sources was high with respect to the non-BAL population. On the other hand if the break frequency can be determined from the spectrum, one can make use of spectral aging models to constrain the age of the sources. Also in this case one would hopefully expect a sharp difference in values between the two classes of objects (Ghosh & Punsly 2007).

Polarized radiation can also be used to extract information about the local environment like particle densities or the strength of the magnetic fields. These physical parameters could also in principle discriminate between the two categories of objects. For example higher densities in BAL QSOs could support an evolutionary scenario in which the AGN is at an early phase of its activity and it is still embedded in a dense cocoon of gas.

Chapter 3

Sample and previous work

3.1 Sample selection

Following the pilot sample of Montenegro-Montes et al. (2008) containing the 15 brightest radio-loud BAL QSOs known until 2005, with flux densities $S_{1.4GHz} > 15$ mJy, Bruni et al. (2012) selected a larger sample made of 25 BAL QSOs. These targets were chosen among all the objects from the 4th edition of SDSS Quasar Catalogue (Schneider et al. 2007) drawn from the 5th data release of the Sloan Digital Sky Survey (SDSS-DR5; Adelman-McCarthy et al. 2007) with a FIRST (Faint Images of the Radio Sky at Twenty-cm; Becker et al. 1997) counterpart lying < 2 arcsec away and having $S_{1.4GHz} > 30$ mJy. The selection has been limited to those objects whose redshifts lied in the range $1.7 < z < 4.7$ allowing the identification of CIV 1549 features on SDSS spectra. The selected objects included 25 BAL QSOs and 34 non-BAL QSOs.

The selection has been made in two steps. A first filtering was performed applying an automatic procedure to all 536 quasars which had the characteristics previously mentioned. The algorithm essentially fitted the CIV absorption feature with the Absorption Index equation shown in Chapter 2 using as continuum the median value of the signal in the rest-frame spectral window 1440-1470. In this way, 29 objects with AI > 0 were selected. On the other hand, 30 sources with AI = 0 were randomly selected to create the comparison sample. Bruni et al. 2012 applied a more conservative version of the AI defined by Hall et al. 2002, considering the parameter C unity only in continuos troughs wider than 1000 km/s (as in Trump et al. 2009), and a threshold of AI>100 to catalogue an object as BAL QSO. A more accurate by-eye check has then been performed to avoid errors introduced by the automatic routine and by the first-order continuum selection. Moreover, the fits were manually repeated using the spectral region between the Si IV to the CIV emission lines (both included) to find out the continuum with spline functions. As a result, 25 objects were found to have an AI > 100 km/s and thus were confirmed to join the BAL population, on the contrary the 34 leftovers were taken as comparison sample.

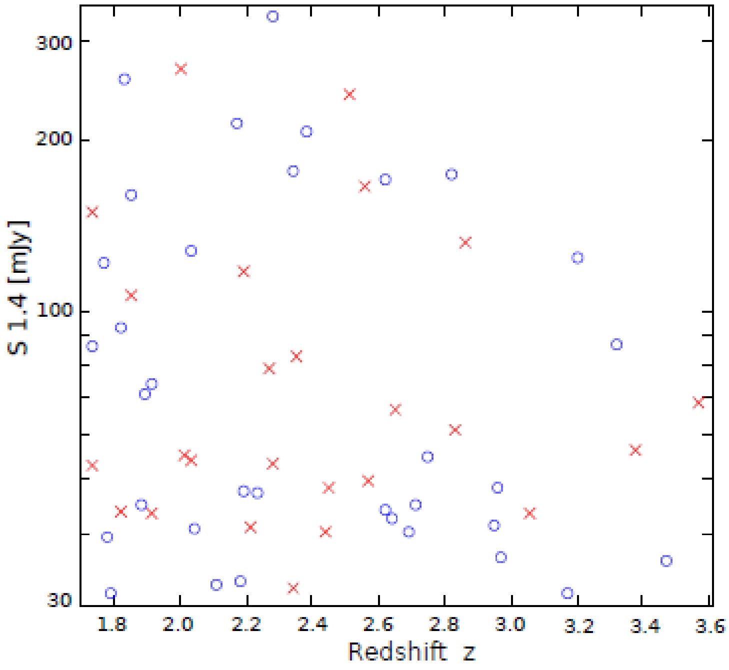

Figure 3.1: Redshift distribution of BAL QSOs (crosses) and non-BAL QSOS (circles)

The complete samples are listed in Tab. 3.1 and 3.2, where the optical coordinates and redshifts from SDSS for each object are shown, as well as the FIRST peak flux densities at 1.4 GHz. In Tab. 3.1 the BAL classification of Bruni et al. (2012) is also reported as last column, determined on the strength of the ionized species responsible for absorption features. For 11 BAL QSOs with $z \leq 2.3$ the SDSS spectra include the vicinity of the Mg II line at 2798 Å, allowing a search for absorption in Mg II, characteristic of low-ionisation BAL quasars (LoBALs) as well as in Fe II (rest-frame range from 2200 to 2700 Å), characteristic of FeLoBAL quasars. Three of the sources show Mg II absorption as well as Fe II absorption and are therefore FeLoBALs, labelled 'FeLo'. The remaining 8 sources lack absorption from both Mg II and Fe II and are identified as HiBAL and denoted as 'Hi'. None of the 11 sources are LoBALs, showing Mg II absorption but no Fe II absorption.

On the selected samples Bruni et al. (2012) conducted a multi-frequency campaign, using Effelsberg, the VLA and the GMRT. In order to find out the discriminating properties between the two populations, they performed different kinds of analysis on the observed objects, which are briefly listed here:

- *Flux-density variability* study at 4.8 and 8.4 GHz, comparing VLA and Effelsberg data with temporal separation equals to 1.6 years. From this analysis they found only three non BAL sources to be subject to flux density variations.

- *Spectral shape* studies to determine the frequency peak of the sources. As a result, 9 BAL QSOs and 8 non-BAL QSOs, 36% and 24% respectively, were found to have a GPS.

- *Spectral indices* α were calculated in the frequency intervals 4.8-8.4 and 8.4-22 GHz. Both populations showed a wide α distribution, from flat ($\alpha < 0.5$) to steep ($\alpha > 0.5$) indices.

- *Rotation measures* were calculated when the signal to noise was high enough to measure the polarized flux densities. For the other sources only fractional polarization (m) upper limits were obtained. A median value for m of 1.8-2.5% was found for both populations.

Comparing the results of these analysis for samples of BAL and non-BAL QSOs, Bruni et al. (2012) did not find out any statistically relevant distinction. The broad range of spectral indices measured for both populations suggests in fact that a variety of orientations are present in both classes of objects. On the other hand, the number of compact sources of GPS type are not found to dominate in the BAL QSO sample, implying that not all sources can be considered young as supported by the evolutionary scenario. Moreover, this is supported by the polarized flux densities which do not seem to show a higher level of depolarization as expected in case of young, obscured, dusty sources.

High-resolution observations were also performed for 11 sources in VLBI technique with the EVN (5 GHz) and VLBA (5, 8.4 GHz) interferometers. Among the 9 resolved objects found no common morphology has been recognized. Double sources, as well as core-jet and symmetric have been detected implying again different orientation.

3.2 This work

The objects presented in this work belong to the sample selected by Bruni et al. (2012) previously described. Because of too short integration times, data from Bruni et al. (2012) did not allow to obtain complete information on the polarization properties of both BALs QSOs and comparison QSOs samples. This argument motivated a request of new observing time to both EVLA and Effelsberg telescopes, with longer exposures in order to increase the S/N. In 5 to 10 minutes, depending on the source brightnesses (10-250 mJy), the EVLA telescope can indeed reach at 4.6 GHz, 10 sigma detection for the polarized flux densities (1 mJ) and in 10 to 20 minutes at 8.4 GHz. Unfortunately, because of technical reasons, which will be later discussed, we could not extract the polarization information from EVLA data. Because of that, we focused our attention on other scientific investigations.

These new observations, in fact, allowed us to check for any significant variability phenomenon too. Indeed, a period of more than one year and a half passed between the observations by Bruni et al. (2012) and the ones reduced in this thesis.

The main analysis, presented in this work, concerns a spectral age study of the whole Bruni et al. (2012) BAL and non-BAL QSOs samples. The age of the radio-sources could be indeed a discriminating property between the two populations and is intended to complete the comparison analysis between the two population of objects begun by Bruni et al. (2012).

Name	RA (J2000)	DEC (J2000)	z	AI (km/s)	$S_{1.4}$ (mJy)	BAL Type
0044+00	00 44 44.06	+00 13 03.5	2.28	1170	53.1	-
0756+37	07 56 28.24	+37 14 55.6	2.51	330	239.4	-
0816+48	08 16 18.99	+48 23 28.4	3.57	260	68.3	-
0842+06	08 42 24.38	+06 31 16.8	2.45	26901	48.1	-
0849+27	08 49 14.27	+27 57 29.7	1.73	540	52.8	Hi
0905+02	09 05 52.41	+02 59 31.5	1.82	130	43.5	Hi
0929+37	09 29 13.97	+37 57 43.0	1.91	2170	43.2	Hi
1014+05	10 14 40.35	+05 37 12.6	2.01	250	55.0	Hi
1040+05	10 40 59.80	+05 55 24.4	2.44	49201	40.2	-
1054+51	10 54 16.51	+51 23 26.1	2.34	22201	32.0	-
1102+11	11 02 06.66	+11 21 04.9	2.35	506	82.3	-
1103+11	11 03 34.79	+11 14 42.4	1.73	380	148.0	FeLo
1129+44	11 29 38.47	+44 03 25.1	2.21	1430	41.1	Hi
1159+01	11 59 44.82	+01 12 06.9	2.00	22601	266.5	FeLo
1159+06	11 59 01.75	+06 56 19.1	2.19	3645	116.6	Hi
1229+09	12 29 09.64	+09 38 10.1	2.65	230	66.2	-
1237+47	12 37 17.44	+47 08 07.0	2.27	13001	78.5	FeLo
1304+13	13 04 48.06	+13 04 16.6	2.57	640	49.6	-
1327+03	13 27 03.21	+03 13 11.2	2.83	190	60.7	-
1335+02	13 35 11.90	+02 53 09.5	1.85	210	105.3	Hi
1337−02	13 37 01.40	−02 46 30.3	3.06	590	43.3	-
1404+07	14 04 33.01	+07 28 47.2	2.86	120	131.1	-
1406+34	14 06 53.84	+34 33 37.3	2.56	350	164.4	-
1603+30	16 03 54.15	+30 02 08.7	2.03	1355	53.7	Hi
1624+37	16 24 53.47	+37 58 06.6	3.38	10201	56.1	-

Table 3.1: The sample of 25 radio-loud BAL QSOs selected by Bruni et al. (2012). Columns 2-7 give the optical coordinates and redshifts from SDSS, the absorption index for the C IV line (width of at least 1000 km s^{-1}), the FIRST peak flux densities and the type.

Name	RA (J2000)	DEC (J2000)	z	$S_{1.4}$ (mJy)
0014+01	00 14 27.93	+01 13 34.0	2.18	32.7
0029−09	00 29 49.46	−09 51 44.8	2.71	44.7
0033−00	00 33 04.32	−00 48 14.5	1.79	31.3
0103−11	01 03 28.72	−11 04 14.6	2.19	47.5
0124+00	01 24 01.75	+00 35 00.1	1.85	159.3
0125−00	01 25 17.19	−00 18 29.7	2.28	329.1
0152+01	01 52 10.35	+01 12 28.9	3.17	31.3
0154-00	01 54 54.37	−00 07 23.1	1.83	255.4
0158−00	01 58 32.52	−00 42 38.5	2.62	169.4
0750+36	07 50 19.55	+36 30 02.8	2.03	126.7
1005+48	10 05 15.98	+48 05 33.2	2.38	206.1
1322+50	13 22 50.55	+50 03 35.4	1.73	85.7
1333+47	13 33 25.06	+47 29 35.4	2.62	44.0
1401+52	14 01 26.15	+52 08 34.6	2.97	36.2
1411+34	14 11 55.24	+34 15 10.4	1.82	92.5
1411+43	14 11 52.77	+43 00 23.9	3.20	122.9
1502+55	15 02 06.53	+55 21 46.1	3.32	86.5
1512+35	15 12 58.36	+35 25 33.3	2.23	47.1
1521+43	15 21 49.61	+43 36 39.4	2.17	213.5
1528+53	15 28 21.68	+53 10 30.7	2.82	172.4
1554+30	15 54 29.40	+30 01 19.0	2.69	40.0
1634+32	16 34 12.77	+32 03 35.4	2.34	175.2
1636+35	16 36 46.41	+35 57 43.7	1.91	73.4
1641+33	16 41 48.07	+33 45 12.5	2.75	54.5
1728+56	17 28 52.61	+56 41 43.9	1.77	120.3
2109−07	21 09 26.41	−07 39 25.9	1.88	44.8
2129+00	21 29 16.61	+00 37 56.7	2.96	48.0
2143+00	21 43 24.37	+00 35 02.8	2.04	40.6
2238+00	22 38 43.57	+00 16 48.0	3.47	35.6
2244+00	22 44 59.44	+00 00 33.4	2.95	41.4
2248−09	22 48 00.70	−09 07 44.9	2.11	32.4
2331+01	23 31 32.84	+01 06 21.0	2.64	42.4
2346+00	23 46 24.56	+00 19 14.2	1.78	39.4
2353−00	23 53 30.21	−00 04 13.4	1.89	70.5

Table 3.2: The sample of 34 comparison (non-BAL) QSOs selected by Bruni et al. (2012) . Columns 2-5 give the optical coordinates and redshifts from SDSS and the FIRST peak flux densities.

Chapter 4

Radio observations and data reduction

4.1 Radio window

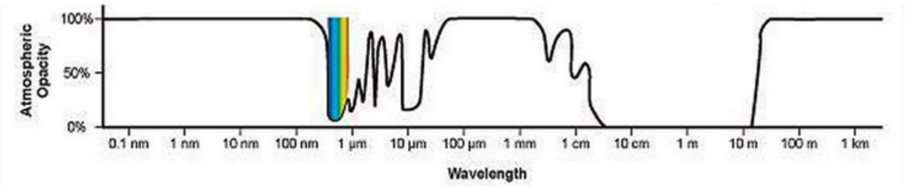

Figure 4.1: Atmospheric electromagnetic opacity

Because of the atmospheric opacity, ground-based astronomy is limited to the optical and radio windows of the electromagnetic spectrum (see Fig. 4.1). The radio window extends from about 0.02 mm to 30 m. These limits are dictated by the atmosphere which, because of its composition (CO_2, O_2, H_2O molecules), absorbs photons with wavelengths lower than 0.02 mm and, because of free electrons of the ionosphere, reflects back into space photons with wavelengths longer than 30 m. Also in this frequency range however, depending on the atmospheric conditions, radio emission can be attenuated up to 1.5 dB. Moreover, the atmosphere emits radio noise that can seriously degrade the sensitivity of ground-based radio observations. As the frequency increases, opacity gets higher, causing bigger distortions to observations. For all these reasons the very best sites for observing, especially at higher frequencies, are exceptionally high and dry.

In addition to atmospheric degradation, celestial radio signals are also corrupted by Radio Frequency Interferences (RFI), i.e. spurious signals, both natural and artificial, that can contaminate the real astrophysical information. These can be produced for example by ground thermal emission or because of man-made devices such as wireless networks, planes, satellites, as well as the telescope electronic parts themselves. The International Telecommunication Union (ITU) is the specialized agency of the United

Nations, responsible for information and communication technologies, which controls and regulates the global use of the radio spectrum, preventing also interference between artificial transmissions and radio astronomy.

Unlike other branches of astronomy in which photons are so energetic to produce the photoelectric-effect, radio astronomy makes use of the diffraction phenomenon to detect radiation. The basic elements of a radio telescope are the primary mirror and the receivers. Depending on the telescope structure there can be also a secondary mirror located in the primary focus which redirects light to the receivers at secondary focus. Each radio telescope is characterized by a diffraction figure called power pattern or beam which is usually expressed in polar coordinates $P(\theta,\phi)$. This represents the measure of the instrumental response with respect to the pointing and, if the radiation source is point-like, allows the definition of the instrumental Point Spread Function (PSF). The beam maxima are known as lobes; a distinction is usually made between the main lobe, where the antenna is most sensitive, and the minor lobes or sidelobes (see Fig. 4.2). The angle subtended by the half power level of the main lobe is called Half-Power Beam Width (HPBW) and it is a measure of the instrument resolving power. The angular resolution of a telescope is:

$$\theta = 1.22\frac{\lambda}{D}$$

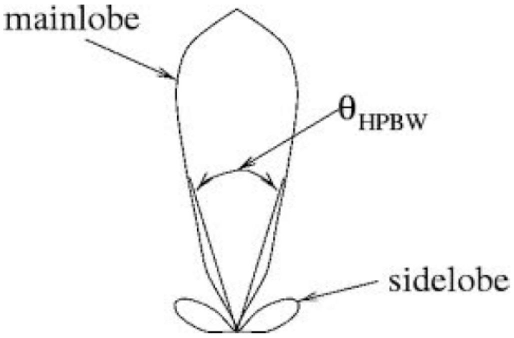

Figure 4.2: Represenattion of the antenna power pattern

To improve the resolution at fixed λ one should increase D. Unfortunately the size of the dish cannot exceed a maximum value for structural and economic reasons. To overcome the problem, the interferometric technique has been introduced. Interferometers are systems of many antennas working together exploiting the interference principle between coherent waves and realizing an 'unfilled aperture telescope'. In this way, the resolution is improved because D now represents the distance between two antennas (baseline length).

The simplest interferometer consists of two antennas. Signals collected by each antenna are combined using a correlator. In order to correlate coherent signals from the two instruments one has to fix a reference antenna and take into account the geometric delay of radiation between the two instruments.

The main idea in aperture synthesis interferometry is that it is possible to reconstruct brightness distribution of a source from the amplitude and phase of interference fringes. A Fourier transform then allows to obtain the source image from the interference fringes.

The sum of the received signals produces a series of maximum and minimum called interference fringes. The Fringe Visibility V(u,v) is defined as a function where u and v represents the coordinates of a baseline projected on a plane perpendicular to the line of sight called (u,v) plane (Fourier plane). The visibility function can be written as the Fourier anti-transform of the sky brightness B(x, y):

$$V = V_0 e^{1\Phi} \propto \int\int_{-\infty}^{+\infty} B(x,y) e^{2\pi i(ux+vy)} dxdy$$

where V_0 is defined as the amplitude and Φ is the phase. This relationship connects the space of Fourier visibility with the space of real brightness.

In case of circular feeds the correlated visibilities between two antennas i and j can be represented by the following expression:

$$V_{i,j} = \left\langle \begin{pmatrix} R_i \\ L_i \end{pmatrix} \right\rangle \otimes \left\langle \begin{pmatrix} R_j \\ L_j \end{pmatrix} \right\rangle = \begin{pmatrix} < R_i R_j > \\ < R_i L_j > \\ < L_i R_j > \\ < L_i L_j > \end{pmatrix} \tag{4.1}$$

where R and L are the provided voltages from the right circular polarization (RCP) and left circular polarization (LCP) channels in case of circular feeds.

An antenna pair samples the visibility in a single point of the u-v plane. Using N antennas, (N(N-1))/N points of the u-v plane are sampled. Most interferometers use then the aperture synthesis technique to increase the u-v plane coverage. Taking advantage of the Earth rotation a single baseline assumes in fact different lengths from the source point of view. Therefore each antenna pair can sample different points of the u-v plane during the observation.

We stress that while with single-dish observations it is possible to sample the emission coming from all the spatial frequencies ranging from zero to λ/D (where D is the antenna diameter) with interferometric ones we can only sample the emission coming from the spatial scales between λ/b_{min} and λ/b_{max} (where b_{min} and b_{max} are the shortest and longest baseline respectively). To retreive the zero spacing information, necessary when dealing with very extended sources, it is possible to combine single dish and interferometric observations of the same source.

The four correlations RR, LL, LR and RL can be combined to form the Stokes parameters I, U, Q, V which have been mathematically defined to describe the polarization state of radiation in a convenient way. Stokes parameters are indipendent on the feed polarization bases (linear or circular) allowing the comparison of signals coming from different instruments. In particular, they express the total intensity (I), the degree of polarization (m), and the shape parameters of the polarization ellipse such as the polarization angle (ϕ) by opportunely combining the for correlations RR, LL, LR and RL:

$$\begin{aligned} I &= (V_{RR}+V_{LL})/2 \\ Q &= (V_{RL}+V_{LR})/2 \\ U &= (V_{RL}-V_{LR})/2i \\ V &= (V_{RR}-V_{LL})/2 \end{aligned} \tag{4.2}$$

$$\begin{aligned} m &= \frac{\sqrt{U^2+Q^2+V^2}}{I} \\ 2\phi &= atan\frac{U}{Q} \end{aligned} \tag{4.3}$$

In this work we use observations from both single dish and interferometric telescopes. The different data treatment will be described in the next sections.

4.2 Jansky Very Large Array Observations

The Karl G. Jansky Very Large Array (JVLA) is one instrument of the National Radio Astronomy Observatories (NRAO). It is located on the Plains of San Augustin in New Mexico (34°04′43.497″N 107°37′05.819″W - 2124 m altitude).

Figure 4.3: Jansky Very Large Array (JVLA), New Mexico

It is constituted of 27 movable antennas of 25-meter diameter each, able to observe in a frequency range from 58 MHz to 50 GHz. The antennas are arranged in a Y-shape interferometric array that can assume four different spatial configurations by locating single antennas at different distances. The most common configurations used are four (A, B, C, D) and cover a distance range between 1 and 36 km providing a wide range of possible resolutions. The D configuration is the widest one so it is mostly used to observe extended structures. On the contrary the A configuration is the most compact one thus useful to resolve the most compact sources. The Y-disposition allows the interferometer to provide the same resolution in all three directions. In addition to these four classical configurations, there are three hybrid ones called DnC, CnB, BnA mostly useful to observe sources in particular ranges of celestial coordinates maintaining a quite circular point spread function. Each antenna is then provided by eight receivers whose frequency bands are generally referred to as L, S, C, X, Ku, K, Ka and Q. More quantitative details on receivers and configurations can be found in Tab. 4.1 and 4.2. Fig. 4.4 also show a picture of the variety of feeds which are mounted on each antenna.

Figure 4.4: Image of one antenna receivers at secondary focus

In the last years the VLA has undergone a series of technological upgrades resulting in a new instrument named EVLA (Expanded Vary Large Array) with enhanced capabilities in terms of sensitivity and spectral resolution. The EVLA project lasted 11 years and was completed at the end of 2012. The modernized instrument has been then renamed in honor of Karl Jansky as Karl G. Jansky Very Large Array (JVLA). The main goals of these upgrades concerned the completion of the frequency coverage from 1 to 50 GHz, a noteworthy increase in the bandwidth, resulting in a continuum sensitivity improvement of

Band	Range (GHz)	θ_{HPBW} (arcsec)
4 m (4)	0.058-0.084	24-850
90 cm (P)	0.23-0.47	5.6-200
20 cm (L)	1.0-2.0	1.3-46
13 cm (S)	2.0-4.0	0.65-23
6 cm (C)	4.0-8.0	0.33-12
3 cm (X)	8.0-12.0	0.2-7.2
2 cm (Ku)	12.0-18.0	0.13-4.6
1.3 cm (K)	18.0.26.5	0.089-3.1
1 cm (Ka)	26.5-40	0.059-0.19
0.7 cm (Q)	40.0-50.0	0.043-1.5

Table 4.1: Frequency coverage, bandwidths and resolutions of the JVLA

Configuration	A	B	C	D
B_{max} [km]	36.4	11.1	3.4	1.03
B_{min} [km]	0.68	0.21	0.035	0.035

Table 4.2: Array configurations characteristics

about an order of magnitude and the implementation of a new correlator able to manage data from the greater bandwidths. In Tab. 4.3 a list of the main changes is presented, together with a factor of improvement of the new instrument with respect to the old one.

One of the most extreme changes in the whole transformation certainly regards the correlator, which is now basically a spectral line correlator, much more flexible and powerful than the previous one. This means that, apart from the scientific analysis goal - continuum or spectral lines - all observations done with this instrument will get data in spectral lines mode i.e. from a number of different channels. This could be a great advantage also for continuum observations because it allows a detailed channel to channel editing, thus removing any possible RFI from data. Furthermore, all observations require some more steps during the data reduction: a bandpass correction (and often a delay calibration as well). The new correlator is now working since January 2011.

Another remarkable renovation, as already briefly mentioned, concerns the instrument sensitivity which strongly depends on the bandwidth. The theoretical thermal noise expected for an image is given by:

$$\Delta S = \frac{SEFD}{\eta_c \cdot \sqrt{n_{pol} N(N-1) t_{int} \Delta\nu}}$$

where SEFD is the System Equivalent Flux Density (Jy) defined as the flux density of

Parameter	VLA	EVLA	Factor
Continuum sensitivity (1-σ, 9 hr)	10μJy	1μJy	10
Maximum BW in each polarization	0.1 GHz	8 GHz	80
Number of frequency channels at max. BW	16	16,384	1024
Maximum number of freq. channels	512	4,194,304	8192
Coarsest frequency resolution	50 MHz	2MHz	25
Finest frequency resolution	381 Hz	0.12 Hz	3180
Number of full-polarization sub-correlators	2	64	32
Log (Frequency Coverage over 1-50 GHz)	22%	100%	5

Table 4.3: Instrument specifications before and after the upgrades

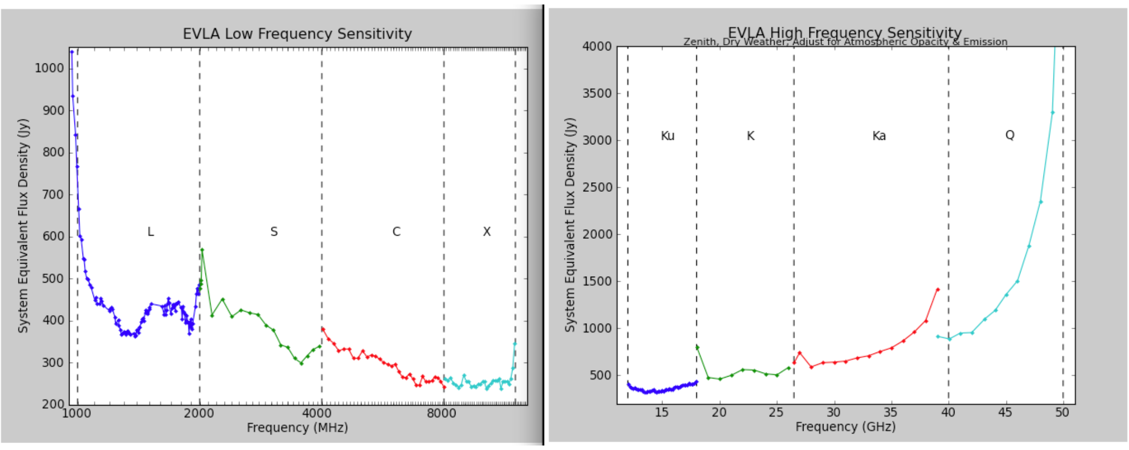

Figure 4.5: Trends of the System Equivalent Flux Density (Jy) with spectral bands

a radio source that doubles the system temperature T_{sys}. The exact expression is given by $SEFD = 5.62T_{sys}/\eta_A$ where η_A is the antenna aperture efficiency in a given band. This means that more sensitive instruments will have a lower SEFD. Moreover, η_c is the correlator effciency, η_{pol} is the number of polarization used, N is the number of antennas, t_{int} the total integration time (s) and $\Delta\nu$ is the bandwidth (Hz). In figure 4.5 the trend of the SEFD as function of frequency is shown.

Because of the contributions of different factors however, the theoretical thermal noise can never be reached in practice. Confusing sources can also play an important role in this issue. If the array configuration does not ensure a good resolution (configuration D, C) one has to consider a confusion error too, to be added in quadrature to the thermal noise. Moreover, interferometric images suffer of sidelobe confusion from uncleaned sources which lie just outside the image. Weather and source elevation also contribute to corrupt the signal, affecting significantly the total noise of the image.

4.2.1 EVLA observations

Our observations were scheduled in filler mode and collected different short runs (from 30 to 90 minutes) during spring 2011 in both C and X band corresponding to a central frequency of 4.6 and 8.4 GHz. The correlator setting had 64 channels of 2 MHz, each covering a full band of 128 MHz. The resolution reached using this setup is $\approx 2arcsec$. What is commonly needed to calibrate the total intensity in interferometric data is to observe, at least once during the observing run, a flux density calibrator and, at regular intervals during the observing session, a secondary calibrator. Both objects should be point-like sources, with no intrinsic variability and sufficiently high flux densities to determine corrections with sufficient signal-to-noise ratio (SNR). In this section the main steps of the data reduction used during the work will be briefly shown. Each data set consists in a primary calibrator (3C286 and 3C138) observed in one scan at the beginning of the observation and in a secondary calibrator observed at regular intervals between the target integration scans. Both primary and secondary calibrators were also considered as polarization calibrators.

4.2.2 Data reduction

Data were reduced using both versions 3.4 and 4.0 of the CASA[1]. CASA is the new software package expressly developed to process data collected from the ALMA[2] and EVLA telescopes. Although AIPS[3] seems to be still able to treat this kind of data, now CASA is recommended by NRAO because constructed to support the new data format coming out from the ALMA and EVLA correlators with higher efficiency and speed. This new format, called Measurement Set (.MS), consists of a MAIN table containing the visibility data and associated sub-tables containing auxiliary information about the observations (antennas, sources, polarization, ...). Each main table of the MS contains three main columns in which data are stored. The principal one, which actually contains raw data, is called 'DATA' column, while the others, 'CORRECTED DATA' and 'MODEL' columns, contain respectively the corrected visibilities, once the calibration has run, and the model to be used as reference during the calibration.

As previously explained, the new correlator of the EVLA started to work at the beginning of 2011, for this reason we had to deal with a very new instrument and analyze data with special carefulness to avoid technical errors. The same attention has been paid when using the CASA software which, despite some years of testing and improvements, is still under development.

---

[1] Common Astronomy Software Applications, http://casa.nrao.edu/

[2] The Atacama Large Millimeter/sub-millimeter Array (ALMA) is an astronomical interferometer located in the Atacama desert of northern Chile operational since March 2013

[3] Astronomical image processing system, http://www.aips.nrao.edu

Data examination and editing

Before starting with the calibration, visibilities inspection is mandatory in order to get rid of data which appear evidently corrupted. For many reasons indeed, some of them can present values irremediable out of trend. This can be due, for example, to an antenna which did not work well during the observation or to RFI in some peculiar channels. These data have to be removed from the data set because they cannot be corrected by the calibration process, to the contrary they can compromise the quality of the calibration itself.

In our case, data were retrieved already with an 'a priori flagging' in which autocorrelated signals were already deleted. We then proceeded with a systematic removal of the first seconds of each scan; this short time interval indeed is very often affected by malfunctioning due to the just finished antenna pointing. Another regular flagging we made concerns channels near the full band-width border. In case of an ideal filter in fact, the device should completely suppress the signal with frequencies outside the passband. What happens in reality is that, because of manufacturing problems, frequencies just outside the nominal bandwidth are only attenuated but not totally rejected. These channels obviously introduce some errors in the real signal and should be eliminated. It is easy to notice how low the responses of the edge channels are respect to the more central ones (see Fig. 4.7). For each data set then, some spectral windows, antennas or correlations were flagged because considered too far from the mean trend. The task used to plot data is called PLOTMS and allows to display visibilities in an interactively way as function of whatever is needed. Once bad points have been recognized, the task 'TFLAGDATA' allows one to remove them from the data set. It is noteworthy to note that the task acts directly on the DATA column modifying definitively the data set. It is probably worth saving the data at the beginning of the work and then in some further steps. The proper task to do that is called FLAGMANAGER which permits to save and organize your editing.

Calibration theory

Once the spurious signal has been removed from the data, one can begin with the calibration process which aims at correcting the visibilities from instrumental or atmospheric contamination. The response of antenna i with circular polarized feeds (R, L) can be factorized into a number of physically distinct components using the Jones' matrix formalism. Here we will give only some hints at this formalism, for a more detailed description refer to 'Syntesis Imaging in Radio Astronomy II (1998 NRSO Summer School Book)'. The Jones' matrix actually includes all propagation and transmission effects and can be seen as the product of various matrices, each of them representing one specific contribution:

$$J_i = G_i B_i D_i P_i \tag{4.4}$$

The first term G_i is typically called the 'gain' matrix and can be written as:

$$\begin{pmatrix} G_{i,R} & 0 \\ 0 & G_{i,L} \end{pmatrix} \tag{4.5}$$

where $G_{i,R}$ and $G_{i,L}$ are the time dependent complex gain factors for the two polarized signals. They can be written explicitly as $G_i = g_i(t)\exp i(\phi_i)$ with $g_i(t)$ and ϕ_i respectively amplitude and phase gains. This term represents the overall instrumental response dictated by each electronic component located between the feed and the correlator plus the atmospheric corruption and the absolute flux density scale factor.
The second term B_i represents the complex Bandpass gains, i.e. the instrumental response as function of frequency due to the presence of electronic spectral filters. In other words, it represents the frequency dependent version of G:

$$\begin{pmatrix} B_{i,R} & 0 \\ 0 & B_{i,L} \end{pmatrix} \tag{4.6}$$

The term D_i models instead imperfections in the feed polarization response and will be further discussed later.

The term P_i is referred to as the *parallactic angle matrix*. It describes the rotation of the feeds of an alt-az mounted telescope relative to the source as they track the source in the sky. In case of circular feeds the matrix can be written as follows:

$$\begin{pmatrix} e^{-i\chi} & 0 \\ 0 & e^{i\chi} \end{pmatrix} \tag{4.7}$$

where χ denotes the parallactic angle which depends on the latitude of the telescope L, the hour-angle of the source H and the apparent declination of the source δ as follows:

$$\tan\chi = \frac{\cos L \sin H}{\sin L \cos\delta - \cos L \sin\delta \sin H}$$

An example of parallactic angle trend is shown in Fig. 4.6. There, the variation of χ versus H, for a telescope of latitude equal to 45°, is shown. One can notice from the diagram that sources at higher declinations will cover a higher range of parallactic angle with respect to those at lower declinations.

Every other contribution can be included as a further matrix in Eq. 4.4. For example a baseline matrix $b_{i,j}(t)$ should also be considered when using the array just after a configuration change to correct for errors in the antennas position, i.e. in the baselines length. Or, a matrix T_i which includes the effects of the troposphere. Note that one such Jones' matrix J_i exists for each antenna i. The gain factors are hence antenna-based i.e. depends on the single instrument characteristics at the time of the observation.

Naming $V_{ij,source}$ the intrisic source visibility and $V_{ij,obs}$ the one obtained as the correlator output one can then write:

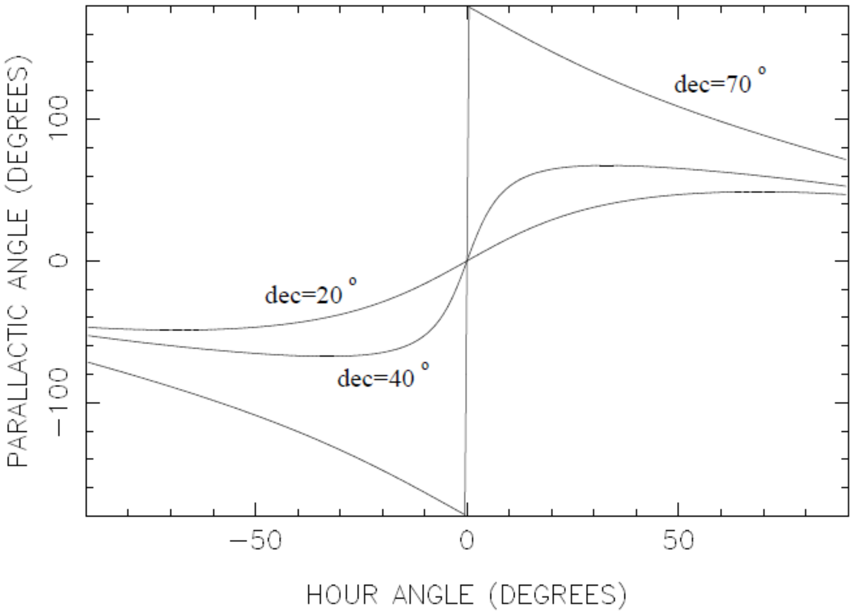

Figure 4.6: Example of parallactic angle trand as function of declination and hour angle for a telescope located at latitude 45°

$$V_{ij,obs} =< J_i \otimes J_j > V_{ij,source} \tag{4.8}$$

The aim of the calibration process is just to calculate the John's matrix to be applied to the target source in order to extract a correct scientific information. To do that one usually uses a visibility model based on the well-known properties of the calibrators:

$$V_{ij,obs} =< J_i \otimes J_j > V_{ij,model}$$

Calibration strategy

As previously discussed the first step of the calibration process is to define a model which describes the intrinsic visibilities of the primary calibrator. To do that one uses the CASA task SETJY which stores the model information in MODEL column of the measurement set. The NRAO web-page offers an EVLA Calibrator List. Moreover, constant monitoring programs are conducted in order to report any flux density variability. Thanks to its stability, 3C286 is highly recommended as flux density calibrator, but accurate flux densities can also be obtained by observing 3C138, 3C147 or 3C48 in some bands and configurations. To make the calibration as precise as possible, also avoiding problems linked to possible calibrators extension, visibility models have been implemented for all these sources in CASA. Flux densities can also be manually specified if needed. Our data have been calibrated using both 3C138 and 3C286 models in the appropriate band referring to the

Perley & Butler (2010) scale. Moreover, a reference antenna must be chosen. In fact, in order to measure phase differences between antennas in the array, one needs to fix a reference component whose phase is put to 0. For this purpose, it is convenient to select one of the most central antennas in the configuration, paying attention to avoid unstable instruments.

As already briefly mentioned, since new EVLA data are collected now in spectral lines mode, one needs to correct for the different response of a set of frequency channels. In order to do that a so-called bandpass calibration is required, which determines the visibility complex gains as function of frequency $B(\nu)$. The bandpass function does not strongly vary with time, allowing one to observe only once the calibrator during the entire run. Before one can proceed using the task 'BANDPASS' to correct for this effect, it is better to solve for an initial set of phase gains, in order to prevent decorrelation in computing the bandpass solutions. In figures 4.7 and 4.8 an example of amplitude vs channels plot of 3C286 at 5 GHz before and after the editing and bandpass correction are shown.

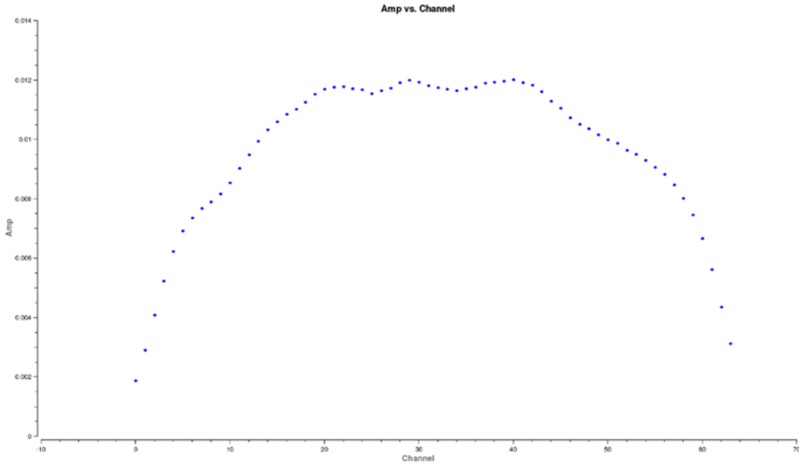

Figure 4.7: Plot of Amplitudes vs. Channels for source 3C286 before the Bandpass correction

In order to have a complete phase coherence in the visibilities, phase delays corrections are also needed. Beyond the geometrical delay due to the fact that wave-fronts reach each antenna in different moments, there could be differences in signal propagation times through the different electronic paths. This concerns not only interferometers, but within a single receiver there could be different effects on varying frequency and polarization. Correcting for these residual delays one can thus eliminate any trend of phases versus frequency channels. The task implemented in CASA to calculate these corrections is GAINCAL (gaintype 'K').

The next step is to derive corrections for the complex antenna gains, G(t). To do that, one makes use of a secondary calibrator whose position is as near as possible to the target

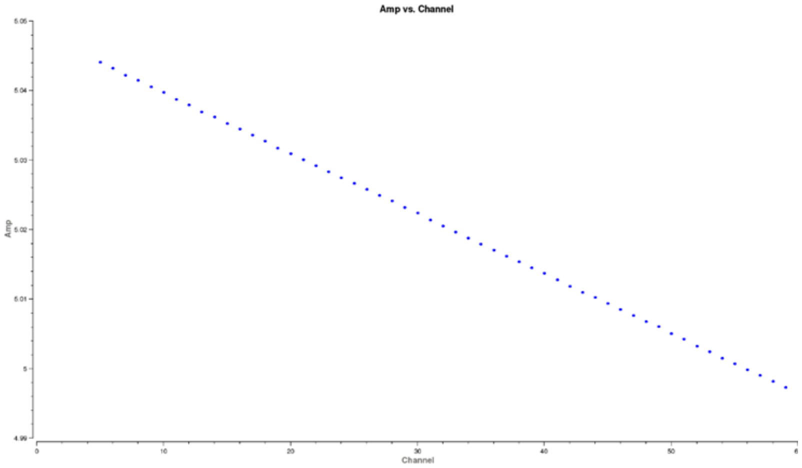

Figure 4.8: Plot of Amplitudes vs. Channels for source 3C286 after the Bandpass correction

source. The reason for that is that signal amplitudes and phases are altered when crossing the atmosphere. It is assumed that, if the secondary calibrator lies in the same direction as the target, it will suffer from the same signal variations as the scientific source and can then be used to correct for that. As already mentioned, the calibrator is observed in short intervals after the target scans just to have the most precise correction possible. In our schedules most phase calibrators were selected at about 2 to 5 degrees from target sources, and in all cases within 10 degrees. These solutions are calculated by using the task 'GAINCAL - gaintype G'.

The secondary calibrator does not necessary have a well known flux density. The model assumed for it is simply that of a point-like source of 1 Jy located at the phase centre. For this reason, one uses the system response calculated using the primary calibrator to rescale the gains obtaineted for the secondary calibrator in the last step. This is obviously done by assuming that the system response can be considered constant over the whole observing session. To do that one compares the model previously set in the MODEL column with the measured data and determines the gain values for the conversion to the absolute flux density scale. The task used to calculate the flux density scaling factors is called 'FLUXSCALE'.

Running each of the tasks previously mentioned, the software creates tables in which the solutions are stored. These tables are however not directly included in the data set, so that one can easily remove or change them. At the end of the calibration, one should apply the solutions to the data using the task 'APPLYCAL'. The corrected data are hence written in the CORRECTED DATA column of the data set without altering the DATA column. To verify the results of the calibration one should apply the solutions to the calibrators. Since the two calibrators are point-like sources located at the phase centre, we expect to see for both of them phases centred at 0 and constant amplitudes. Moreover, as already mentioned, no trend in frequency should be present. Note that the whole procedure is intended as iterative. This means that, if at the end of the process the results differ from the expectations or some more flagging is requested, one needs to repeat the whole calibration from the beginning.

Polarization theoretical outline

Also polarization data suffer from a number of effects that can alter and corrupt the signal, as always the antenna feeds do not have an ideal response and will introduce some errors. In particular, since feeds have a physical size and are often not perfectly orthogonally oriented, the antenna-feed combination causes a small amount of right circular polarization to show up in the left channel and vice versa (this is obviously true also for linear feeds). This spurious signals are commonly called leakage terms or D-terms and have to be removed in order not to contamine the scientific signal. For the majority of the extra-galactic radio-sources, in fact, the polarization percentage is typically few percent thus comparable with the instrumental plarization. It has been seen anyway that they are very stable over time since they depend on manufacturing imperfections of the feeds at least they can be considered constant over periods of days or few weeks.

The leakages D can be defined in the following way:

$$\begin{aligned} v_R &= E_R e^{-i\chi} + D_R E_L e^{i\chi} \\ v_L &= E_L e^{i\chi} + D_L E_R e^{-i\chi} \end{aligned} \tag{4.9}$$

where v_R and v_L are the voltages from the right circular polarization (RCP) and left circular polarization (LCP) channels, and E_R and E_L are the true electric fields. By computing the four correlations (RR, LL, RL, LR) from the previous expressions, neglecting second order terms one obtains:

$$\begin{aligned} V[RR] &= (I+V) + (Q+iU)e^{-i2\chi}d^*_{Rj} + d_{Ri}(Q-iU)e^{+i2\chi} \\ V[LL] &= (I-V) + (Q+iU)e^{-i2\chi}d_{Li} + d_{Lj}(Q-iU)e^{+i2\chi} \\ V[RL] &= e^{-2i\chi}(Q+iU) + (D_{R1} + D^*_{L2})I \\ V[LR] &= e^{-2i\chi}(Q-iU) + (D_{L1} + D^*_{R2})I \end{aligned} \tag{4.10}$$

It is worthwhile noting that, although in small percentage, the D-terms also corrupt the total intensity I. Typically though, this contribution is ignored and, unless one is interested in getting the polarization information, one does not proceed with the leakage correction.

To solve for instrumental polarization some standard strategies can be adopted. One can decide to include in the observation run one of the following calibrators:

1. Unpolarized calibrator - it allows with only a single scan to constrain D_R and D_L . In this case indeed Q and U are equals to zero and the only polarized signal is the one coming from the instrument itself and can easily be recognized:

$$\begin{aligned} V[RL] &= (D_{R1} + D^*_{L2})I \\ V[LR] &= (D_{L1} + D^*_{R2})I \end{aligned} \tag{4.11}$$

   In the calibrators monitoring program of the NRAO there are at least four sources recommended for this kind of calibrations (3C84 polarization $< 1\%$).

2. Polarized calibrator with known polarization - In this case indeed it is necessary to set the polarization parameters of the calibrator in the software inputs and observe it at least at two different parallactic angles. Only in this way the software will be able to isolate the spurious polarized signal from the total observed.

3. Polarized calibrator with unknown polarization - need to be observed at least in 3 scans for each run covering a parallactic angle range not smaller than 60°. Having at its disposal observations at different parallactic angles the software is able to disentangle between a fixed contribution coming from the instrument and a variable one which depends on the source parallactic angle. With this method the calibrator polarization is determined jointly with the leakage terms.

Even after having corrected for the leakage terms the intrinsic polarization angle is generally unknown. Indeed, in Eq. 4.10 a phase rotation term $e^{\pm(\Phi_R - \Phi_L)}$ multyplying the cross-hands equations has been left off. This term essentially represents the phase difference between the two orthogonally polarized channels R and L, and must be corrected in a further step. The parallel hand calibration ensures that this difference will be the same for each antenna, and equal to that of the reference antenna. For this goal a strong source with known polarization angle has to be observed, so that one can change the relative phase of the cross-hand channels to get the known angle for the source. We then tried to produce U and Q images without the leakages correction although aware of the noise high contribute. Unfortunately, the noise was too high to determine any reliable polarized information.

Polarization reduction

As shown in Sec. 4.2 our observations were carried out in filler mode and none of the previous strategies was followed. Anyway, in the AIPS cookbook (see section 4.6) the authors claim the possibility to solve for D-terms by using different sources, all of them covering the same parallactic angle range requested in method 3. For this reason we tried to test the latter possibility, in collaboration with the EVLA team. Unfortunately, since CASA is an on-going project, continuosly developed and tested, the EVLA software experts found a bug when combining visibilities from different sources and we could not proceed in this direction. As a last attempt, we also tried to apply method 2 to the single scan of the primary calibrator, even conscious of the small parallactic angle coverage. This way also led to unsatisfactory results. We also tried to calibrate the polarization angle without having removed the D-terms. Probably because of the high noise in the visibilities also this test did not produce the expected result.

Imaging and self-calibration

Once the calibration is succesfully completed, one can proceed with the image reconstruction. Since visibilities are the Fourier transform of the sky brightness distribution to create an image an inverse Fourier transform of the visibilities is needed. Moreover, antenna arrays are able to measure the visibility function at many spatial frequencies but not all. In fact, because of a finite number of antennas and a finite amount of integration time there will always be gaps or holes in its measurement. The set of spatial frequencies at which visibility measurements were made can be written in terms of a sampling function S(u, v).

$$V^{obs}(u,v) = S(u,v) \cdot V^{true}$$

To get the image one thus has to apply the inverse Fourier transform to the observed, calibrated visibilities. Designating with **F** the (inverse) Fourier transform operator one can write:

$$I^D = \mathbf{F}(V^{obs}) = \mathbf{F}(SV^{true}) = \mathbf{F}(S) * \mathbf{F}(V^{true}) = \mathbf{F}(S) * I^{true}$$

where $*$ stands for a convolution. The result of this mathematical operation is called Dirty Image. The Dirty Image is thus the convolution of the inverse Fourier transform of the sampling function with the 'true' brightness distribution; F(S) is commonly referred to as the "dirty beam" or the point spread function since, when the source is a point of unit amplitude at the phase tracking center, the visibility function is unity everywhere. The Dirty Map is very different from the real surface brightness of the sky. Many artificial features actually intervene to corrupt that.

In order to find out the real brightness distribution one has to perform an iterative process called 'cleaning'. For every step the program finds in the image the pixel corresponding to the maximum absolute surface brightness and associates to its position a delta-function (clean component or CC). A percentage of this CC is then convolved with the normalized dirty beam and subtracted from the image. A value of 10% is typically chosen to avoid the inclusion of radiation from secondary lobes of other near objects. This way one obtains what is called the RESIDUAL MAP. On the residual maps the algorithm looks for another peak and the cycle repeats until a pre-fixed condition is verified, that can be a maximum number of iterations or a noise threshold fixed by the user. One can also stop it interactively when the subtracted brightness begins to converge. Starting from the last residual map the program proceeds in restoring the image. This means to convolve the clean components found with a CLEAN BEAM (free from secondary lobes) to have at last the cleaned image. The CLEAN BEAM is normally a Gaussian with same FWHM of the main lobe of the dirty beam to preserve the resolution. This process can be carried out on either the whole image or on specific regions selected by the user. Note that extended sources are assumed to be representable as a combination of N separate point sources and so the same iterative process can be performed.

The first image one wants to produce is finalized to create a model for the self-calibration. This further calibration process is made to refine the solutions found for the target source with respect to the a priori calibration where corrections were averaged on the whole scan and obtained by using the secondary calibrator. It is called self-calibration just because it uses the data themselves to determine its own calibration.

The coherence time of the atmosphere is the time on which its variations are not significant, allowing radiation to propagate maintaining the same phase. This time depends on the wave frequency and will be particularly short for high frequencies. Despite this, during our scans, which last about 15 minutes, there could be fluctuations which could slightly alter the phases of the visibilities. To eliminate this effect self-calibration corrects phases on shorter timescales.

As the first image is concluded, the MODEL column of the MS file will be overwritten with the visibilities of the clean components found. Using the task GAINCAL one can then proceed with a new gain calculation to be then applied to the DATA column. At this point the next cleaning process will use the new CORRECTED DATA column to produce the image. Note that the self-calibration process can be repeated using time intervals shorter and shorter in order to reduce the gap between model and observations and improve the phase and amplitude corrections. Once the self-calibration is completed a last final image can be produced from which the scientific information can be extracted.

Following this procedure maps for all the sources were produced. In Fig. 4.9 the map of source 1103+11 (BAL) at 4.6 GHz is shown as illustrative example.

4.2.3 Observational parameters calculation

From the final cleaned map one can extract scientific information on the target source. Using the task 'VIEWER' it is possible to perform any kind of inspection on the image as

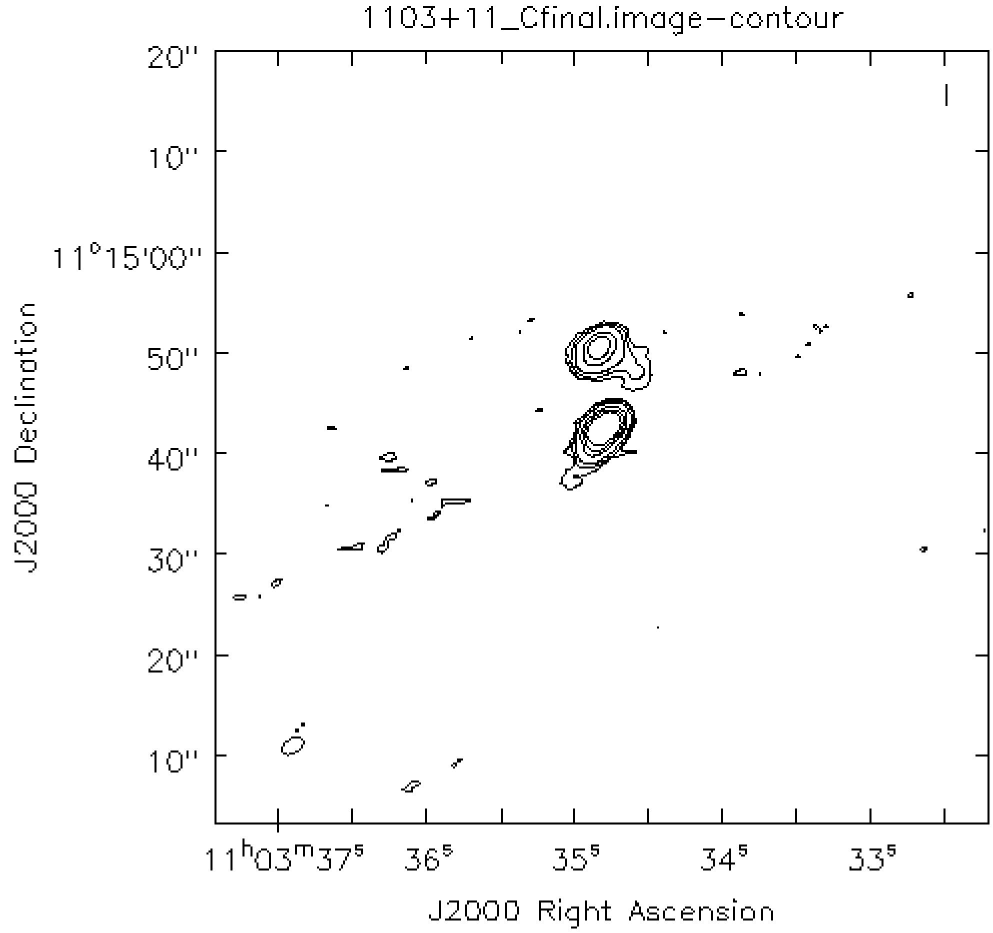

Figure 4.9: C-band map of BAL source 1103+01. The synthesised beam size is shown in the lower left corner of the map. Levels are multiples of the 3σ flux density value in mJy/beam with the following proportions 1, 2, 4, 16, 32, 64 ($\sigma = 310^{-5}$ mJy/beam).

CASA main tasks	
Data examination and editing	
listobs	Lists the summary information of a data-set
plotants	Produces a plot of the antenna configuration during the observation
plotms	Interactive graphic window where visibilities can be plotted and manipulated
viewer	Displays images (e.g. row data, cleaned maps, ...)
tflagdata	Flags selected visibilities
flagmanager	Organizes and creates beckups of the flag/unflag data
Calibration	
setjy	Fills the MODEL column of the MS with the absolute calibrator visibilities
gencal - antpos	Computes possible antenna position corrections
bandpass	Solves for frequency complex gains
gaincal	Solves for time dependent complex gains
fluxscale	Bootstraps the flux density scale from standard calibrators
plotcal	Plots calibration solutions contained in the selected table
applycal	Applies solutions to data
clearcal	Clears the CORRECTED DATA and MODEL column of the MS
Imaging	
split	Creates a visibility subset from an existing visibility set
clean	Inverts and deconvolves images with selected algorithm

Table 4.4: List of tasks used in the CASA software

well as statistical calculations. In order to obtain the flux densities for our sources we made use of both tasks IMSTAT and IMFIT. The first one is able to calculate statistical values of a region selected interactively. In particular, we measured in this way the integrated flux densities for our sources. On the other hand, the second one makes a Gaussian fit of the component within the selected region. In our case the objects appear almost always point-like and so one can better trust the fit. In figure the trend jmfit vs imstat is shown, done to understand if there are systematic differences between the two results. The error of these measurements was calculated by using the formula from Klein et al. (2003) for interferometric data.

$$\Delta I = \sqrt{(\Delta S_{calib} \cdot S)^2 + (\Delta S_{noise})^2 \cdot \frac{A_{src}}{A_{beam}}}$$

where ΔS_{calib} is the calibration error which represents the goodness of the calibration process and was calculated by measuring the visibilities standard deviation around the mean value for the flux density calibrator in question. ΔS_{noise} is the thermal noise which was calculated from the final target image. In particular we selected a wide sky region

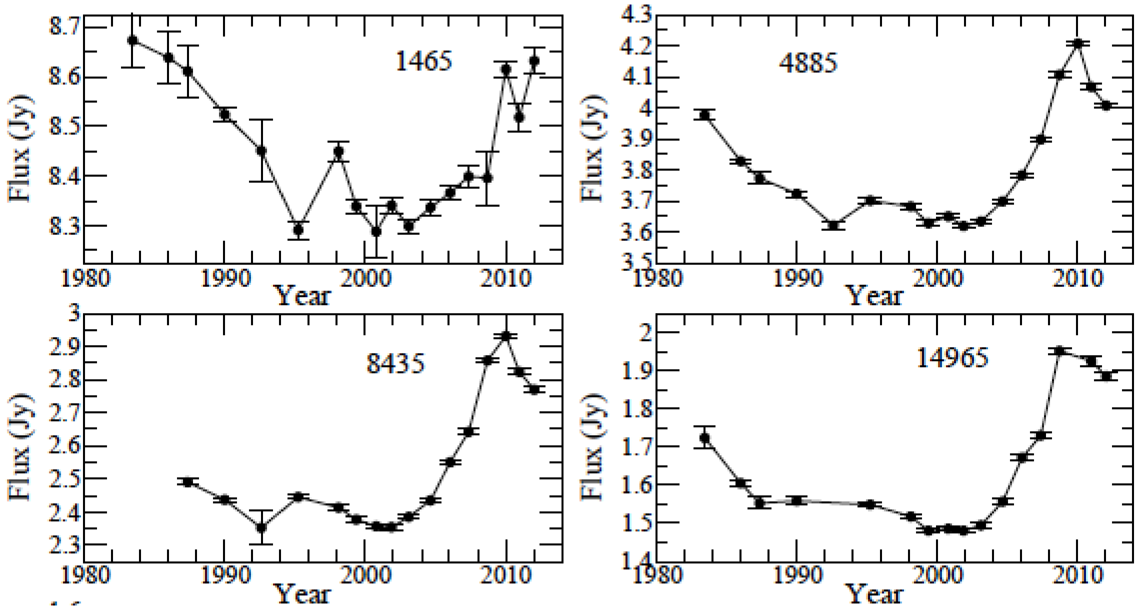

Figure 4.10: Flux density monitoring of source 3C138 at various frequencies carried out with the VLA (Perley & Butler 2013)

around the source lacking of field sources and measured with the task IMSTAT the flux density standard deviation from the mean value in Jy/beam. That value was taken as the thermal noise of the image. A_{beam} and A_{src} are respectively the beam area in pixels and the source area used for the flux density extraction. From this ratio we determine the number of beams contained in the source. For this kind of observations in terms of frequency and instrument one can avoid to consider a confusion error in the formula which, for synthesis imaging would be the result of uncleanable sidelobes of close sources.

As already told, 3C138 and 3C286 were used during this work as flux density calibrators. Although both objects belong to the list of suggested calibrators for VLA - EVLA observations due to their high flux density and small angular size, 3C138 has to be used with special care because it is known to be variable. In their VLA calibrators monitoring program confirmed this trend. 3C138 seems to have experienced in fact a violent flare beginning in 2003, reaching its peak in 2010 and now slowly fading down (see Fig. 4.10). The importance of the flare was greatest at higher frequencies, nearly doubling the flux density at 43 GHz. Perley & Butler (2013) fitted its spectrum with a cubic polynomial function for each of the 18 monitoring sessions available starting from 1983 until 2012.

$$logS[Jy] = a + b \cdot log\nu[GHz] + c \cdot log^2\nu[GHz] + d \cdot log^3\nu[GHz]$$

Since the visibility models in CASA refer to flux densities observed in a slightly different period respect to our observations, we decided to correct our flux densities a posteriori by exploiting the information by Perley & Butler (2012). We hence calculated a multiplicative correction factor by dividing the Perley & Butler (2012) value for 3C138 in the year 2010.9 - which is the closest date to our observing session - by the value used by CASA in the implemented model. The polynomial coefficients used to get the updated flux densities are quoted below (Tab. 4.5) as well as the flux densities and correction factors (Tab. 4.6).

Year	a	b	c	d
2010.9	1.0207	-0.5140	-0.1626	0.058

Table 4.5: Polinomial coefficients used to fit the spectrum of 3C138 computed by Perley & Butler (2013)

Frequency (GHz)	$S_{2010.9}$	S_{CASA}	Correction
4.86	4.07	4.27	0.9516
8.46	2.81	3.03	0.9296

Table 4.6: Comparison between the Perley & Butler (2013) flux densities and CASA modelled flux densities for 3C138. In the third column the correction to be applied are shown in order to consider the calibrator variations.

4.3 Effelsberg observations and data reduction

Figure 4.11: The Effelsberg parabola, Bonn

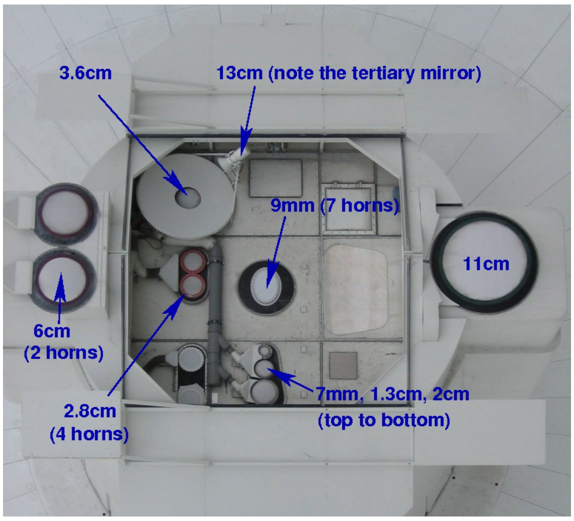

Figure 4.12: Image of the telescope receivers located at the secondary focus

With its diameter of 100 meters the Effelsberg single dish ($50^\circ 31' 29''$N $6^\circ 52' 58''$E - 319 m altitude) is one of the largest fully steerable radio telescopes in the world (see Fig. 4.11). It is operated by the Max-Planck-Institut für Radioastronomie (MPIfR) of Bonn but about half of the observing time is available to external astronomers.
It has a Gregorian configuration with a parabolic 100-m primary mirror and an ellipsoidal 6.5-m secondary mirror with an alt-azimuth mount. Thanks to a great variety of receivers located either in the primary or in the secondary focus, the telescope can be used to observe radio emission from astronomical objects in the frequency range from 300 MHz to 90 GHz in different observing modes from spectroscopy to continuum to high time-resolution measurements for pulsar observations and as part of several Very Long Baseline Interferometry (VLBI) networks.

Our observations have been taken in continuum mode during two runs: the first one in September 2011 and the second one in March 2012 (see Fig. 4.7).

Date	Frequencies (GHz)
September 2011	2.6, 4.85, 8.35, 10.5
March-April 2012	2.6

Table 4.7: List of observations

At all frequencies the telescope is supplied with circular feed horns which detect the incoming signal and then transfer it to the receivers. The feeds for the frequencies of interest are placed in the secondary focus (see Fig. 4.12) and have the following characteristics:

- 2.64 GHz (11.4 cm) : 1-horn receiver sensitive to frequencies from 2599.5 to 2679.5

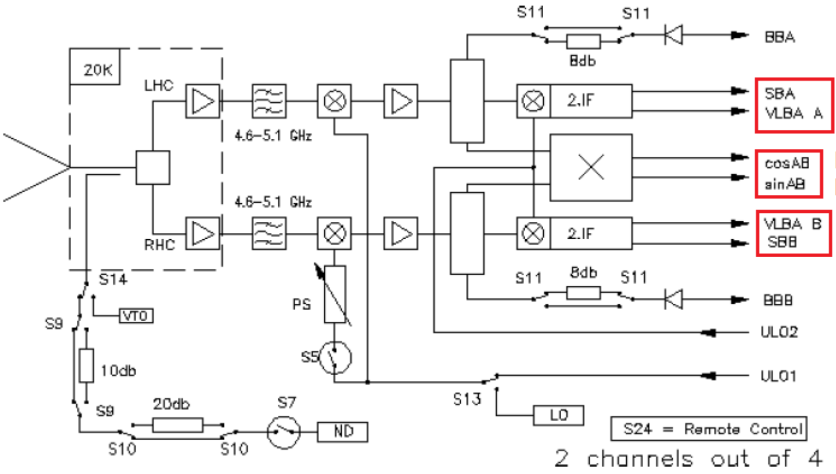

Figure 4.13: The 4.85-GHz receiver electronic scheme.

MHz. Together with the 18/21-cm receiver, it is equipped with a 8-bank polarimeter used to split the full band into 8 sub-bands of 10 MHz each.

- 4.75 GHz (6 cm) : 2-horn receiver provided with only one broad band ranging from 4600 to 5100 MHz.
- 8.35 GHz (3.6 cm) : 1-horn receiver provided with only one broad band ranging from 7950 to 9150 MHz.
- 10 GHz (2.8 cm) : 4-horn receiver provided with only one broad band ranging from 1030 to 1060 MHz.

In Fig. 4.13 the electronic scheme of the 4.85-GHz receiver is illustrated as an example. In red the four correlations outputs RR, LL, RL, LR are indicated, where R and L are the provided voltages from the right circular polarization (RCP) and left circular polarization (LCP) channels. As already said only the 2.64-GHz and the 18/24-GHz receivers are complemented by multiband polarimeter beckends. This facility has the great advantage of splitting the full band in more sub-bands giving the possibility to analyze signals from each of them separately. This is very useful in case there are interferences at very precise frequencies and one can decide to use only the clean sub bands for the study. In figure 4.14 the electronic scheme of the 8-Bank-Polarimeter and the channel distribution scheme are reported.

In our case at 2.64 GHz, in particular in the first sub-band (2604.5± 5 MHz), observations were heavily corrupted by the presence of RFI, probably from Airborne Warning and Control Systems (AWACS) aircrafts. For this reason we decided to exclude the entire sub-band from our work.

Channels	Output	Frequency of sub-band
1 2 3 4	TP A TP B cos A/B sen A/B	2604.5±5 MHz
5-8	...	2614.5 ±5 MHz
9-12	...	2624.5 ±5 MHz
13-16	...	2634.5 ±5 MHz
17-20	...	2644.5 ±5 MHz
21-24	...	2654.5 ±5 MHz
25-28	...	2664.5 ±5 MHz
29-32	...	2674.5 ±5 MHz
Full Band 33-36	...	2639.5 ±40 MHz

Table 4.8: Channels distribution scheme of the 11 cm 8-Bank Polarimeter

In Tab. 4.9 the angular resolutions, in terms of Full Width at Half Maximum (FWHM), for the frequencies of interest, are reported.

Frequency (GHz)	Bandwidth (MHz)	FWHM (arcsec)
2.64	80	265
4.75	500	146
8.35	1100	81
10.7	300	67

Table 4.9: List of FWHM varying frequency

Since the sources of our sample appear point-like to the Effelsberg telescope at these frequencies, the observational technique of CROSS-SCAN was used. This consists of tracing a cross on the target source moving the telescope along two perpendicular directions with the source located in the centre. The two axes of this cross are commonly called Lambda and Beta and can correspond to (see figure 4.15):

- Azimuth and Elevation, typically in case of point-like sources
- For slightly extended sources one can use the major axis of the object as reference and the one perpendicular to it. Note that this technique can only work if the source is elongated along one axis only; for more resolved objects mapping is required.

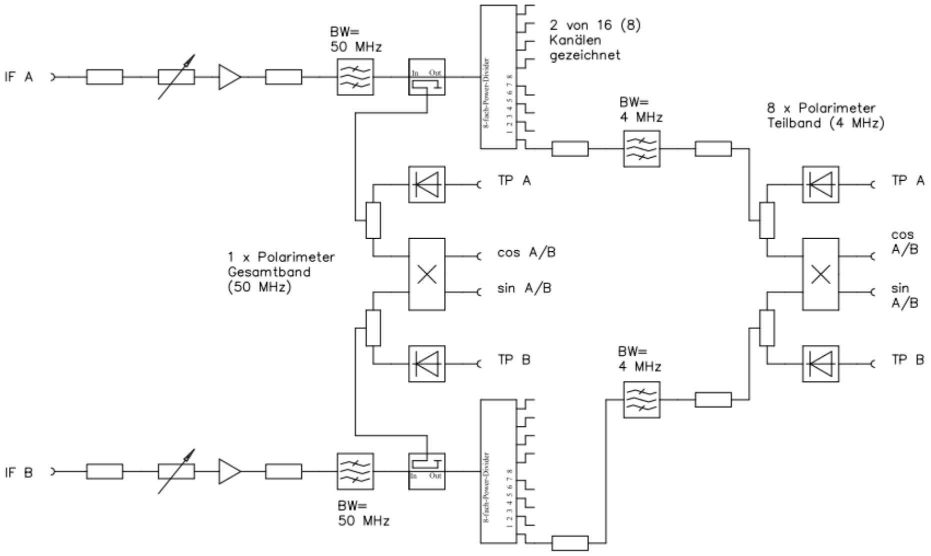

Figure 4.14: Electronic scheme of the 8-Bank Polarimeter available for 18/21cm-receiver and 11cm-receiver

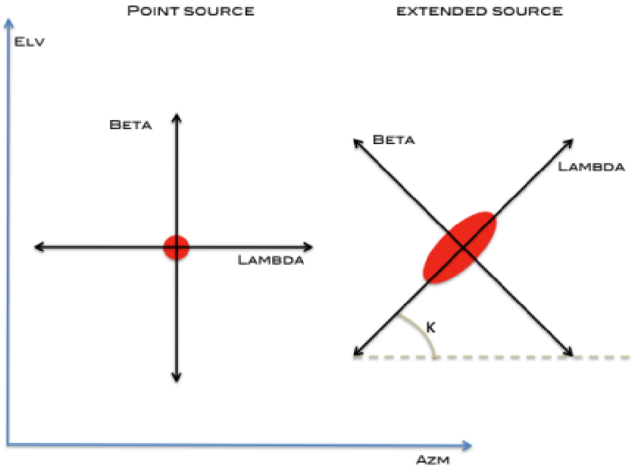

Figure 4.15: Schematic representation of the cross-scan technique

The spatial length of each sub-scan arm has been fixed at five Effelsberg beams, the middle one being centred on the source. The entire path is typically tracked in 30 seconds. The velocity of the telescope therefore depends on the observation frequency, it will be higher as the frequency decreases i.e. as the beam increases.

Each cross-scan observation is made of a different number of sub-scans depending on the exposure time required to detect the source as shown by the radiometer formula

$$\sigma = \frac{T_{syst}}{\sqrt{\Delta\nu \cdot \tau}}$$

where T_{syst} is the system temperature in Kelvin, $\Delta\nu$ is the observation bandwidth and τ is the integration time. Varying the exposure time, while other parameters are kept fixed, the noise of the observation is modified e.g. increasing τ a lower value of σ is reached and fainter sources could be detected.

In our observations, in order to detect also the fainter sources and to manage to find out the polarized flux densities, 50 sub-scans have been chosen corresponding to a total integration time of about 30 minutes.

Raw data are collected in MBFITS format files. They have been visualized and reduced by using the Toolbox software package developed at the Max-Planck-Institute für Radioastronomie in Bonn. The software has been upgraded in the last years to become more user-friendly. It allows one to check the goodness of data and to make the whole reduction in case of cross-scan observations. This process consists of selecting only good sub-scans and fit the signal with a Gaussian to extract the flux densities. In Tab. 4.10 the main commands used in our reduction are listed and briefly commented.

For the reasons explained in section 5.1 it is necessary to check by eye each sub-scan and decide whether its signal is representative of the real astronomical one or not. In presence of RFI we made use of the command 'SPIKE', available in the program, to actually try to correct for the precence of spikes. The task indeed divedes the x-axis in n infinitesimal intervals and looks for flux density fluctuations in the signal higher than a certain value, set in the input parameters, which is typically taken as 2σ. In case a spike is found the task proceeds with its removal and interpolates the boundaries. Although we are obviously talking of some kind of artificial data manipulation, the result of this kind of action can lead to great improvements in the flux density extraction. In Fig. 4.17 one example of subscan affected by radio-interference is presented. When the signal resulted too corrupted to be corrected we decided to delete it from the work. An example of these extreme cases is shown in Fig. 4.16. Here, probably due to heavy rain, some drops completely modified the signals. Another situation, which is worth to show, is the ground radiation. When the telescope is indeed pointing at low elevations, the celestial signal can be contaminated by thermal radiation coming from the ground. In this occurence, one

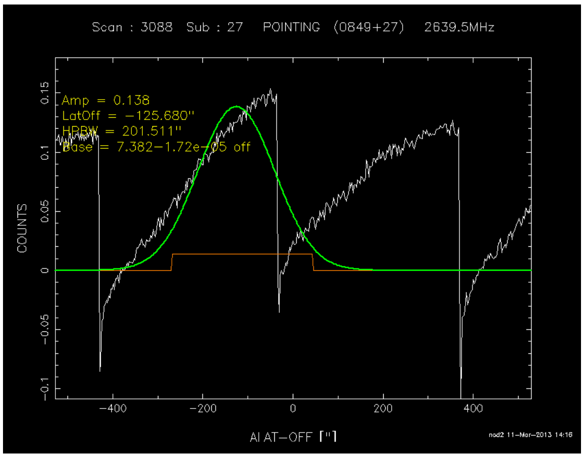

Figure 4.16: Example of sub-scan corrupted because of rain drops

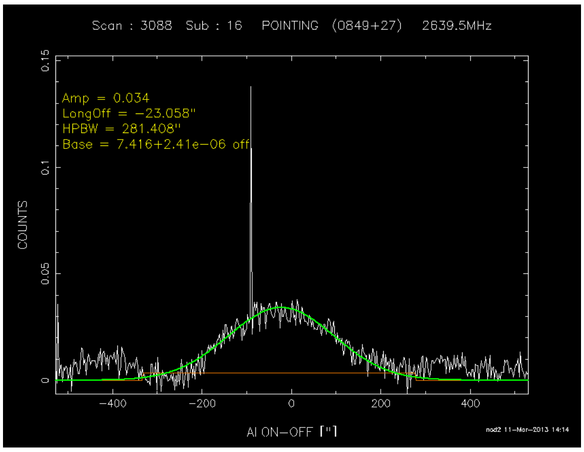

Figure 4.17: Example of sub-scan corrupted by strong RFI

wing of the Gaussian appears increased to values of the same order of the peak signal as shown in Fig. **??**. Thanks to the Toolbox task 'FCENT' it has been possible to force, in these cases, the Gaussian fit right in one position, corresponding to the peak position.

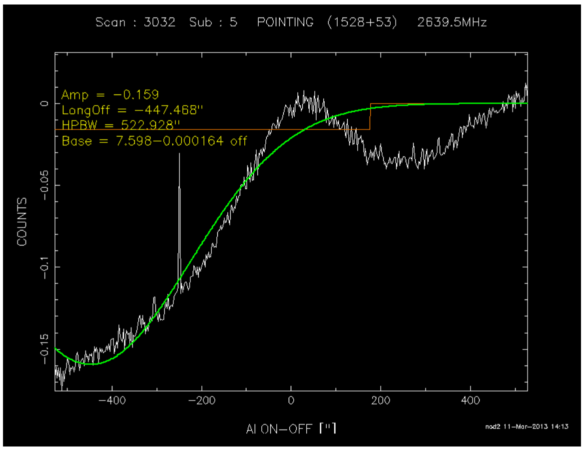

Figure 4.18: Example of sub-scan corrupted by thermal ground radiation

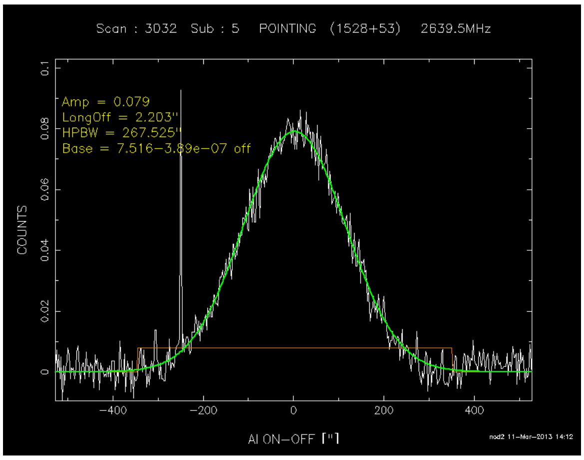

Figure 4.19: Imagine of the same sub-scan shown in Fig. **??** after the use of FCENT task

Once this selection was accomplished, the sub scans have been averaged in order to obtain the best signal to noise ratio and fit the signal as well as possible. During this operation the program also proceeds with the baseline subtraction, that is subtracting the background signal. The program allows one to select the polynomial order used for the subtraction. In order not to introduce artifacts we always used a linear order. The function used for the fit is a Gaussian, which can be considered in first approximation a good representation of the telescope beam. In output the software gives a .fit file containing all the information about the scan fitting results.

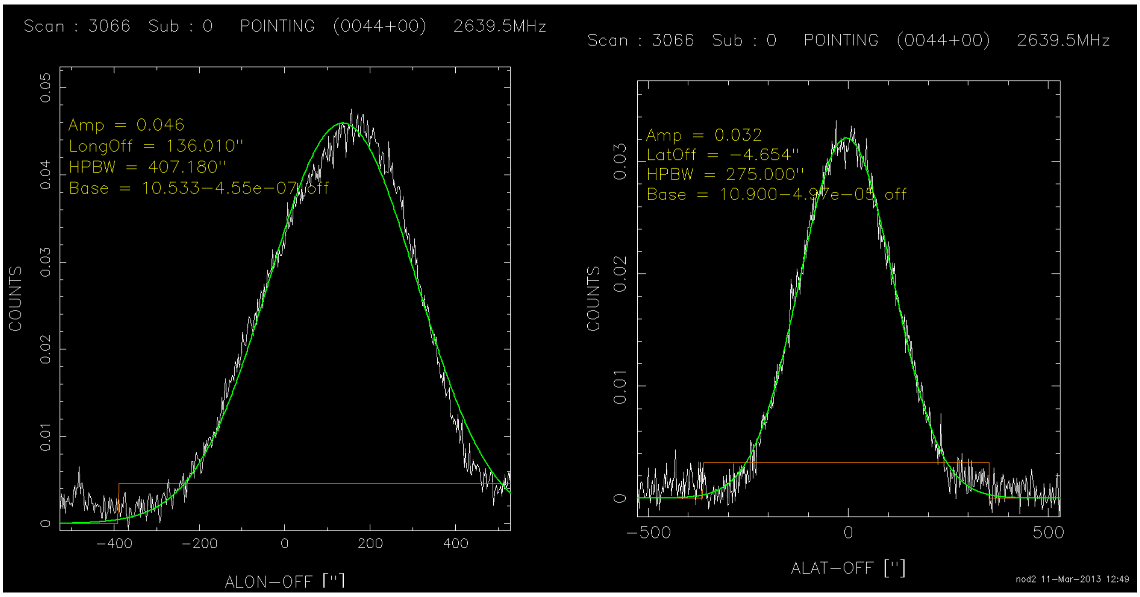

Figure 4.20: Example of source confusion due to low resolution power. Note the great broadening of the beam in azimuth direction (left panel) due the presence of the confusing source respect to the elevation direction (right panel).

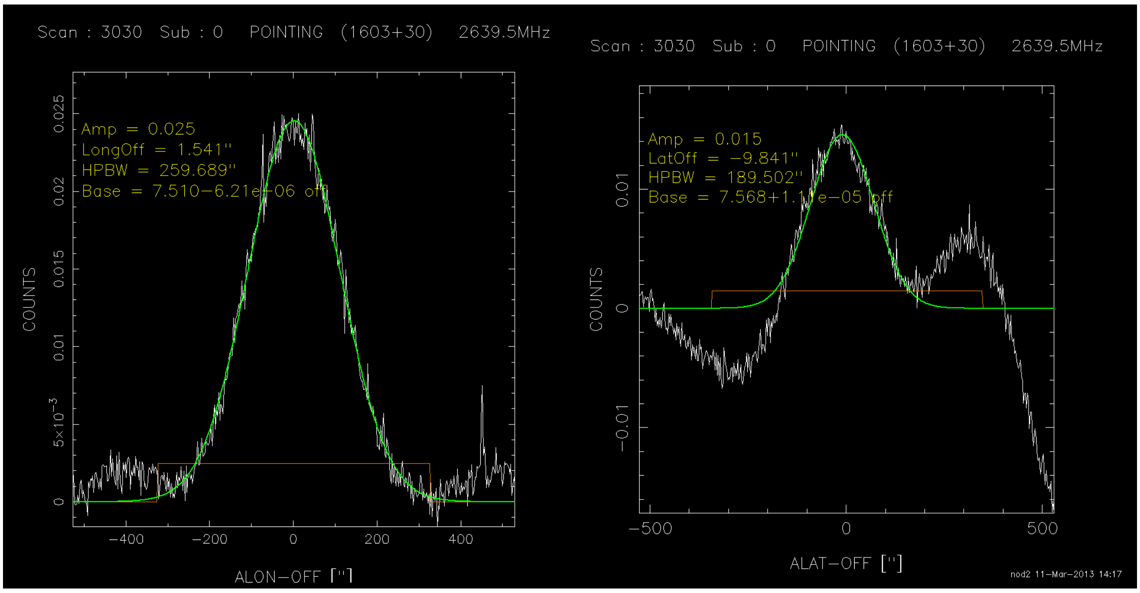

Figure 4.21: Example of source confusion due to low resolution. Note the presence in the beam in elevation direction (right panel) of a second source next to the target which cannot be avoided.

Task	Comment
scan=XXXX	scan number selection
sub=X	displays sub-scans X only
del=XXXX:x1,x2	delates sub-scans x1,x2 from scan XXXX
plot='/gif'	produces a gif-image XXXX.gif
pol=u or q	allows the selection of polarization channels
baseline=[no,0,1,2]	allows the choice of the degree of the function used for the baseline
aver	average over all longitude and latitude sub-scans
use='c[1]+c[2]/2'	allows the selection and combination of the channels available at that frequency
spikes=n	delate spikes due to interferences whose hights is greater than n*RMS (default n=3)
fcent=x	defines the starting point (centre) of the Gaussian fitting, 'x' in arcsec
header	MBFITS header visualization
rms	prints the rms of the observation

Table 4.10: List of tasks used in the Toolbox software

Because of the large beam of the Effelsberg telescope at our observation frequencies, we also had to pay attention to confusion sources, in order to extract correct flux densities. To do that, we made use of the NVSS catalogue and maps by Condon et al. (1998) which helped us in right interpretations. One clear example of this situation is reported in Fig. 4.21, where the presence of a second confusing source next to our target 1337-02 appears evident (see the NVSS map in Fig. 4.22. A similar case was found observing the source 0044+00 (Fig. 4.20). Here one could not even distinguish the two components because they appear completely tied under the same beam which obviously suffers of a considerable broadening (see the NVSS map in Fig. 4.23).

In order to correct for the flux density loss caused by the offsets due to the poynting, an IDL-program has been written during this work. In this script we have assumed the beam of the telescope to be well approximated by a Gaussian function:

$$f(x) = \frac{1}{\sigma\sqrt{2\pi}} \exp\left(-\frac{(x-x_0)^2}{2\sigma^2}\right)$$

with x_0 equals to 0 and $\sigma = FWHM/2\sqrt{2\ln 2}$. We have studied the variation of the flux densities as the offset changes. Given in input the offset obtained from the Toolbox reduction, the program calculates what the flux densities would have been if the source

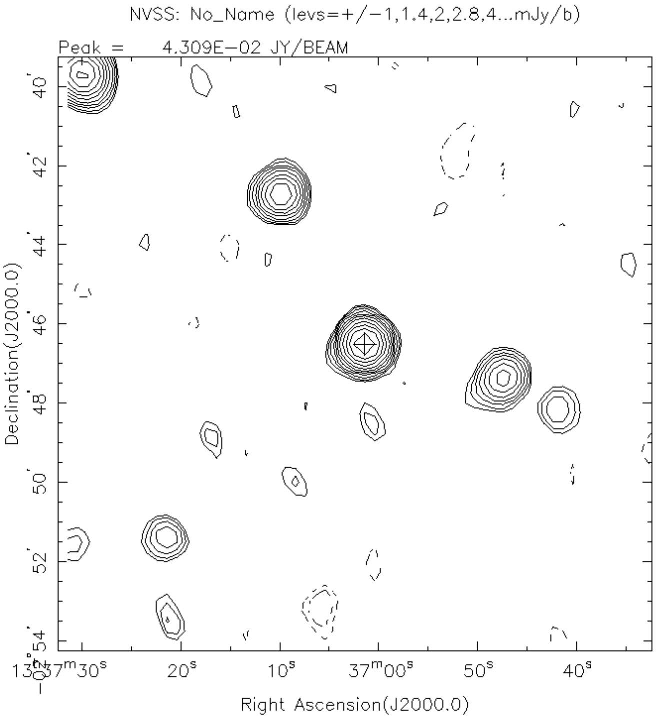

Figure 4.22: NVSS contours map of source 1337-02

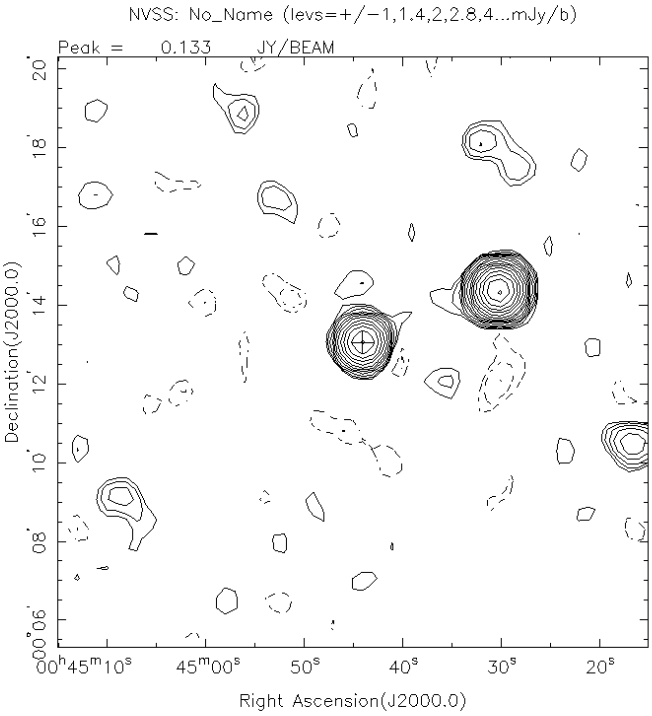

Figure 4.23: NVSS contours map of source 0044+00

was correctly pointed. Typically in literature an offset within the 10% of the beam width is tolerated.

4.3.1 Calibration and observational parameters calculation

To convert the flux densities from arbitrary units to Jansky units a calibration process has been made. Standard calibration sources were observed at regular intervals to determine the flux density scale. As already discussed for interferometric data, a good calibrator should be a bright point-like source with well-known flux density and no variability. In these observations 3C286 and 3C295 have been used, whose flux densities stability has been checked in Ott et al. (1993) and then confirmed by Kraus (priv comm). To determine the flux densities the Baars scale (Baars et al. 1977) has been used :

$$logS[Jy] = a + b \cdot log\nu[MHz] + c \cdot log^2\nu[MHz]$$

with a, b and c listed in Tab. 4.11

Source	a	b	c
3C286	1.480	0.292	-0.124
3C295	1485	0.759	-0.255

Table 4.11: Parameters for the calibrators flux density determination from Baars et al. (1977)

Tab. 4.12 shows the flux densities of the calibrators at 2.7 GHz, 5 GHz, 8 GHz, 10.7 GHz.

Source	$S_{2.7GHz}$ (Jy)	S_{5GHz} (Jy)	S_{8GHz} (Jy)	$S_{10.5GHz}$ (Jy)
3C286	10.50	7.30	5.38	4.40
3C295	12.20	6.36	3.65	2.53

Table 4.12: Calibrators flux densities computed following Baars et al. (1977)

The calibration factor is defined as:

$$CF = \frac{S_{Baars}}{S_{counts}}$$

where S_{baar} is the flux density in the Baars scale and S_{counts} is the flux density in counts obtained from the Toolbox reduction. The trend of the calibration factor as function of time is plotted Fig. 4.24. As already said, its value is expected to be nearly constant for any observation at the same frequency. Deviations from this constant trend can be interpreted as changes in weather conditions (indeed in both observing runs it was rainy and windy) or in instrument efficiency. The points have been interpolated using the least squares method and since the slope was small the mean values have been taken as reference for the calibration. In Tab. 4.13 the values found for each frequency are listed.

Frequency (GHz)	CF (mJy)	Standard deviation fit (mJy)
2.7 run2	1.59	0.005
2.7 run1	1.57	0.01
4.8 run1	1.15	0.02
8.4 run1	1.95	0.03
10.5 run1	5.56	0.09

Table 4.13: Results of the least squares fits performed on the calibration factors.

We notice that some difference in the mean values at 2.7 GHz has been found from run to run. The cause is probably linked, as mentioned before, to different weather conditions. To be precise data from each run have been calibrated using the respective CF. In order to make a coherent calibration, data regarding the calibrators have been reduced following the same procedure as the one of the target sources.

The last version of the Toolbox software gives in output for each scan the average values on all the sub-scans in both directions azimuth (ALON) and elevation (ALAT) with respective rms. To obtain the total flux densities, the arithmetic mean between ALON and ALAT has been calculated so that:

$$I = \frac{(I_{ALON} + I_{ALAT})}{2} \tag{4.12}$$

When during the reduction some sub-scans were eliminated because considered too corrupted, the weighted average has been used.

$$I = \frac{(I_{ALON} \cdot N + I_{ALAT} \cdot M)}{(N+M)} \tag{4.13}$$

where N and M are the numbers of sub-scans along the azimuth and elevation direction, respectively. In both cases to calculate the total rms the propagation of error has been used respectively with formule:

$$\sigma = \frac{1}{2}\sqrt{\sigma^2_{ALON} + \sigma^2_{ALAT}} \tag{4.14}$$

and

$$\sigma = \frac{1}{M+N}\sqrt{N^2\sigma^2_{ALON} + M^2\sigma^2_{ALAT}} \tag{4.15}$$

Once obtained all these values, the calibration factor has been applied to the target sources giving as result the flux densities in total power and its rms in Jy.

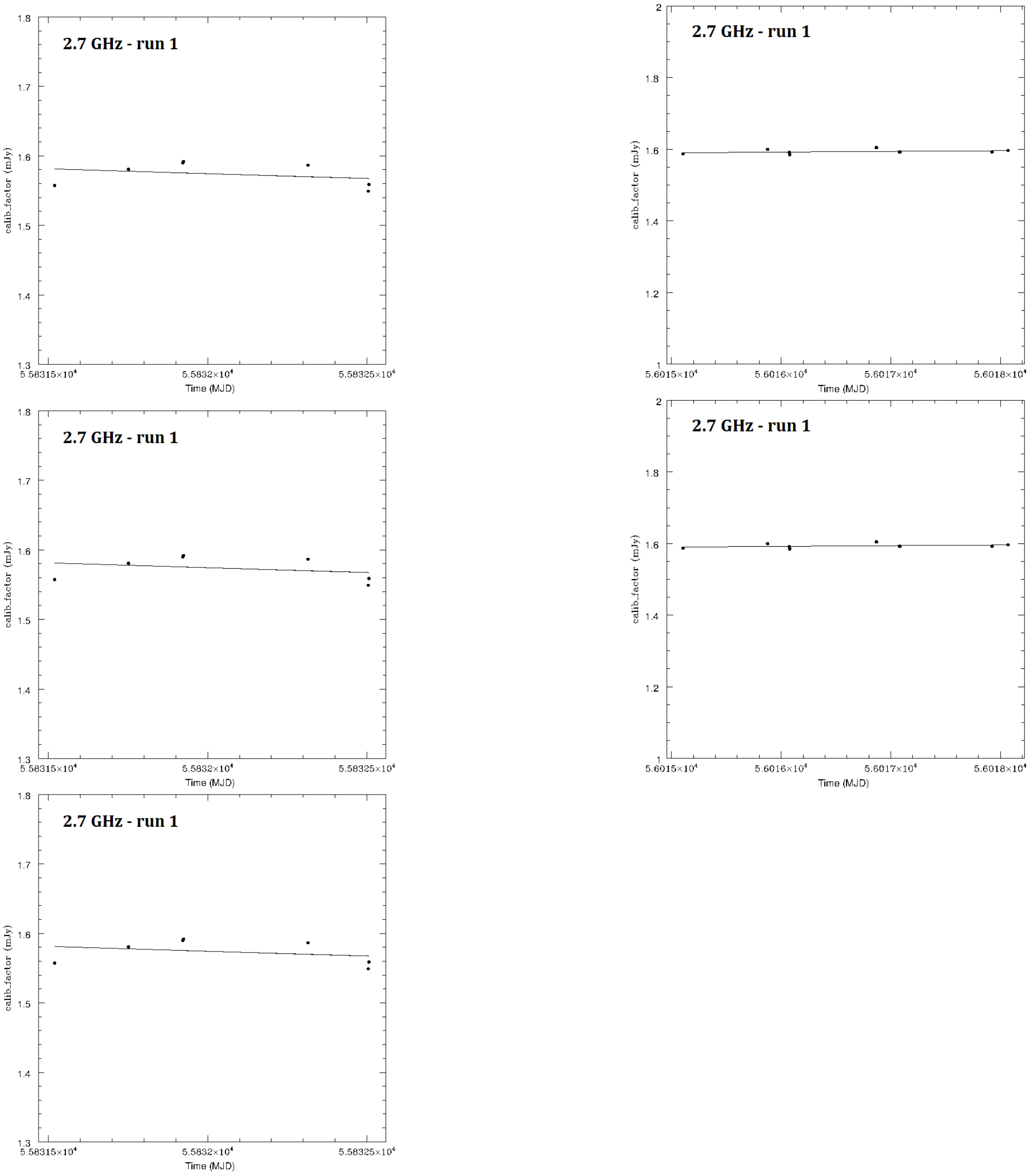

2.7 GHz - run 1

2.7 GHz - run 1

2.7 GHz - run 1

2.7 GHz - run 1

2.7 GHz - run 1

Figure 4.24: Least square fits of calibration factors vs time for the frequencies of interests.

To calculate the total error, different contributions have been taken into account. First of all, the thermal noise of the observation ΔS_{noise}, which is obtained, in this particular case, from the Toolbox outputs averaging azimuth and elevation values as previously explained. Secondarily, the calibration error ΔS_{calib} which represents the standard deviation of the least squares fit used to interpolate the Calibration Factor. This value is expected to be typically about 1% of the flux density. Lastly, the confusion noise ΔS_{conf} due to the emission from undetected sources in the beam of the telescope which limits the instrument sensitivity. All these values were considered using the following formula from Klein et al. (2003):

$$\Delta I = \sqrt{(\Delta S_{calib} \cdot S)^2 + (\Delta S_{noise})^2 + (\Delta S_{conf})^2}$$

Polarization

The procedure to obtain the polarized flux densities is quite the same as for the total power flux densities. For both cross-correlated signals RL and LR (U_{obs} and Q_{obs}) azimuth and elevation values were combined to obtain a unique result. Before we could proceed with the counts-Jansky conversion a further instrumental correction was applied. When observing a polarized flux density calibrator, such as 3C286, at different times, i.e. different parallactic angles χ, one should reproduce an ellipse in the imaginary plane Q-U. Remember in fact that the cross-hands signals depend on Q and U which are intrisic values of the source but also from χ which varies with time: $RL = e^{-2i\chi}(Q + iU)$ and $LR = e^{-2i\chi}(Q - iU)$. Consequently, by plotting various measurements of Q_{obs} against U_{obs}, both normalized to the total power flux density we expect the graph to be a circle centred in the origin of coordinates with radius equal to the polarization fraction of the source m. Assuming the curve to be a circle (ellipticity=0), we fitted the measurements and a clear offset between the circle centre and the origin of axes came to light (see Fig. 4.25). The cause of this gap is linked to the electronics of the receiver and can be considered as a spurius instrumental polarization which has to be removed.

Montenegro-Montes (2009) already studied this effect and having many available data from various observational campaigns made a systematic study the offset corrections to apply to the polarization channel signals. During our work we tried to find out confirmation of these offsets and we succeeded at least at 11 cm where we had more data. In Fig. 4.25 the best fit is shown. The offsets for 3C286 measured in this work and the ones calculated by Montenegro-Montes (2009) are presented in Tab. 4.14

Frequency (GHz)	U^{MM}_{offset}/I %	Q^{MM}_{offset}/I %	U_{offset}/I %	Q_{offset}/I %
2.7	0.20	1.66	0.1	1.60
4.5	0.60	0.00	-	-
8.4	-0.12	-40.30	-	-
10.5	-0.20	-0.40	-	-

Table 4.14: Positions determined for the origin of the Stokes circles in each frequency (Montenegro-Montes (2009))

The corrections were applied to U_{obs} and Q_{obs} as follows:

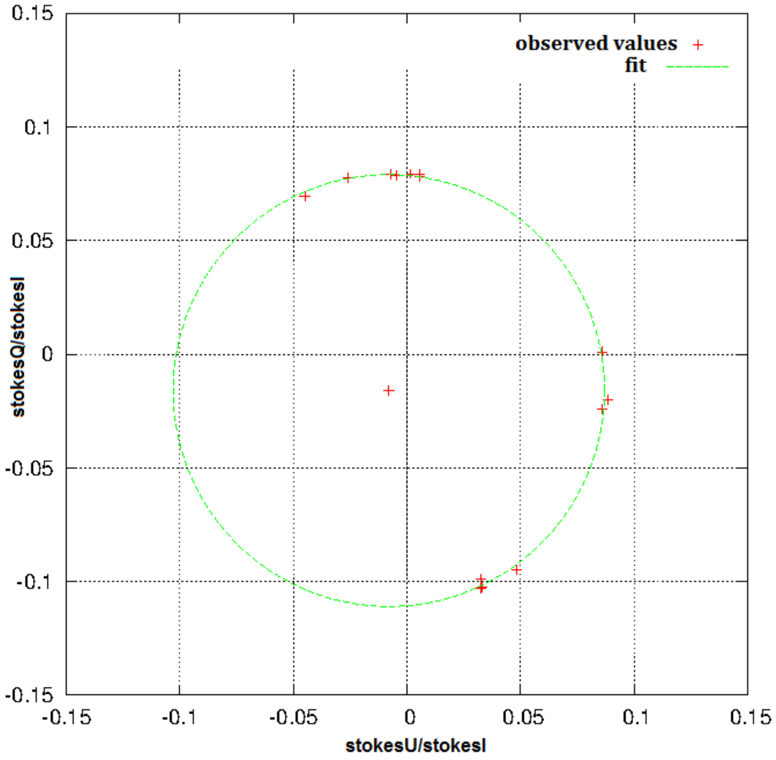

Figure 4.25: Stokes diagram at 11.0 cm showing the best fitted circle for 3C 286 using polarized flux densities measured during our observational campaigns.

$$Q = Q_{obs} - I \cdot Q_{offset}$$

$$U = U_{obs} - I \cdot U_{offset}$$

Once the corrections are applied, one can proceed with converting the observed polarized signals into physical units by using the same calibration factor calculated for total power measurements.

4.4 The data

In Tab. 4.15 and 4.16 the flux densities obtained from the data reduction are presented.

Name	Comp	$S_{2.6}$	$S_{4.85}$	$S_{4.86}$	$S_{8.35}$	$S_{8.46}$	$S_{10.5}$
0044+00		53.4 ± 2.0		32.1 ± 2.3		24.3 ± 4.0	20.6 ± 1.6
0756+37							
0816+48							
0842+06		37.2 ± 1.7		24.7 ± 0.6	18.5 ± 0.8		
0849+27		45.0 ± 2.0		27.6 ± 0.7	21.7 ± 0.6		
0905+02		96.4 ± 1.8					
0929+37		30.3 ± 1.7		30.5 ± 0.7		30.2 ± 0.9	
1014+05		42.2 ± 2.1				22.5 ± 1.6	
1040+05							
1054+51		32.2 ± 1.7					
1102+11		68.0 ± 1.9				17.6 ± 2.7	
1103+11				90.6 ± 6.8		66.3 ± 11.0	
	A			16.8 ± 1.2		7.0 ± 1.1	
	C			72.9 ± 5.5		55.1 ± 9.1	
1129+44		69.6 ± 1.7					
1159+01							
1159+06							
1229+09							
1237+47		57.2 ± 1.7					
1304+13		32.6 ± 1.7					
1327+03		90.0 ± 2.0		75.4 ± 4.4		55.9 ± 4.2	
1335+02		86.5 ± 1.8					
1337-02		65.5 ± 1.9		38.1 ± 1.8		14.8 ± 1.0	
1404+07				194.7 ± 9.5		183.6 ± 12.8	
1406+34							
1603+30		31.7 ± 1.7		35.1 ± 0.9		27.3 ± 0.8	
1624+37		36.3 ± 1.7					

Table 4.15: BAL QSO sources flux densities measured during this work expressed in mJy. Flux densities at 4.86 and 8.46 GHz are from the JVLA; those at 2.6, 4.85, 8.35 and 10.5 GHz are from the Effelsberg telescope. Column 2 specifies the component of the source following the classification by Bruni et al. (2012).

Name	Comp	$S_{2.6}$	$S_{4.85}$	$S_{4.86}$	$S_{8.35}$	$S_{8.46}$	$S_{10.5}$
0014+01							
0029-09		41.4 ± 1.8		41.9 ± 3.0		33.1 ± 5.5	
0033-00		30.9 ± 1.8	20.9 ± 0.9		13.4 ± 0.7		
0103-11		51.0 ± 2.0		37.2 ± 2.9	30.2 ± 0.8		
0124+00							
0125-00							
0152+01		23.3 ± 2.1				8.0 ± 1.4	
0154-00		232.5 ± 3.1				85.5 ± 15	
0158-00				65.0 ± 2.9		43.4 ± 8.0	
0750+36		84.0 ± 1.7		59.8 ± 2.7		48.1 ± 8.9	
1005+48							
1322+50							
1333+47		35.8 ± 1.9		21.6 ± 1.5		16.8 ± 2.3	
1401+52				30.7 ± 2.4		21.7 ± 1.7	
1411+34							
1411+43							
1502+55							
1512+35							
1521+43							
1528+53		127.3 ± 1.8		64.7 ± 3.4			
1554+30		39.7 ± 1.7		37.4 ± 1.9		31.9 ± 2.8	
1634+32							
1636+35		101.8 ± 1.9				55.8 ± 3.8	
1641+33							
1728+56					33.2 ± 2.3		
	B					20.4 ± 1.4	
	C					12.34 ± 0.8	
2109-07							
2129+00		38.7 ± 1.7		30.4 ± 0.8		22.4 ± 0.7	
2143+00		35.6 ± 1.7		49.4 ± 1.3		49.4 ± 1.6	
2238+00							
2244+00							
2248-09							
2331+01		28.0 ± 1.8		21.1 ± 1.3		17.0±1.9	
2346+00		52.2 ± 1.8		58.4 ± 1.6		61.0±2.0	
2353-00		40.7±1.7			18.9±0.7		

Table 4.16: Flux densities of non-BAL QSOs measured during this work expressed in mJy. Flux densities at 4.86 and 8.46 GHz are from the JVLA; those at 2.6, 4.85, 8.35 and 10.5 GHz are from the Effelsberg telescope. Column 2 specifies the component of the source following the classification by Bruni et al. (2012).

Chapter 5

Results

As previously explained the study of BAL QSO radio emission can be used as an additional diagnostic tool to explore the dichotomy BAL/non-BAL QSOs. In fact, it can be crucial to constrain some source properties such as age, magnetic field, local column density and orientation, providing new means of interpretation. In this chapter we present our results on the analyses performed during this thesis.

5.1 Spectral analysis

The study of the synchrotron spectra can be used to deduce much physical information about radio sources. In particular, one can investigate the radiative age of the brightest component contributing to the integrated flux density of the source (Murgia et al. 1999). Synchrotron ageing analyses have been successfully used in literature to estimate the radiative ages of radio sources. In particular, these analyses have been applied to CSS/GPS sources, revealing that these have been radiating for 10^3 to 10^5 years. This is about 1000 times shorter than normally found for classical extended radio galaxies (Mack et al. 1998, Parma et al. 1999). In this thesis we have performed a spectral study and ageing analysis -when possible- of the entire BAL and non-BAL QSOs samples looking for answers on their structure and radiative lives. In this chapter the theoretical background, as well as the analysis approach and results found will be discussed.

5.1.1 Spectral models

The detailed study of the electrons population of a radio source is essential to understand the physical environment and phenomena within the source itself. As already explained in fact, electrons are considered to be responsible for the majority of the non-thermal radiation observed. In Chapter 1 we have mentioned the main conditions that can alter the pure synchrotron power-law spectra. Here we want to describe in a more specific way some models which have been developed during the years to physically relate the curvature of the synchrotron spectrum to the age of the radiating particles leading to a method now called "spectral ageing" (Kardashev 1962; Kellermann 1964; Pacholczyk 1970; Jaffe & Perola 1974). Although in first approximation radiative losses always cause a steepening of the power-law spectrum, the precise shape of the high-frequency spectrum tail is indicative of a peculiar energy input evolution within the source. This kind of analysis thus help to put some constraints on the AGN picture, in terms of how and how much the energy is replenished from the central source.

As already seen in Eq. 1.12 the radiation spectrum of an electron population derives from its energy distribution. For this reason, the starting point, from which every kind of spectral model develops, is the assumption of a distribution of energies for the electron population at a given point of the source and at a given initial time N(E, $\vec{r}$, t_0). By then knowing each energy loss and gain contribution of the electron population dE/dt, as well as the electrons replenishment q(E, $\vec{r}$, t) and depletion p(E, $\vec{r}$, t), one can study the evolution of the distribution N(E, $\vec{r}$, t) at a generic time. Typically, one chooses, for simplicity, to assume a uniform and isotropic distribution, in order to exclude the space dependence in all terms which then become N(E, t), q(E, t), p(E, t). One has, anyway, to pay attention to adopt this approximation which can sometimes be too rough. Neglecting the space dependence in the energy distribution of the particles, one can hence write the most generic continuity equation in a one-dimensional energy space as follows (Kardashev 1962):

$$\begin{aligned} \frac{\partial N(E,t)}{\partial t} = {} & \alpha_1(t)\frac{\partial}{\partial E}\left(E^2\frac{\partial N(E,t)}{\partial E}\right) \\ & +\frac{\partial}{\partial E}\left(-\alpha_2(t)E+\beta(t)E^2\right)N(E,t) \\ & +q(E,t) \\ & -p(E,t) \end{aligned} \tag{5.1}$$

In this expression, $\alpha_1(t)$ represents the random acceleration by the Fermi mechanism, $\alpha_2(t)$ represents instead the systematic acceleration by the Fermi mechanism and the energy loss by adiabatic expansion, $\beta(t)$ stands for the synchrotron losses $\beta = c(Bsin\theta)^2$, q(E, t) is the function describing the number of particles with energy E injected in the region per unit time and per unit energy interval, p(E, t) represents, on the contrary, the number of particles with energy E removed from the region. This last term p(E, t) can also be substituted by the expression $N(E,t)/T_{life}$, in which T_{life} represents the lifetime of the electron within the emitting region.

In case of particle equilibrium the terms q(E, t) and p(E, t) are equal to zero and the equation reduces to:

$$\begin{aligned}\frac{\partial N(E,t)}{\partial t} &= \alpha_1(t)\frac{\partial}{\partial E}\left(E^2\frac{\partial N(E,t)}{\partial E}\right)\\ &= \frac{\partial}{\partial E}\left(-\alpha_2(t)E+\beta(t)E^2\right)N(E,t)\end{aligned} \tag{5.2}$$

To the contrary, one can discuss the sink function p(E, t) on the basis of the confinement time and particle interactions and one has to include some injection process q(E, t). One can thus consider two sorts of situation:

- particles are injected altogether in the radio source at one initial moment $t_0 = 0$ with an energy spectrum N(E, t_0) so that $q(E,t) \neq 0$ only for $t = t_0$,
- particles are continuously replenished by the central source so that q(E, t) is always $\neq 0$

In both cases, the energy distribution of the injected electron populations is assumed to be well described by a power law as suggested by observations:

$$N(E,t) = N_0E^{-p} \tag{5.3}$$

The acceleration mechanism at the basis of this kind of distribution is thought to be in first approximation the Fermi I mechanism. In particular, the energy distribution index p predicted by this model is equal to 2, thus giving a power distribution with $\alpha = 0.5$. By studying the details of the Fermi mechanism, such as the thickness of the shock, a wider energy distribution index is found.

A global solution of the continuity equation is inevitably too elaborated. For this reason, we will here only examine some peculiar cases which consider different evolutions of the supply of the energetic particles.

Continuous Injection model (CI)

In this model it is supposed that the source is continuously replenished of fresh relativistic particles and thus it is usually considered the best model to describe an active radio source. In this case the continuity equation includes the injection term q(E,t) and can be written as follows:

$$\frac{\partial N}{\partial t} = \beta\frac{\partial}{\partial E}(E^2N) + qE^{-p} \tag{5.4}$$

where $q(E,t) = qE^{-p}$ with q supposed to be independent from time.
Assuming the injection to start at an initial time t_0 the minimum break energy at a certain time t is:

$$E_b^{min} = \frac{1}{\beta(t-t_0)} \tag{5.5}$$

If N(E,0)=0 is assumed as initial condition, the solution can be written as:

$$N(E,t) = \frac{qE^{-(p+1)}}{(p-1)\beta}\left[1-\left(1-\frac{E}{E_b}\right)^{(p-1)}\right] \quad for\ \ E < E_{break} \tag{5.6}$$

$$N(E,t) = \frac{qE^{-(p+1)}}{(p-1)\beta} \quad for\ \ E > E_{break} \tag{5.7}$$

By studying the asymptotic trends of the solution one finds that:

$$N(E,t) \approx qtE^{-p} \qquad for\, E \ll E_b \tag{5.8}$$

$$N(E,t) \approx \frac{qE^{-(p+1)}}{(p-1)\beta} \qquad for\, E \gg E_b \tag{5.9}$$

This means that at low frequencies the number of particles per unit volume N(E, t) grows linearly with time coherently with the fact that they are continuously replenished. At high frequency instead the slope of the power-law increases by one unit (p+1) independently of time. The radiative losses are in fact balanced by the rate of injected particles so that the spectral shape remains unchanged.

Once the energy distribution has been modeled, one can proceed with the power spectrum calculation following Eq. 1.12. In particular, it will also show two different trends like the energy distribution, before and after the break frequency ν_b:

$$P(\nu) \propto \nu^{-\alpha} \quad for\ \ \nu < \nu_b \tag{5.10}$$

$$P(\nu) \propto \nu^{-(\alpha+0.5)} \quad for\ \ \nu > \nu_b \tag{5.11}$$

Note that this model does not include the effects of possible energy losses due to the expansion of the source or magnetic field modification with time which can however be important, especially in case of young sources. Some variations of the simple CI model have hence been studied which take into account these effects (Kardashev 1962, Murgia et al. 2008):

- The *Continuous Injection + Expansion model (CIE)* considers the emitting source to expand adiabatically at a constant rate and the magnetic field to be frozen into the plasma thus changing according to flux conservation.

- The *Continuous Injection + Magnetic field model (CIm)* considers again the emitting source to expand adiabatically but assumes the magnetic field to be always in equipartition with the particles energy density.

Single injection models

In contrast to the previous model, one can imagine a situation in which the electrons are injected into the radio source in a single event at a time t_0 and remain confined within it. In this case, the injection term in the continuity equation q(E, t) will be always 0 after t_0. The only term which survives is thus the synchrotron loss term and the equation reduces as follows:

$$\frac{\partial N}{\partial t} = \beta \frac{\partial}{\partial E}(E^2 N) \tag{5.12}$$

The solutions obtained are the following:

$$N(E,t) = \frac{N_0 E^{-p}}{(1-\frac{E}{E_b})^{2-p}} \quad for \quad E < E_b$$

$$N(E,t) = 0 \quad for \quad E > E_b$$

This means that an electron of even infinitely large energy must, within some finite time scale, reduce its energy to a value $\leq 1/\beta t$. Hence, the spectrum will be almost equal to the initial one for $E < E_b$ but will show a sharp decrease in the amount of high-energy electrons for $E > E_b$.

Remembering that $E_b \propto (B sin\theta)^{-1}$, the precise trend of the spectrum will depend on the assumptions made on the pitch angles θ. In general one assumes that the angle distribution can be considered isotropic. What makes the difference between the various models is instead how much that angle is considered to vary with time:

- The Kardashev-Pacholczyk model (KP, Kardashev 1962; Pacholczyk 1970) assumes a constant pitch angle for the accelerating particles. This, in practice, is equivalent to assume a time-scale for the isotropisation of the electrons much longer than the radiative timescale. Following this model, electrons are divided in different populations each one with its own pitch angle and its own break frequency. In particular, electrons with $\theta = 90°$ have the lowest break frequency, while electrons with $\theta = 0°$ have the highest break frequency.

- The Jaffe-Perola model (JP, Jaffe & Perola 1973) assumes instead that the angle distribution continuosly varies with time. This means that each particle can experiment a large number of angles on shorter time scales than the radiative one. In this case,

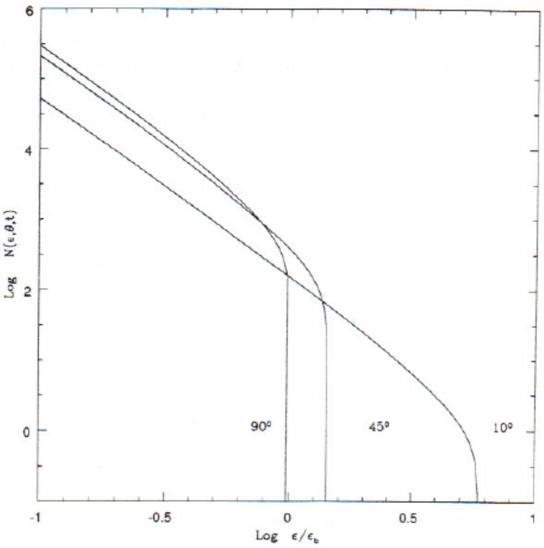

Figure 5.1: Spectral trends of the KP model by varying the pitch angle

there will be only one general population with one only break frequency. Here the expression of the break frequency can be simplified by making the mean value of $sin\theta^2$:

$$< sin\theta^2 >= \frac{1}{4\pi}\int_0^{2\pi}\int_0^{\pi} sin^3\theta d\theta d\phi = \frac{2}{3} \tag{5.13}$$

$$E_b^{JP} = \frac{1.5}{bB^2 t} \tag{5.14}$$

The different assumptions on the pitch angles of the electron population naturally influence the power spectrum as well. In particular, the main distinction between JP and KP models lies in the fact that the break frequency ν_b does not show the same dependence on the pitch angle θ for both models:

$$\nu_{b,KP}(\theta) = Cost \cdot (Bsin\theta)^{-3} t^{-2} \tag{5.15}$$

$$\nu_{b,JP}(\theta) = 2.25\, Cost \cdot (B)^{-3}(sin\theta) t^{-2} \tag{5.16}$$

with

$$Cost = \frac{C_\nu}{C_E^2} \quad , \quad C_\nu = 6.27 \cdot 10^{18} (c.g.s.) \tag{5.17}$$

One can see from the former expressions, that ν_b^{JP} has a maximum value in correspondence of $\theta = 90°$ beyond which the emission is totally suppressed. To the contrary, in the KP model, the radiation power is never equal to 0. In fact, for $\theta \rightarrow 0°$ $\nu_b^{KP} \rightarrow \infty$. For

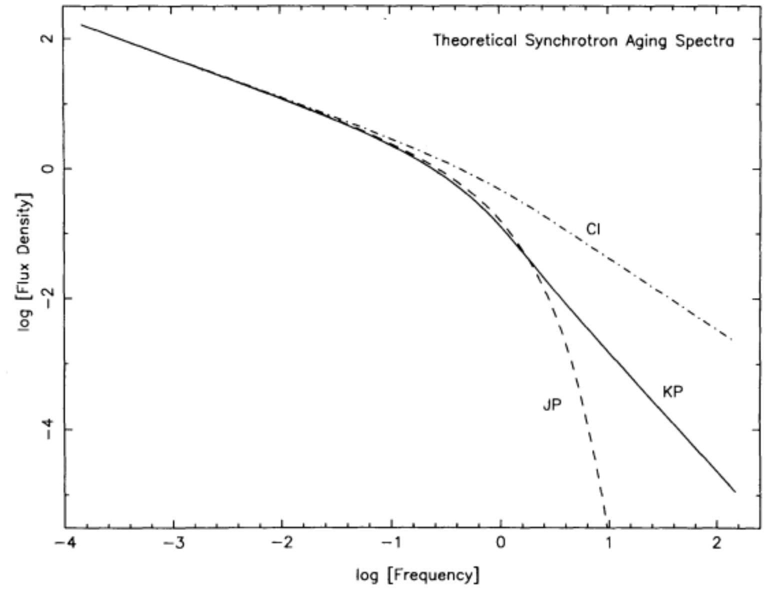

Figure 5.2: Example of theoretical spectral shapes corresponding to different models. The CI model shows the flattest spectral trend due to the balance between synchrotron losses and continuous injection. To the contrary the JP model exhibits a very sharp cut-off at high frequencies. Finally, the KP model shows an intermediate steepness due to the superposition of electron populations with different break frequencies.

frequencies beyond ν_b^{KP}, the spectrum steepens but still remains a power-law with spectral index $(\frac{4}{3}\alpha+1)$. In Fig. **??** some theoretical spectra, corresponding to different models, are shown.

CI model with injection power-off (CIOFF)

The CIOFF model describes a source which is subject, after a certain life time, to a switch-off of the central engine. In particular, after its birth, the source is assumed to experiment a continuous injection phase in which the central engine fuels it at a constant rate. During this period t_{CI} all the considerations done for the CI model are valid: the radiation spectrum has a power-law shape with a break frequency ν_b becoming lower and lower as the time passes. For some reason, at the time t_{CI} the nuclear energy supply is supposed to power off. In this 'dying phase', of duration t_{OFF}, a new break frequency $\nu_{b,high}$ appears, beyond which the radiation spectrum drops exponentially.

The continuity equation for this kind of situation can be written as follows:

$$\frac{\partial N}{\partial t} = \beta \frac{\partial}{\partial E}(E^2 N) + q(E,t) \tag{5.18}$$

with

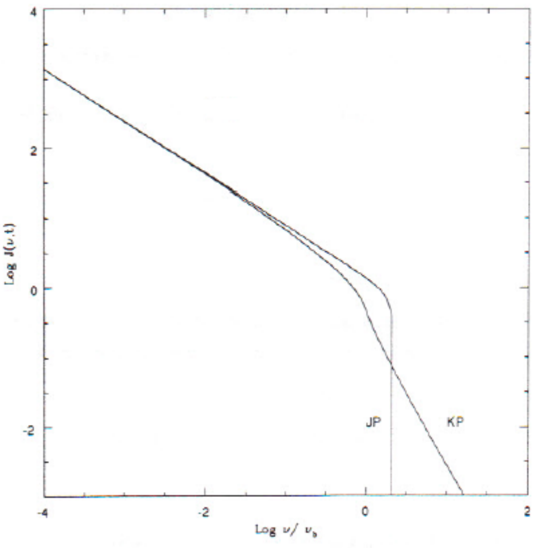

Figure 5.3: Spectral trends for JP and KP models for a fixed value of p=2.5

$$q(E,t) = q(t)E^{-p} \qquad for \;\; t < t_{off} \tag{5.19}$$

$$q(E,t) = 0 \qquad for \;\; t > t_{off} \tag{5.20}$$

One can thus define a minimum energy break E_b^{min}, representative of the oldest particles, and a maximum energy break E_b^{max} associated to the source power-off:

$$E_b^{min} = \frac{1}{\beta(t-t_0)} \qquad E_b^{max} = \frac{1}{\beta(t-t_{off})} \tag{5.21}$$

The solution of the continuity equation before E_b^{max} can be obtained following the simple CI model. Then, from time t_{CIOFF} on, the injection is stopped and the spectrum evolves as in a single injection model but starting from the aged CI power-law with spectral index p+1. The three trends of the solution are here reported:

$$N(E,t) = \frac{QE^{-(p+1)}}{\beta(p-1)}\left[\left(1-\frac{E}{E_b^{max}}\right)^{p-1} - \left(1-\frac{E}{E_b^{max}}\right)^{p-1}\right] \qquad if \quad E < E_b^{min} \tag{5.22}$$

$$N(E,t) = \frac{QE^{-(p+1)}}{\beta(p-1)}\left(1-\frac{E}{E_b^{max}}\right)^{p-1} \qquad if \quad E_b^{min} < E < E_b^{max} \tag{5.23}$$

$$N(E,t) = 0 \qquad E > E_b^{max} \tag{5.24}$$

The first term in parentheses of Eq. 5.22 can be rewritten as follows:

$$\left(1-\frac{E}{E_b^{max}}\right)^{p-1} = \left(1-\frac{E_b^{min}}{E_b^{max}}\cdot\frac{E}{E_b^{min}}\right)^{p-1} = \left(1-\frac{\Delta t_{off}}{\Delta t}\cdot\frac{E}{E_b^{min}}\right)^{p-1} \tag{5.25}$$

where in the last passage we used Eq. 5.21 and we named $t - t_0 = \Delta t$ and $t - t_{off} = \Delta t_{off}$. Here the term $\frac{\Delta t_{off}}{\Delta t}$ represents the fraction of time during which the source has been powered off with respect to its entire life $t = t_{CI} + t_{off}$. Note that, if Δt_{off} is negligible ($\ll 1$) Eq. 5.22 and Eq. 5.23 reproduce the solution found for the CI model as expected.

Similarly, in the power spectrum the relation between the two break frequencies can be written as follows (Murgia et al. 2011):

$$\nu_{b,high} = \nu_b \left(\frac{t}{t_{OFF}} \right)^2 \tag{5.26}$$

Considerations on the models

As already mentioned, because of the continuous replenishment of fresh particles, the CI model is best suited to describe an active radio source. To the contrary, the other models regard sources which ceased their activity in the past. The main differences between the KP and JP emission spectra concern the assumed micro-physics for the electron population. While in the KP model the pitch angle of individual electrons is supposed to be constant, the JP model considers the single particle to be subject to many scattering events which randomize its pitch angle. Just for this assumption, the JP model has always been considered to be much more reliable, from a physical point of view, than the KP model. Despite of this, many examples of sources well fitted by the KP model are present in literature (e.g. Carilli et al. 1991). The reason for that has deeply been explored by Tribble (1992, 1994). There, he suggests that the assumption of a constant and uniform magnetic field, in this kind of sources, could be too simplistic. A more appropriate supposition would be to describe the magnetic field with a Gaussian random field. In this way the angles would be isotropically distributed and the field strength would be drawn from a Maxwellian distribution. Applying this adjustment to the models, he shows that little modification is produced to the KP model while the JP model results much flatter at higher frequencies. It is argued that the smoothing out of the sharp spectral decline present in case of constant magnetic field is easy to explain. In fact, in an environment with different field strengths there will be different ν_{break} values that will superimpose in the combined spectrum, which will become flatter and much more similar to the KP trend (see Fig. 5.4). With this arguments one could explain the variety of spectra studied in litterature which do not reproduce at all the drop expected in the classical JP model without renouncing the more accepted idea of an isotropic pitch angle distribution.

5.1.2 Spectral ageing analysis

In this section the approach used to produce the spectra and to extract the spectral ages for the sources of our samples are presented.

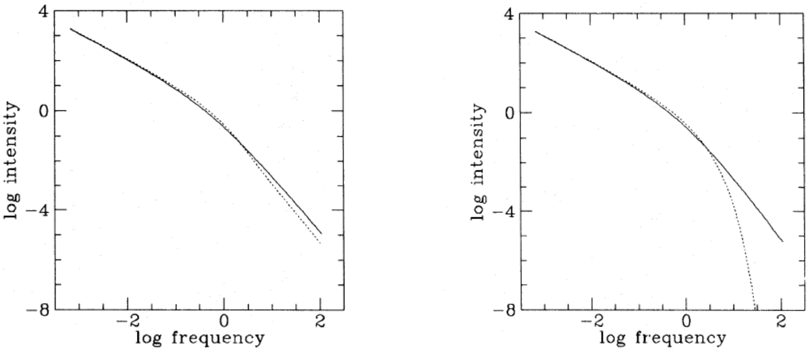

Figure 5.4: Aged spectra as a function of frequency for the KP model (left) and JP model (right). The aged spectrum assuming a random field strength is shown as a solid line, and that from a constant field shown as a dotted line for comparison (Tribble et al. 1993).

Spectral points selection

One of the main difficulties in creating radio spectra is that radio continuum observations are very monochromatic. The full band associated to one receiver can indeed vary from some tens of MHz to few GHz in the newest generation of instruments. This means that from one continuum radio observation one can get one single point of a flux density-versus-frequency diagram. A spectrum can thus be created by collecting measurements acquired by means of various telescopes in multiple epochs. This constitute inevitably a risk for the spectral points coherence. In fact, sources can be subjected to intrinsic flux density time variability and reveal different properties if observed with instruments with unsimilar capabilities.

The building blocks of all the 59 radio spectra presented in this work are constituted of our own data: for the most, by data from Bruni et al. (2012) described in Chapter 3, complemented by data reduced during this thesis. The high-frequency coverage of the radio spectra, up to 43 GHz, is essential to constrain as much as possible the break frequency region. In order to increase the flux density information of the sources and to create spectra as complete as possible, we also did a systematic research in the available radio survey catalogues for all objects.

The idea of astronomical surveys arises just from the need of collecting and cataloging information about as many sources as possible. The final goal would be to map the whole sky at various frequencies, permitting the creation of complete catalogues and allowing significant statistical analysis of celestial objects. Obviously we are now still very far from reaching this goal although a number of surveys has been performed in the last decades using various instruments at various frequencies. The characteristics of a survey are strictly connected to the telescope capabilities. On this basis every survey has, apart from its own field of view, its own resolution and sensitivity. For this reason, observing the same sky field with more than one instrument can be necessary to resolve and detect more sources with different properties. To begin with the research, the major radio surveys available in literature were consulted and are briefly described.

FIRST

The *Faint Images of the Radio Sky at Twenty-cm (FIRST) survey* was begun in 1993 with the goal of producing a 'radio version' of the Palomar Observatory Sky Survey over 10,000 square degrees of the North and South Galactic Caps. Observations have been carried out using the NRAO VLA in B configuration at 1.4 GHz. Maps typically reach now a 0.15 mJy rms and a resolution of 5 arcsec.To this day, the catalogue contains 811,117 sources, covering almost the same area of the Sloan Digital Sky Survey (SDSS). The survey area has been chosen to coincide with that of the SDSS; at the $m_v \sim 23$ limit of SDSS, $\sim 40\%$ of the FIRST sources have a radio counterpart in the SDSS.

NVSS

The *NRAO VLA Sky Survey (NVSS)* covers the whole sky with $\delta \geq 40^\circ$ (82% of the celestial sphere) and was mostly carried between September 1993 and October 1996 and completely accomplished in 1997 (Condon et al. 1998). They performed 1.4 GHz continuum total intensity and linear polarization observations using the compact D and DnC configurations of the VLA. These maps were made with a relatively large restoring beam (45 arcsec FWHM) to yield the high surface-brightness sensitivity needed for completeness and photometric accuracy. Their rms brightness fluctuations are about 0.45 mJy/beam = 0.14 K (Stokes I) and 0.29 mJy/beam = 0.09 K (Stokes Q and U). The rms uncertainties in right ascension and declination vary from 0.3 arcsec for strong ($S > 30$ mJy) point sources to 5 arcsec for the faintest (S = 2.5 mJy) detectable sources.

VLSS

The *Very Large Array (VLA) Low-frequency Sky Survey (VLSS*), released in Cohen et al. (2007), is a 74 MHz (4 m) continuum radio survey carried out in the period 2001-2007. Before the advent of the 74-MHz VLA receiver (Kassim et al. 1993) the severe ionospheric phase changes did not allow to obtain high resolution images at frequencies below 150 MHz. The survey was intended to serve as a low-frequency counterpart to the NVSS, allowing spectral information to be compiled for statistical samples of sources. It covered the entire sky north of $\delta > -30^\circ$ for a totality of 3π sr, collecting 68,311 sources. Using A, B and BnA configurations a resolution of approximately 80 arcsec is reached, together with a sensitivity of ~ 0.1 Jy/bm.

Some years later the publication of the first release of the catalogue, several major upgrades to the processing software along with the availability of faster computers gave the possibility to re-reduce data to refine and widen the results. The improved reduction techniques led to substantial improvements including images of six previously unpublished fields (1% of the survey area) and reducing the clean bias by 50%. The largest angular size imaged has been roughly doubled, and the number of cataloged sources is increased by 35% to 95,000. Revised data were then collected in a new catalogue and images archive which take the name of *VLSS Redux* (VLSSr, Lane et al. 2012).

WENSS

The *Westerbork Northern Sky Survey* (WENSS, Rengelink et al. 1997) is a low-frequency survey made with the Westerbork Synthesis Radio Telescope (WSRT) located in the northeastern Netherlands. It covers the whole sky with declination above 30° at 325 MHz (92 cm) reaching a limiting flux density of approximately 18 mJy (5σ). It contains 11,299 sources with angular resolution of 54 arcsec and a positional accuracy of 1.5 arcsec for the strongest objects. Observations were conducted in the period 1991-1996.

The Texas surveys

The *Texas survey* (Douglas et al. 1996) was carried out by the University of Texas Radio Astronomy Observatory (UTRAO) during the years 1974 - 1983. The observatory is a standard 'Mills Cross' type arrangement composed of five antennas arranged in a North-South and an East-West arms. It collected 365-MHz (80 cm) continuum observations of 66,841 discrete sources with declination ranging from $-35^\circ.5$ to $71^\circ.5$ intended to be complete to a flux level of 250 mJy. The resolution reached is approximately 60 arcsec.

The 87GB and GB surveys

The *87GB survey* (Gregory & Condon 1991) was realized by using the NRAO 91-m telescope in Green Bank, West Virgina. The entire sky with declination in the range $0^\circ < \delta < 75^\circ$ was mapped at 4.85 GHz (6 cm), covering a total sky area of 6 sr. The survey could not be extended south of the celestial equator beacause gravitational deformations severely degradated the performance of the instrument. Observations were performed during October 1987 and images of 54,579 discrete sources with angular size $\Phi < 10'$ and flux density $S > 25$ mJy with $\theta \sim 3$ resolution and $\sigma \sim 5$ mJy noise and confusion (Condon, Broderick, and Seielstad 1989) were collected. New observations in November 1996 contributed in creating the final set of sky maps using data from both epochs. The noise and position errors are nearly a factor of sqrt(2) smaller than in the epoch 1987 maps. The new catalogue is called *GB6 survey* (Gregory et al. 1996) and contains 75,162 discrete sources with angular sizes < 10.5 arcmin and flux densities above S $\sim$ 18 mJy.

By using these well-known radio surveys that have been extensively considered in the literature and that have proven to provide reliable flux densities, we fixed solid points for our spectra. A more meticulous research was then also carried by making use of the two most complete databases currently available: the NASA/IPAC Extragalactic Database (NED) and the Astrophysical Catalogs Support System (CATS) (Verkhodanov et al. 1997). While NED, like other databases, is reasonably complete for information on stars and galaxies, CATS aims at creating an exhaustive collection of radio measurements since they have exponentially increased in the last decades thanks to the advent of new instruments and surveys. In particular, it provides more than 350 different references and resulted to be very useful for our investigation.

Once the research was completed we proceeded in examining and selecting the collected flux densities. First of all, data from Very Long Baseline Interferometry (VLBI) were excluded because they typically miss a significant amount of the total flux density of a source, due to the high resolution. On the other hand, observations carried out with low resolution can suffer from confusion. When more flux densities at the same frequency were found, we compared them checking possible time variability. In case big discrepancies in values were found, we omitted points particularly out of trend because considered influenced by variability. It is worth remembering in fact that many surveys have been carried with a big temporal gap with respect to our observations which instead are gathered all in much shorter time range. Moreover, measurements from less famous catalogues should be treated with greater caution. Note that flux densities without respective errors were not considered for our selection.

In order to compare coherently all the flux densities available, a conversion to the Baars flux density scale was done. This has been possible making use of the scaling factors calculated by Helmboldt et al. (2008). In their work, they calculated multiplicative conversion factors between the Baars scale and all the major radio surveys available, by comparing flux densities of sources present both in Baars et al. (1977) and the survey of interest. The factors used for our analysis are shown in Tab. 5.1 .

Spectral fitting

We used the latest version of the SYNAGE software (Murgia priv comm) to perform spectral fitting. Flux densities of each source were collected together with their frequencies and errors. This will be the input file to be used then for the fitting. The program also offers the possibility to flag some of these points, i.e. to perform the fit taking in account only some of the flux densities listed in the input file. This option has revealed very useful when dealing with self-absorption evidences or multiple components.

The program allows the selection of various models to perform the fit. Among all of them, we only took in consideration the previously described ones i.e. CI, CIOFF, JP, KP as well as a simple power-law function. The pure power-law function obviously best fits

Survey	f_{Baars}	Frequency (MHz)	Reference
6C	0.904	151	Hales et al. 1988
7Cn	1.237	151	Riley et al. 1999a
MIYUN	1	232	Zhang et al 1997
WENSS	1	325	Rengelink et al. 1997
TXS	1.041	365	Douglas et al. 1996
4C_M2	1.019	408	Munro 1971b
B3	1.091	408	Ficarra et al. 1985
MRC	1	408	Large et al. 1991
NVSS	1	1400	Condon et al. 1998
Z2D	1	3900	Larionov et al. 1994
NAIC5	1	4775	Lawrence et al. 1983
PMN	1	4850	Wright et al. 1994 - 1996
GB6-87GB	1	4850	Gregory et al. 1996
9C	1	1400, 4800, 15000 22000, 31000, 43000	Bolton et al. 2004
PKS90	1.024	Several	A. E. Wright & R. Otrupcek 1990

Table 5.1: List of the factors used to obtain flux densities in the Baars scale

transparent spectra without evident break frequency. In this case the main input parameter is the the power index which simply represents the spectral index of the power spectrum α at a generical time and has nothing to do with α_{inj}. When using this fitting function we always left the parameters free. Concerning the other models, the main parameters of the fit are the injection spectral index α_{inj} and the normalization which can be both kept fixed at a certain value or left free. In particular, in our fits we left them always free as first choice. In this case the programme assumes an initial spectral index and at the same time, it considers a second slope in order to fit the high-frequency region of the spectrum, which depends on the model under consideration. In consecutive iterations, these slopes are progressively modified in order to minimize the χ^2 of the global fit. The χ^2 is here used as statistical test to determine the best fit model. Its expression is here reported:

$$\chi^2 = \sum_i \frac{(S_i - S)^2}{\sigma_i}$$

where S_i and σ_i are the measured flux densities at frequency ν_i with respective error while S is the theoretical flux density value. The goal of this test is to measure whether the observed data significantly differ from the theoretical ones. If $\chi^2 = 0$ the observed data completely coincide with the theoretical ones. The bigger the χ^2 is, the worse observed data are fitted with the model. When the couple of values (α_{inj}, ν_{br}) which minimize the

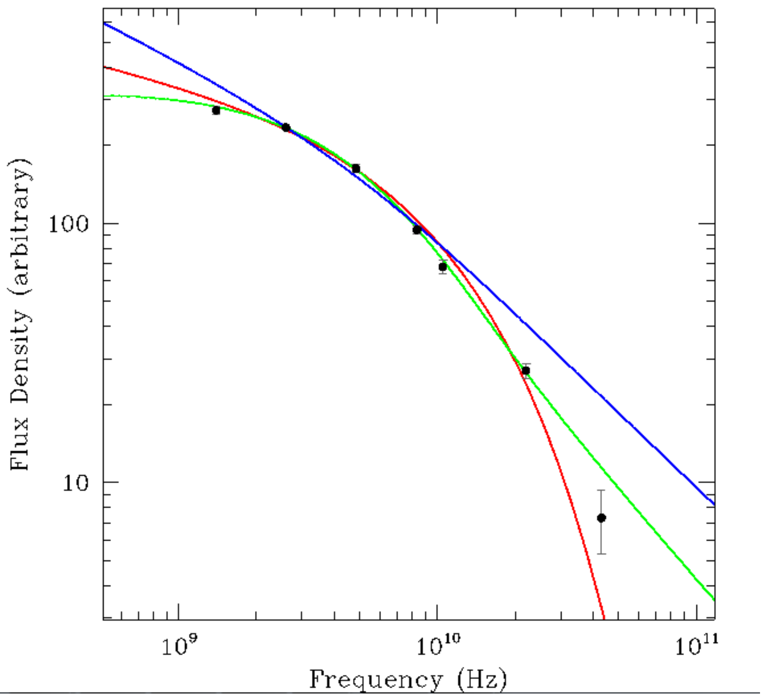

Figure 5.5: Comparison of spectral fits performed with different models for source 0154+00. The red line represents the JP model fit, the green line represents the KP model fit and the blue line represents the CI model fit.

χ^2 is thus found, the best fit with that particular model is found. ν_{br} is obtained as the frequency where the two asymptotic slopes intersect. In order to compare the goodness of different models, the χ^2_{red} is often used, which also takes into account the number of degrees of freedom of the fit (i.e. number of data - number of parameters) and assumes a value of 1 in case of total accordance with the data. Only in few occasions we decided to fix α_{inj} to a theoretical value of 0.5. This choice was made in case the spectral coverage was so poor that the fit could not converge with α_{inj} as free parameter.

One illustrative example of the way of proceeding with the best fit selection is here reported. In this case, it appears plain already by eye, that the best fit cannot come from the CI model. In fact, at high energies, the trend dramatically breaks off. In Fig. **??** each model is indicated with a different colour.

The best fit model should be found on the basis of a χ^2 comparison as previously explained. Despite that, we found various cases in which the difference in χ^2 between models was not so evident to make us accomplish a statistically reliable choice. In these cases we report values for all models.

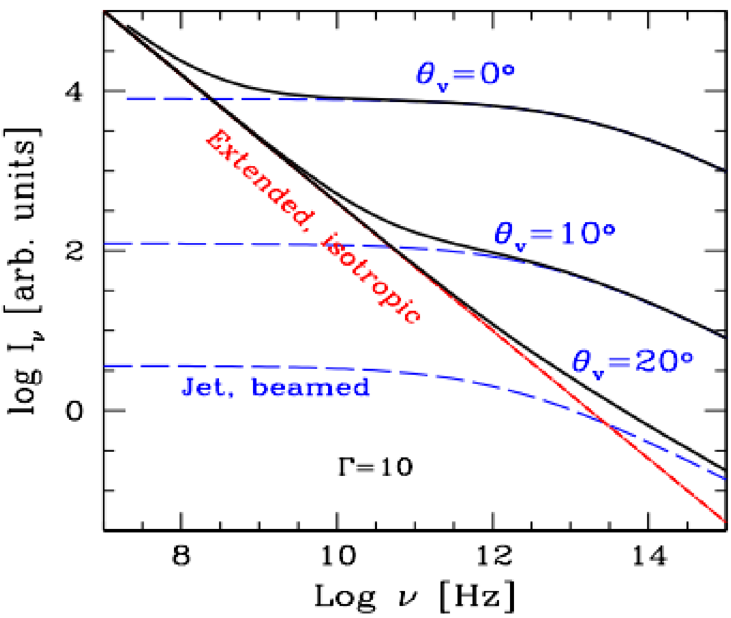

Figure 5.6: The emission of the jet is beamed, and depends on the viewing angle (blue lines). The emission from the radio lobe is instead isotropic, and is optically thin (red line). Since it is not beamed, it does not depend on the viewing angle. The overall appearance of the radio spectrum therefore depends on the viewing angle. Steep radio spectra correspond to large θ, flat radio spectra to small θ. (Ghisellini et al. 2012)

Spectral results

As already highlighted by Bruni et al. (2012) a great variety of radio spectral shapes were found. Despite that, three main typologies have been recognized which will be discussed here. For a correct interpretation one has always to remember that the sources in question are almost always unresolved at kpc scale. This means that we are looking at a superposition of emissions coming from different components within the beam. In particular, depending on the line of sight, the main contribution to the total emission is given by the dominant component, i.e. the lobes, the jet or the hot-spots.

Since the jet material is moving with a bulk Lorentz factor Γ, its radiation is beamed. What we see is therefore amplified if the jet points at us, and depressed if the jet points elsewhere. The large structures (hot spots and radio-haloes), instead, are not moving, and their emission is isotropic. The ratio between the jet emission and the radio-lobe emission is thus a strong function of the viewing angle as shown in Fig. 5.6. Some sources also present complex spectra which suggest the presence of different components. In these cases, the component at higher frequency was only fitted when possible.

At very low frequencies we expect that the emission is always dominated by the lobe, for all viewing angles. Lobe and jet emission are equal at some frequency which gets higher as the viewing angle with respect to the jet increases. For misaligned jets the depressing factor due to beaming is so large that we do not see the jet, we only see the lobe emission.

Flat spectrum sources

2 out of 25 BAL sources and 5 out of 34 non-BAL sources show flat spectra (see Fig. 5.7). This kind of trend is typically interpreted as due to the radio jet directly pointing along our line of sight (small viewing angles). Because of shocks created along the jet itself, beamed sources generally also suffer from severe variability. This is observed in our objects as well. Special care should be taken though when interpreting this kind of spectra. In fact, a flat trend can also be the result of a superposition of multiple compact components. This would then lead to a total misinterpretation of the source emission. For example, source 1335+02 shows an upper limit at 43 GHz which lies very far from the trend of all the other spectral points. Trusting in that upper limit, the source must experience a drastic drop in flux densities at high frequency which probably cannot be in accordance with the picture of beamed source. The same happens to source 1641+33 and 2346+00. These are obviously only speculations. More spectral points are needed at frequencies higher than 20 GHz to confirm the spectral trend and morphological observations at VLBI resolutions would definitely help in characterizing the sources. Plots of the spectral fits are presented in Fig. 5.7.

ID	Class	α
1335+02	BAL	0.14
1404+07	BAL	0.08
0029-09	nonBAL	-0.09
1411+43	nonBAL	0.23
1512+35	nonBAL	0.06
1641+33	nonBAL	0.01
2346+00	nonBAL	0.09

Table 5.2: Flat spectrum sources with fitted spectral indices

Power law spectrum sources

4 out of 25 BAL sources and 15 out of 34 non-BAL sources do not show signs of break frequency and result only well fitted with a pure power law function. Within this category different types of spectra are collected. In some cases (e.g. 1502+55) a continuous, well-constrained power-law trend from 74 MHz to high frequencies is present. Unfortunately, some sources show instead a big gap in spectral points between the lowest frequencies

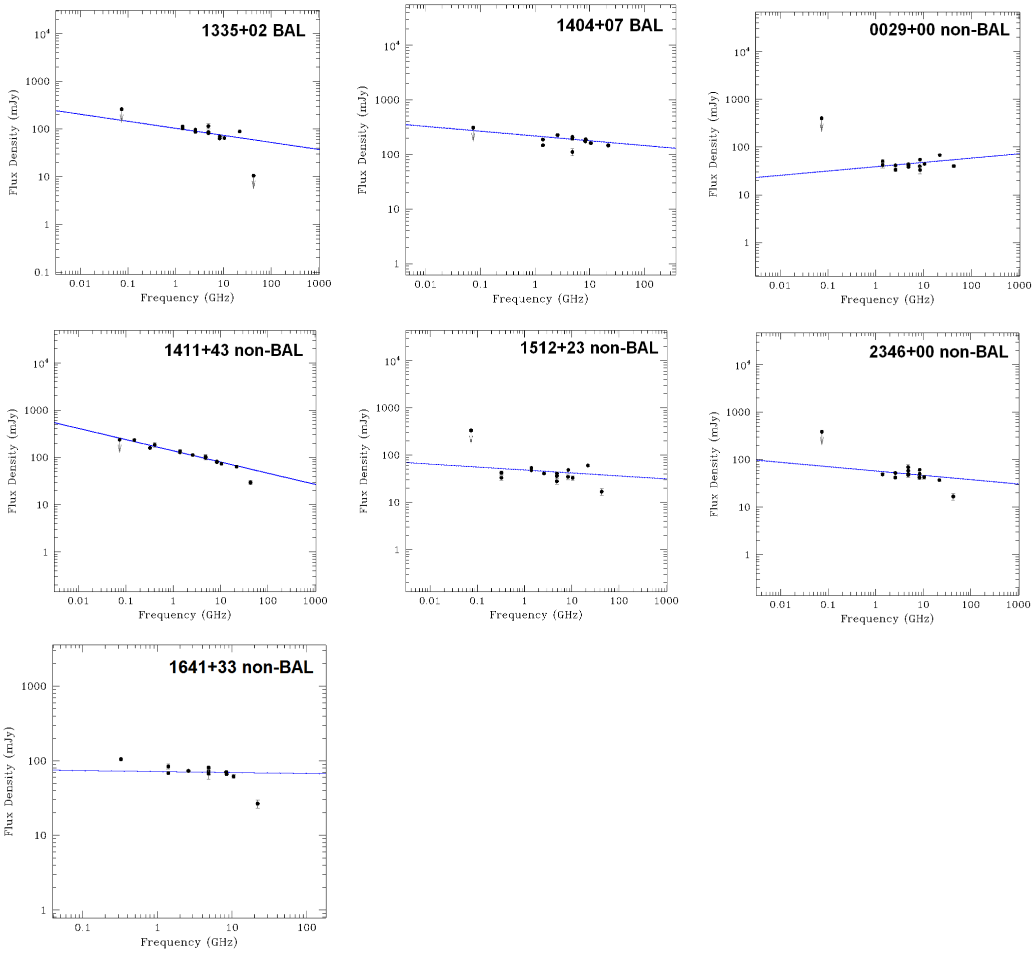

Figure 5.7: Power-law fits for sources which show a flat trend. Vertical arrows indicate upper limits.

and the highest ones (e.g. 0849+27). Here we cannot really know whether intermediate frequencies suffer from self-absorption. In other cases instead (e.g. 2143+00), evidence of self-absorption at low frequencies is observed. As already introduced in the previous section, here we made use of the flagging option, in order to fit the transparent region of the spectrum only. Lastly, some sources (e.g. 2129+00) miss the highest-frequency spectral points or their errors are so big that the fit is not able to recognize a break frequency even if present. In this circumstance, we chose the power law as the most reliable fit. Note that some of these sources (0849+27, 1103+11, 0033-00, 0125-00, 1728+56) are resolved at some frequencies at the arcsecond scale with the VLA and show multiple components. Despite that, because of insufficient spectral points for each component, we only study the total emission spectrum. Plots of the spectral fits are presented in Fig. 5.8.

ID	Class	α
0849+27	BAL	0.65
1103+11	BAL	0.71
1304+13	BAL	0.68
1327+03	BAL	0.60
0014+01	nonBAL	0.61
0033+00	nonBAL	0.80
0124+00	nonBAL	0.80
0125-00	nonBAL	0.64
0158-00	nonBAL	0.77
1322+50	nonBAL	0.69
1333+47	nonBAL	0.50
1502+55	nonBAL	0.86
1636+35	nonBAL	0.57
1728+56	nonBAL	0.90
2109-07	nonBAL	0.59
2129+00	nonBAL	0.37
2143+00	nonBAL	0.44
2248-09	nonBAL	0.80
2353-00	nonBAL	0.84

Table 5.3: Power-law spectrum sources with fitted spectral indices.

Sources with measured break frequency

For 11 out of 25 BAL sources and 5 out of 34 BAL sources SYNAGE succeded in fitting the spectrum thus finding a break frequency. The adopted strategy has already been described in Section 5.1.2. We here limit ourselves to show the spectral results. Plots of the spectral fitting are also shown in Fig. 5.9.

Peculiar sources

6 out of 25 BAL sources and 7 out of 34 non-BAL sources could not be allocated to any of the previous categories either because of complicated spectral shapes or because of missing spectral constraints. Here we briefly comment on these spectra:

- Sources 1040+05 and 1237+47 (BAL) do not have sufficient spectral points to make any fit or consideration on their spectral shape (see Fig. 5.10 and Fig. 5.11).). More observations are needed to proceed with the analysis.

ID	Class	CI			CIOFF			JP			KP			PL	
		α_{inj}	$\nu_b[GHz]$	χ^2_{red}	α_{inj}	ν_b [GHz]	χ^2_{red}	α_{inj}	ν_b [GHz]	χ^2_{red}	α_{inj}	ν_b [GHz]	χ^2_{red}	α_{inj}	χ^2_{red}
0044+00	BAL	0.5 fix	12.7	**2.62**	0.5 fix	12.6	3.00	0.5 fix	58.2	2.70	0.5 fix	32.6	2.68	0.70	2.32
0756+37	BAL	0.34	3.2	39.57	-	-	-	0.48	29.8	**11.11**	-	-	-	-	-
0816+48	BAL	0.42	4.1	3.6	0.33	10.5	1.44	0.34	13.1	**1.22**	0.33	6.94	1.50	0.70	6.62
0842+16	BAL	0.37	5.6	4.61	-	-	-	0.35	22.7	**4.09**	0.34	18.1	4.11	0.65	5.19
1014+05	BAL	0.36	11.8	2.06	0.37	26.9	2.41	0.37	48.7	**2.00**	0.37	27.3	**2.00**	0.47	2.5
1054+51	BAL	0.40	2.5	4.28	-	-	-	0.24	7.0	**2.91**	-	-	-	0.73	5.4
1102+11	BAL	0.5 fix	2.9	17.09	-	-	-	0.5 fix	15.0	**11.6**	-	-	-	0.85	23.7
1129+44	BAL	0.75	7.6	3.06	-	-	-	0.46	11.8	**0.67**	-	-	-	1.04	4.0
1159+06	BAL	0.61	8.4	3.32	0.58	24.7	3.04	0.58	30.5	**2.65**	0.58	17.8	2.74	0.82	4.5
1229+09	BAL	0.5 fix	0.1	7.41	0.5 fix	0.2	**0.79**	0.5 fix	5.5	2.4	0.5	2.7	1.9	1.21	0.9
1337-02	BAL	0.5 fix	0.4	47.18	0.5 fix	6.8	13.04	0.5 fix	7.7	**9.79**	0.5 fix	3.8	12.11	1.3	25.67
1406+34	BAL	0.35	22.1	98.88	-	-	-	0.36	124.6	**18.35**	-	-	-	0.66	206
1624+37	BAL	0.49	9.8	11.23	0.41	27.0	5.8	0.41	30.1	**4.67**	0.40	15.4	5.80	-	-
0152+01	nBAL	0.5 fix	0.8	17.11	-	-	-	0.5 fix	18.7	0.32				1.7	1.33
0154+00	nBAL	0.89	18.9	1.48	-	-	-	0.69	39.1	**0.26**	0.67	19.0	0.29	0.84	38.24
0750+36	nBAL	0.35	7.4	6.26	0.31	21.7	3.5	0.31	24.6	**3.22**	0.31	13.1	3.58	0.55	11.9
1005+48	nBAL	0.40	10.3	7.60	0.41	34.1	7.26	0.41	50.86	**6.63**	0.41	27.9	6.74	0.49	22.11
1401+52	nBAL	0.41	7.4	1.70	0.32	13.3	1.61	0.33	23.9	**1.27**	0.33	12.6	1.30	0.68	2.09
1528+53	nBAL	0.60	7.6	3.42	0.61	30.3	3.49	0.61	38.4	3.30	0.61	21.5	**3.29**	0.72	12.6
1554+30	nBAL	0.5 fix	7.6	4.86	0.5 fix	35.8	4.09	0.5 fix	40.2	**3.07**	0.5 fix	22.0	3.24	0.91	6.22
2244+00	nBAL	0.38	13.1	7.87	0.30	32.47	9.9	0.30	45.73	**6.57**	0.30	25.2	6.71	-	-

Table 5.4: Spectral fitting results for CI, CIOFF, JP, KP, PL models. For each model the fit output parameters are reported: the injection index α_{inj}, the break freqency $\nu_b[GHz]$ and the χ^2_{red}. When the α_{inj} value is combined with the label 'fix', the parameter has been fixed during the spectral fitting in order to obtain more reliable results. Empty spaces represent fits which did not converge.

- Source 0929+37 (BAL) presents a multi-component spectrum (see Fig. 5.12). The spectral coverage extends from 74 MHz to 43 GHz. Unfortunately flux density at the highest frequency is known with great uncertainty, so that no indication on the spectral steepening can be deduced. On the other hand, already at 5 GHz the trend displays signs of spectral index inversion suggesting a self-absorption contribution. At lower frequency, though, the spectrum does not result absorbed indicating the possible presence of a further component. Its contribution probably superimposes, at intermediate frequencies, on the high-frequency component. The 74-MHz upper limit indicates than the possibility of a further flattening or even self-absorption.

- Source 1411+34 (non-BAL) presents a multi-component spectrum with similar trend as BAL 0929+37 (see Fig. 5.13). The spectral coverage extends from 74 MHz to 43 GHz. At high frequencies the spectrum appears almost flat probably because of the superposition of more components. Then, as the frequency decreases we observe a spectral steepening possibly coming from a more extended transparent component. As a confirmation of these speculations one can look at the FIRST map at 1.4 GHz and at the ones by Bruni et al. (2012) at 4.8 and 8.4 GHz (Fig. 5.14). Actually the source appears resolved and shows a core and a double-lobe structure. At the light of this information one can think that the high frequency component in the total spectrum could come from the most compact or young component of the source.

- Source 0103-11 (non-BAL) cannot be interpreted in a univocal way. A thicker and wider spectral coverage would be needed to confirm whether we are looking at a superposition of compact components or at a single slope. The 43-GHz spectral point suggests that some steepening at high frequency is in action but it is not sufficient to constrain any change in slope (see Fig. 5.16).

- Source 2331+01 (non-BAL) probably suffers from some variability phenomenon (see Fig. 5.18). Indeed, all flux densities, from both single-dish and interferometry, collected during the year 2011 and reduced during this work appear to have smaller values than the ones previously measured. Note also the gap in flux density between the FIRST value and the NVSS one at 1.4 GHz, this last being smaller. Since these regular deviations are observed only in this source, with both telescopes and also in the most known surveys one is led to exclude some systematic calibration errors. A further confirmation of this idea also comes from Bruni et al. (2012) who classified it as 'source with significant variability'. In fact, they observed a flux density decrease of 3.7 mJy in a time period of 1.6 years at 8.4 GHz. The spectral points reduced in this thesis actually support this declining trend as can be seen in Fig. 5.18. More details on this analysis can be found in Section 5.3 of the variability analysis.

- Source 1603+30 (BAL) shows a spectrum with a concave parabolic shape with evident signature of self-absorption at low frequencies (see Fig. 5.17). From literature (Bruni et al. 2012) we know that the source is resolved at 22 GHz showing a core component (C) coincident with the optical position of the QSO and another component towards the south (A), which could be interpreted as a lobe. Unfortunately because of the lack of spectral points we could not succeed in performing a fit. Moreover, a big discrepancy in flux density is present at 4.8 GHz between the measurements by Bruni et al. (2012) and the GB6 catalogue which results much lower. This supports the idea of an intrisic variable source as proposed by Montenegro-Montes et al. 2008.

- Source 0905+02 (BAL) shows a very steep transparent spectrum in the frequency range between about 2.6 GHz and 22 GHz (see Fig. 5.15). For lower frequency though, the only spectral point available (1.4 GHz) is self-absorbed thus not allowing the break frequency fit. We tried here to fit the spectrum with a *Self-Absorption model* using a 2.5-index for the thick region. The fitted spectral index for the transparent region is equal to 1.33. Such a steep slope can be hardly interpreted as due to the injection of fresh particles which should then have an energy distribution with p=3.66. On the contrary it should probably be interpreted as the aged region of the spectrum with spectral index $\alpha_{inj}+1$. Because of the lack of points at low frequencies but also because of self-absorption we cannot constrain the α_{inj} and thus identify the break frequency.

- Source 1159+01 (BAL) exhibits a complex multi-component spectrum (see Fig. 5.20). Fortunately, we can learn from literature about its morphology. Montenegro-Montes et al. (2008b) could already resolve it at 4.8 and 8.4 GHz with the VLA in A configuration. Recently, Hayashi et al. (2013) conducted a VLBI campaign on four BAL QSOs included 1159+01. At a milliarcsecond resolution the source appears composed by a radio core aligned with several discrete components that extend ~ 90 mas towards the southeast and a significant counter feature ~ 50 mas northwest. From a morphological point of view thus they could classify it as a two-sided structure. Studying the spectral indices of the single components they also found the core to have an inverted spectrum and the other components to show very steep spectral indices. In Fig. 5.21 the total spectrum they constructed is also shown. They identify two spectral peaks: the first one peaking at few hundred MHz and the second one at ~ 10 GHz. The GHz-peaked component originates in the radio core, while the steep spectrum components originate from the extended structure with several discrete blobs. In our work we actually find confirmation of this description. Moreover, we propose another spectral point at 240 GHz from GMRT (Bruni, priv comm.) which confirms the global picture.

- Source 1521+43 (non-BAL) belongs to the category of the so-called 'inverted spectrum' sources. It actually shows a spectral slope of -0.3. Moreover it is one of the few sources exhibiting important variability. In Fig. 5.19 we have expressly collected all the measurements we found in literature about the source, just to show how many flux density oscillations have been reported.

Magnetic fields and Spectral ages

Magnetic fields are an essential component of many astrophysical environments. In the context of radio sources we have already seen that they play a fundamental role in producing the synchrotron emission observed. Moreover, they strongly interact with the ionized medium influencing its energetics and dynamics. However, their origin is not yet clear and in fact is one of the most challenging problems in modern astrophysics. A recent review that addresses the different proposed explanations to understand the origin of the galactic and extragalactic magnetic field was presented by Widrow (2002).

In our work, in order to calculate the spectral age of the sources, we are actually interested in estimating the magnetic field strength, as well as the break frequency. As already shown in Section 5.1.2 having a good spectral coverage, ν_{br} can be easily found by fitting the spectrum. To the contrary, the magnetic field determination is anything but easy. If the spectrum shows a self-absorbed peak, the magnetic field should be directly calculated by using Eq. 1.20. Special attention must be paid though when using this formula. In fact, the magnetic field has a strong dependence on the other parameters so that small uncertainties can strongly reflect in the magnetic field determination. Moreover, reaching a spectral coverage so that the spectral fitting could produce reliable values is a real challange.

To overcome these observational difficulties one usually looks for an estimate of the magnetic field strength on theoretical arguments. Indeed, by studying the radio-source energetic content, one can calculate the so-called *equipartition magnetic field*, which corresponds to the minimum energy condition in the radio-source (Pacholkczyk 1970).

The total energy of a synchrotron source is stored both in relativistic particles (U_{el} electrons and U_{pr} protons) and in magnetic fields (U_B):

$$U_{tot} = U_{el} + U_{pr} + U_B$$

The magnetic field energy contained in the source volume V is given by:

$$U_B = \frac{B^2}{8\pi}\Phi V$$

where Φ is the filling factor.

Assuming a power-law particle energy distribution with index p, the electron total energy in the range $\varepsilon_1 - \varepsilon_2$ is:

$$U_{el} = V \times \int_{\varepsilon_1}^{\varepsilon_2} N(\varepsilon)\varepsilon d\varepsilon = VN_0 \int_{\varepsilon_1}^{\varepsilon_2} \varepsilon^{-p+1} d\varepsilon$$

and can also be expressed as function of the synchrotron luminosity L_{syn}:

$$L_{syn} = V \int_{\varepsilon_1}^{\varepsilon_2} \left(-\frac{d\varepsilon}{dt}\right) N(\varepsilon) d\varepsilon = c_2 (Bsin\theta)^2 VN_0 \int_{\varepsilon_1}^{\varepsilon_2} \varepsilon^{-p+2} d\varepsilon \qquad (5.27)$$

By eliminating VN_0 and by writing ε in terms of ν one obtains:

$$U_{el} = c_2^{-1} c_1^{1/2} \overline{C}(\alpha, \nu_1, \nu_2) L_{syn} B^{-3/2} = c_{12}(\alpha, \nu_1, \nu_2) L_{syn} B^{-3/2}$$

where $sin\theta$ has been taken equal to 1 and

$$\overline{C}(\alpha, \nu_1, \nu_2) = \left(\frac{2\alpha - 2}{2\alpha - 1}\right) \frac{\nu_1^{(1-2\alpha)/2} - \nu_2^{(1-2\alpha)/2}}{\nu_1^{(1-\alpha)} - \nu_2^{(1-\alpha)}}$$

Remembering that, because of the Larmor formula, heavy particles do not emit much of their energy, one can assume the proton energy U_{pr} to be proportional to the electron energy U_{el} :

$$U_{pr} = kU_{el}$$

One can thus write the total energy as follows:

$$U_{tot} = (1+k)U_{el} + U_B = (1+k)c_{12} L_{syn} B^{-3/2} + \frac{B^2}{8\pi}\Phi V$$

A convenient estimate for the total energy is represented by its minimum value thus one has to derive the above expression. The condition of minimum energy is obtained when the contributions of the magnetic field and the relativistic particles are approximately equal:

$$U_B = \frac{3}{4}(1+k)U_{el}$$

The magnetic field for which the total energy content is minimum is (see Fig. **??**):

$$B_{eq} = (6\pi(1+k)c_{12} L_{syn} \Phi^{-1} V^{-1})^{2/7}$$

The total minimum energy is:

$$U_{tot}(min) = c_{13} \frac{3}{4\pi}^{3/7} (1+k)^{4/7} \Phi^{3/7} V^{3/7} L_{syn}^{4/7}$$

and the total minimum energy density is:

$$u_{min} = \frac{U_{tot}(min)}{V\Phi} = c_{13}\frac{3}{4\pi}^{3/7}(1+k)^{4/7}\Phi^{4/7}V^{4/7}L_{syn}^{4/7}$$

where $c_{13} = 0.921c_{12}^{4/7}$.

The total minimum energy density assuming $\Phi = 1$ and applying the K-correction, can be expressed in terms of observable parameters (Govoni & Ferreti 2008), as:

$$u_{min}\left[\frac{erg}{cm^3}\right] = \xi(\alpha,\nu_1,\nu_2)(1+k)^{4/7}(\nu_{0[MHz]})^{4\alpha/7}(1+z)^{(12+4\alpha)/7}(I_0\left[\frac{mJy}{arcsec^2}\right])^{4/7}(d[kpc])^{-4/7}$$

$$B_{eq} = \left(\frac{24\pi}{7}u_{min}\right)^{1/2}$$

where z is the redshift, I_0 is the source flux density at frequency ν_0, d is the source depth and the constant $\xi(\alpha,\nu_1,\nu_2)$ is tabulated in Table 1 of Govoni & Feretti (2004) for the frequency ranges 10 MHz - 10 GHz and 10 MHz - 100 GHz. For our calculations we assumed k=1 and we adopted a spectral index α equals to 0.5 for whom Govoni & Feretti (2004) pointed out a value for $\xi(\alpha,\nu_1,\nu_2)$ equals to 2.13 $\times 10^{-12}$.

In order to calculate the projected area of the source one needs to make some assumptions on the source geometry. Typically one assumes the source to be an ellipsoid symmetric to the major axis observed so that $area = \pi(ab)/2$. For each source the size was extracted from the maps at the highest resolution available. The depth of the source d is assumed to be equal to the minor axis of the ellipse observed. The cosmology adopted throughout the work assumes a flat universe and the following parameters: $H_0 = 70\ km\ s^{-1}\ Mpc^{-1}$, $\Omega_\Lambda = 0.7$, $\Omega_M = 0.3$. To extract the source dimensions from the available maps we used the task JMFIT which performs a Gaussian fit of the source. In case the fit could not deconvolve a size for the source (or component) we used the beam size as an upper limit for its dimension thus obtaining a lower limit for the magnetic field strength. In Tab. **??** and **??** the parameters used to compute B_{eq} together with the results of the calculations are presented for all sources. For 9 of our sources Bruni et al. (2013) carried out a VLBI observational campaign and already estimated the magnetic field for each of the observed component. For these sources we do not calculate magnetic fields and we use their values in the spectral age computation which follows. In Tab. **??** magnetic fields by Bruni et al. (2013) are reported.

The main uncertainties on this estimate are linked to the poor knowledge of the source dimensions (remember that also in the best cases we only measure the projected area of the source and we are obliged to assume an arbitrary depth) and on the assumptions made on parameters like k -which depends on the acceleration mechanisms and Φ. Various studies based on lobe dynamics and kinematics conclude anyway that the equipartition magnetic

ID	Comp	B_{eq} [mG]
0044+00	A	3.4
	B	2.0
	C	3.4
0756+37	A	9.1
	B	5.3
0816+48		10.6
0849+27	A	>2.0
	B	3.9
1014+05	A	>1.0
	B	1.4
	C	2.3
1102+11	A	>3.3
	B	2.4
1304+13	A	4.6
	B	6.6
1327+03		>2.6
1603+30	A	2.0
	B	1.9
	C	1.8

Table 5.5: Magnetic fields calculated by Bruni et al. (2013). Column 2 indicates the source component following the classification by Bruni et al. (2013).

field can be considered, in first approximation, a good estimate (Longair et al. 1995, Di Cuia 1994). Indeed they suggest the real value to be comprised between:

$$\frac{1}{3} \cdot B_{eq} \leq B \leq 2 \cdot B_{eq}$$

ID	Comp	z	freq [MHz]	S [mJy]	Min.axis [arcsec]	Maj.axis [arcsec]	Min.axis [kpc]	Maj.axis [kpc]	B [μG]	B_{CMB} [μG]
0842+06		2.45	22000	6.9	1.13*	0.81*	8.84*	6.34*	>97	38.68
0905+02		1.82	22000	8.8	1.03*	0.84*	8.69*	7.08*	>84	25.84
0929+37		1.91	43000	6.9	0.42	0.26	3.58	2.21	223.2	27.52
1040+05		2.44	8460	5.2	3.47*	2.38*	28.14*	19.30*	>29	38.45
1054+51		2.34	8460	9.5	2.89*	2.20*	23.63*	17.99*	>38	36.25
1103+11	A	1.73	8460	10.2	1.39	0.99	11.75	8.45	121.0	24.22
	C	1.73	8460	64.8	1.05	0.38	8.91	3.26	46.0	24.22
1129+44		2.21	22000	3.1	1.06*	0.84*	8.75*	6.93*	>71	33.48
1159+01		2.00	22000	169.2	1.09*	0.82*	9.12*	6.86*	>209.0	29.25
1159+06		2.19	22000	4.6	1.90*	0.99*	15.71*	8.18*	>60	33.07
1229+09		2.65	4860	17.3	3.20	0.54	25.54	4.33	100.6	43.29
1335+02		1.85	22000	88.6	0.29	0.08	2.47	0.67	906.6	26.39
1404+07		2.86	22000	146.9	0.13	0.09	1.06	0.77	1598.7	48.42
1624+37		3.38	22000	7.4	1.31*	0.91*	9.70*	6.74*	>115	62.34

Table 5.6: Parameters used for the magnetic field calculation for the BAL QSOs sample. In column 1 and 2 the sources and components are specified. Column 3 contains the redshifts. Column 4 and 5 present the highest frequency available to measure the source size and the relative flux density obtained. Columns 6-7 and 8-9 contain the major and minor axis of the source projected area in arcseconds and kpc respectively. Asteriks indicate the sources for which we could not obtain a deconvolved size so the beam size is used as an upper limit of the dimension. Columns 10 and 11 report the intrisinc magnetic fields and equivalent magnetic fields of the CMB calculated during this work respectively.

Figure 5.8: Power-law fit for sources which do not show a break frequency. Filled circles represent the spectral points used for the fit while empty circles represent the flagged spectral points. Vertical arrows indicate upper limits.

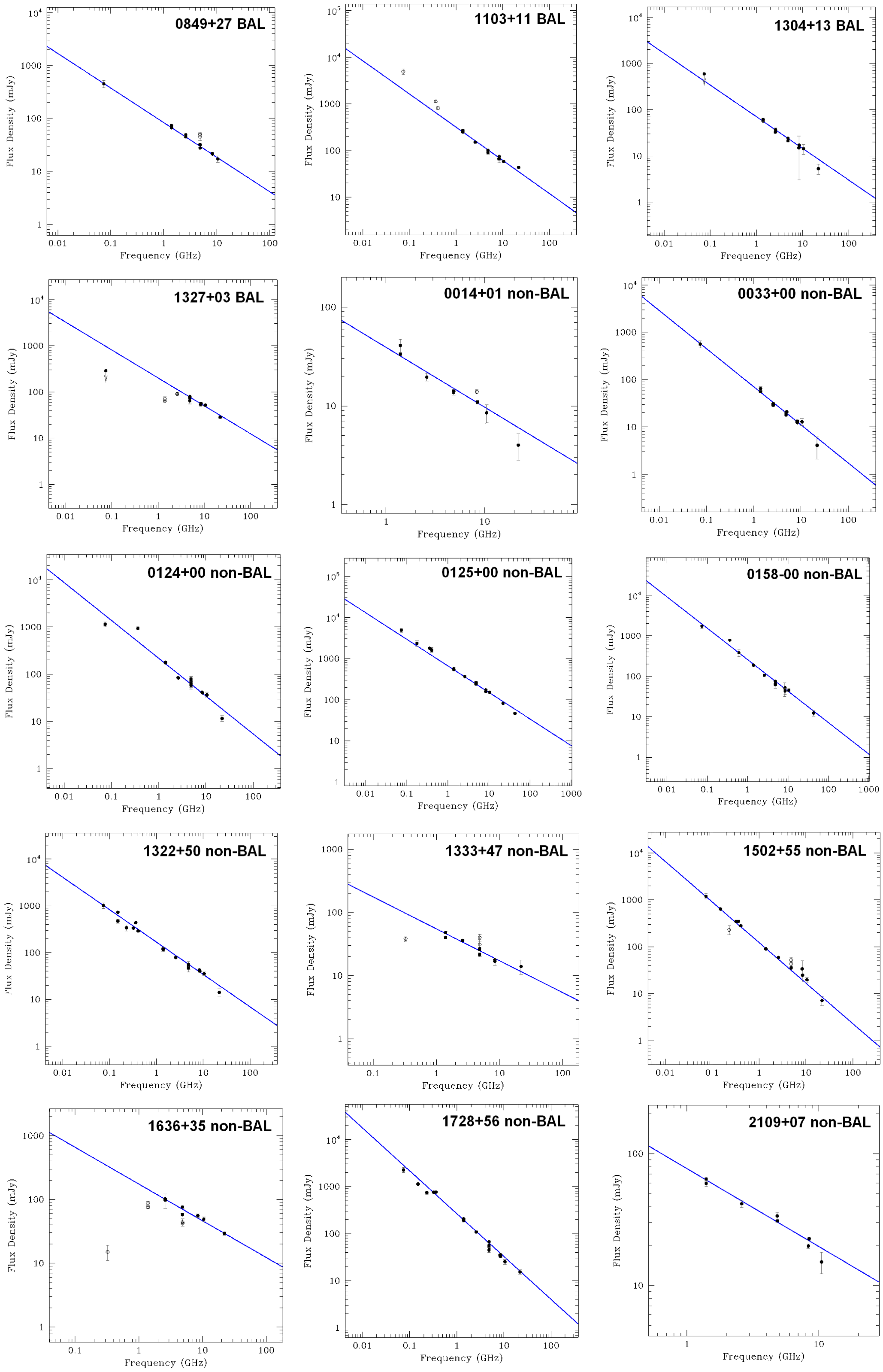

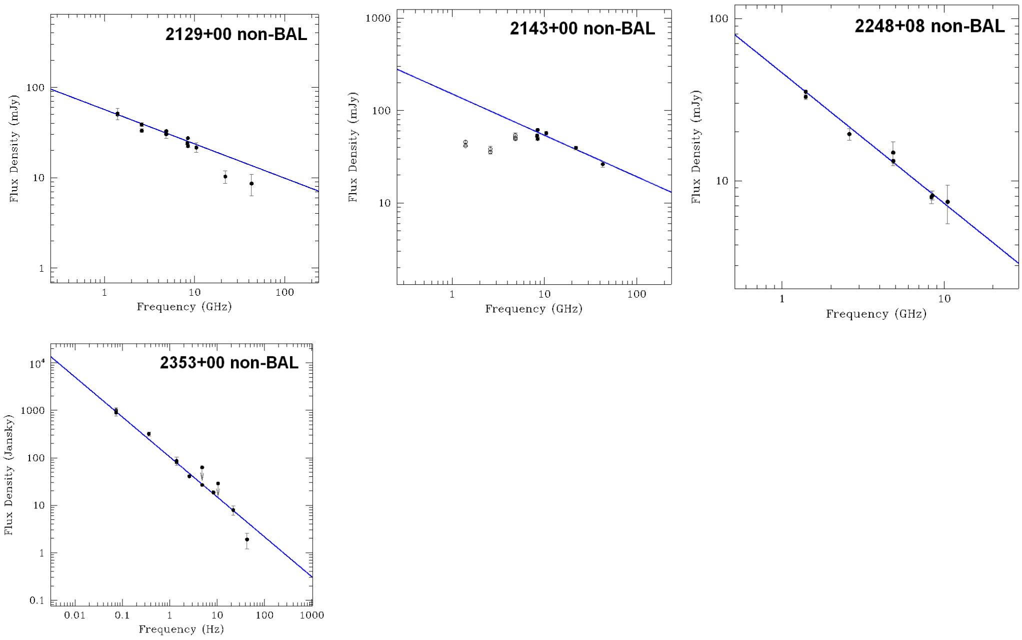

Fig. 5.8 Continued

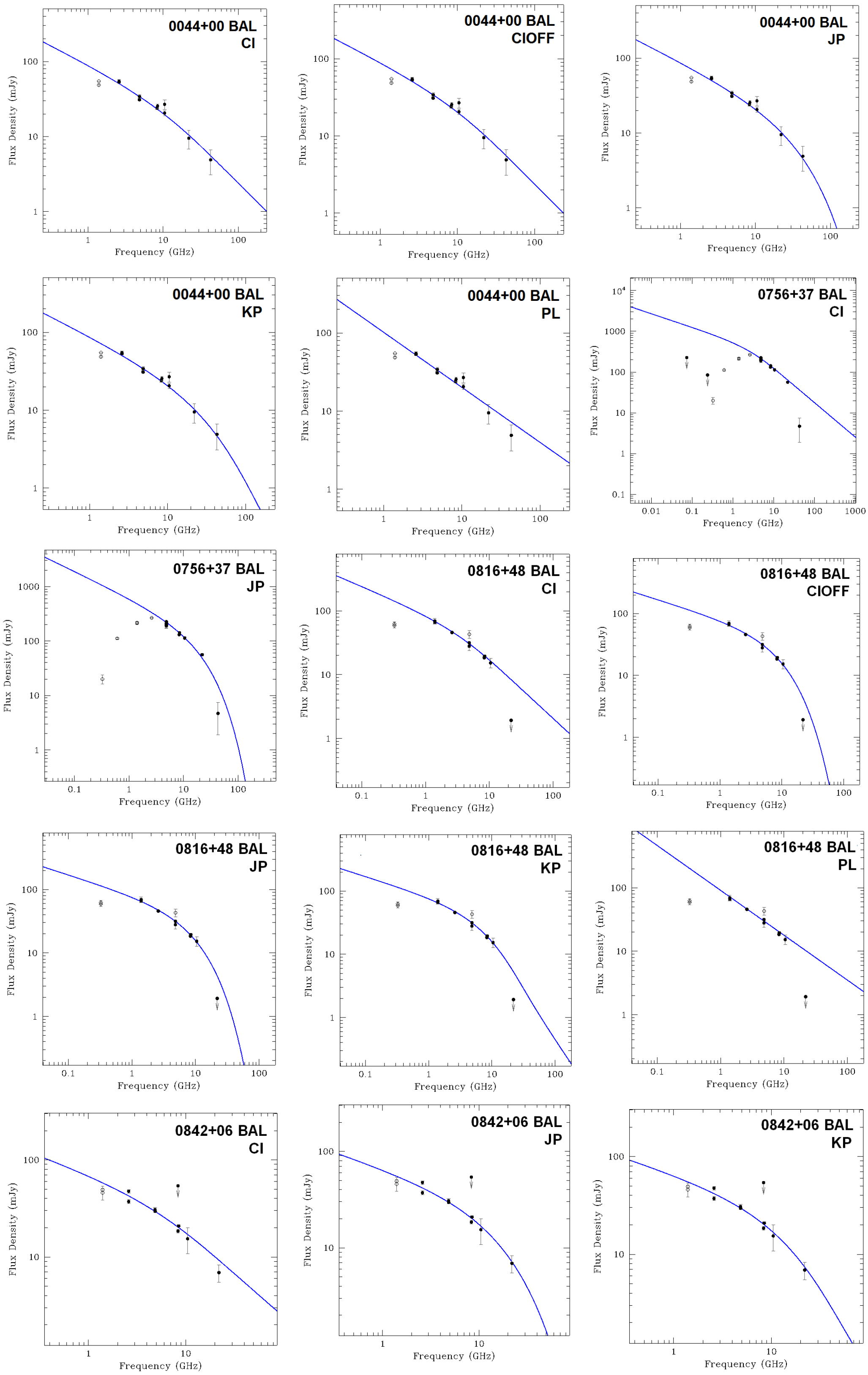

Figure 5.9: Fits of the radio spectra with various models (CI - CIOFF - JP - KP - PL). Filled circles represent the spectral points used for the fit while empty circles represent the flagged spectral points. Vertical arrows indicate upper limits.

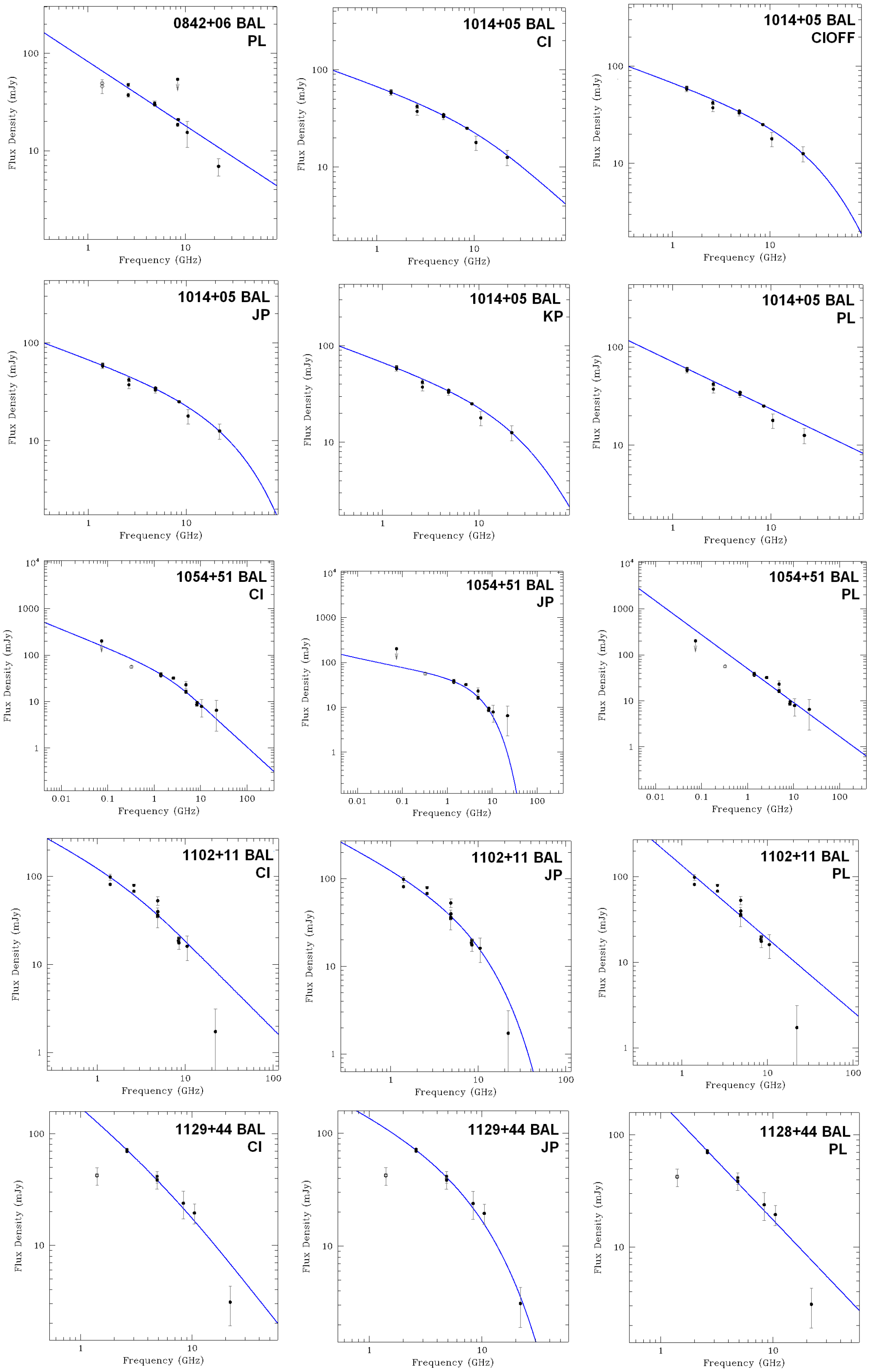

Fig. 5.9 Continued

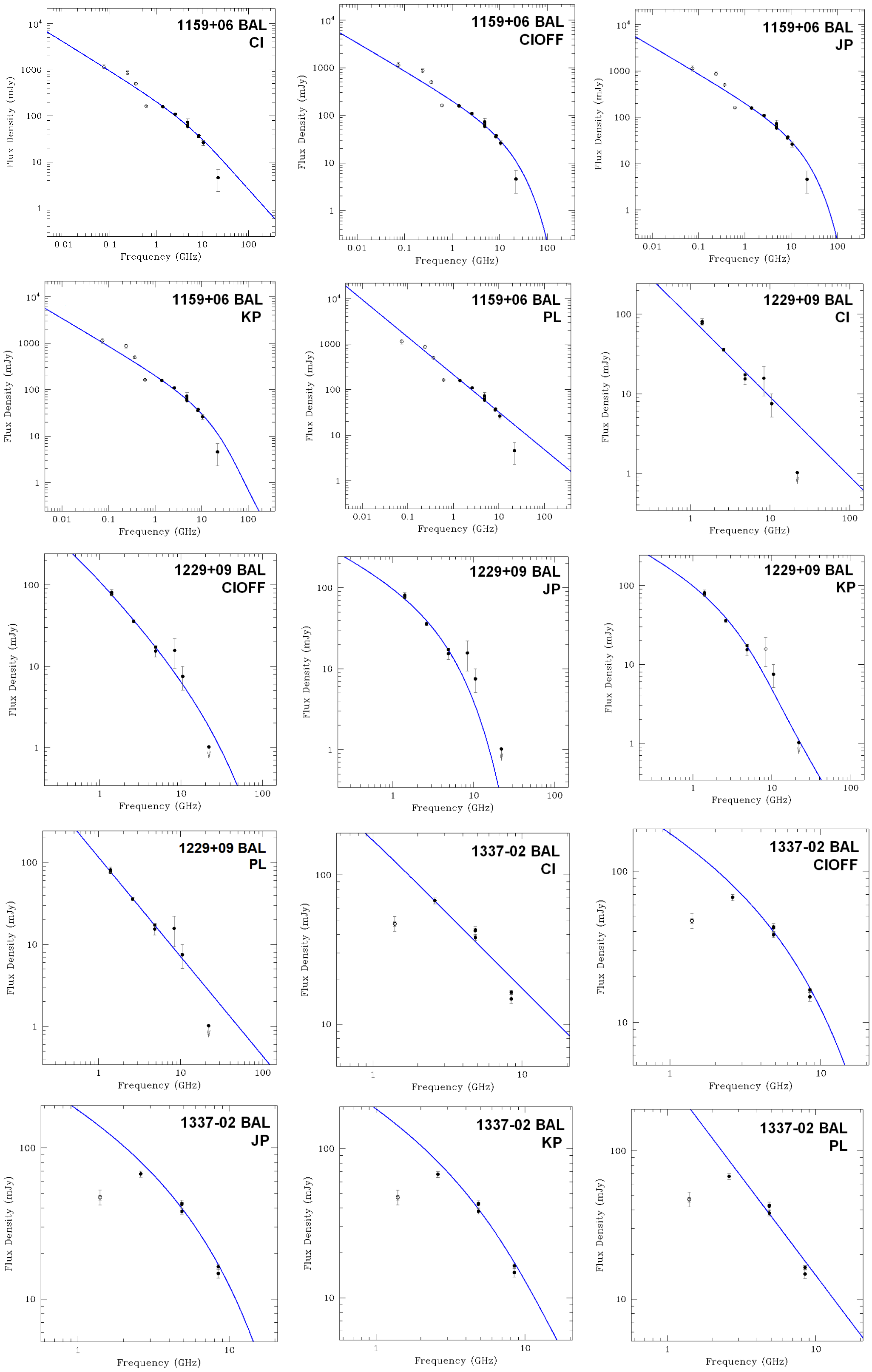

Fig. 5.9 Continued

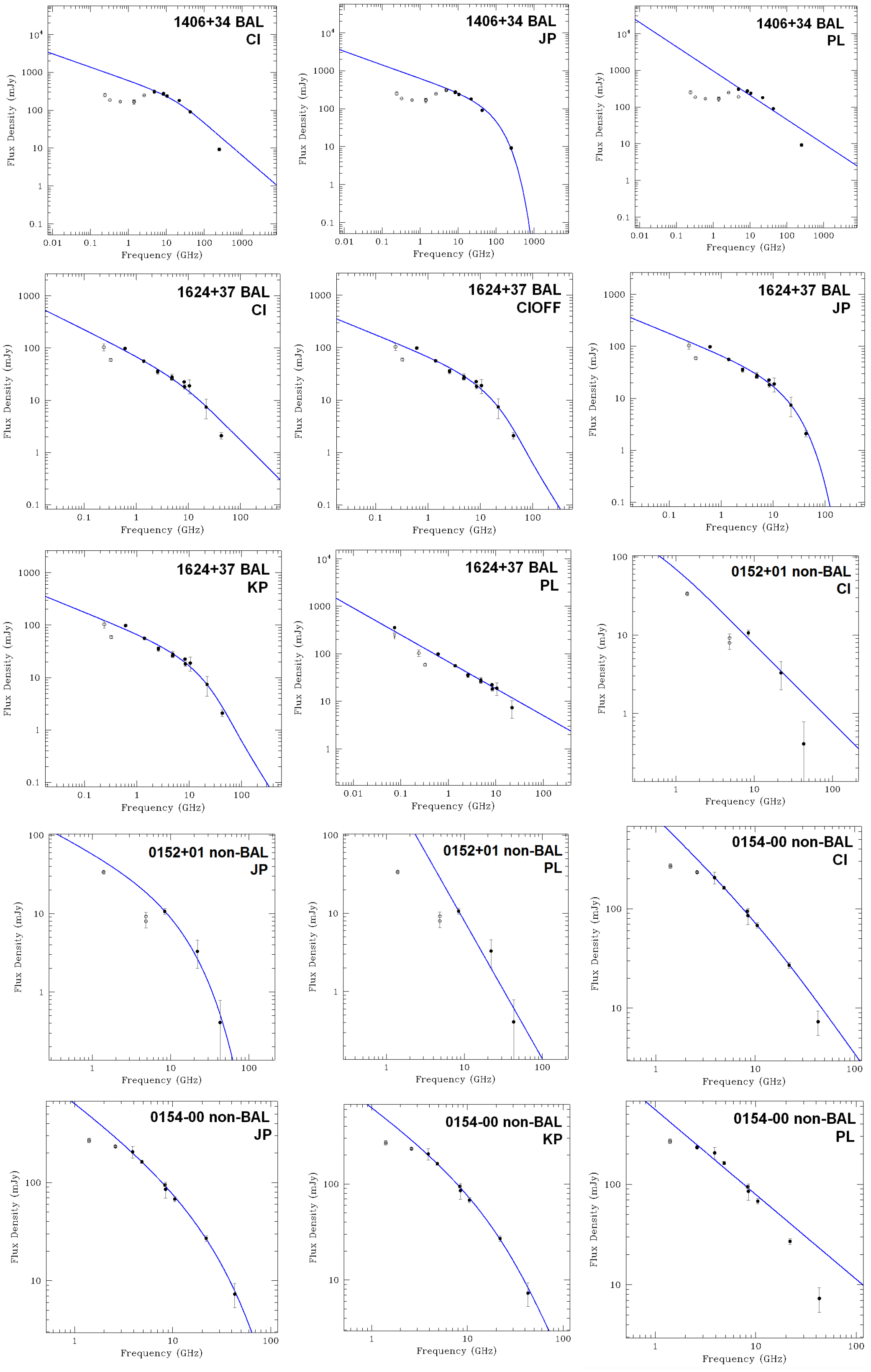

Fig. 5.9 Continued

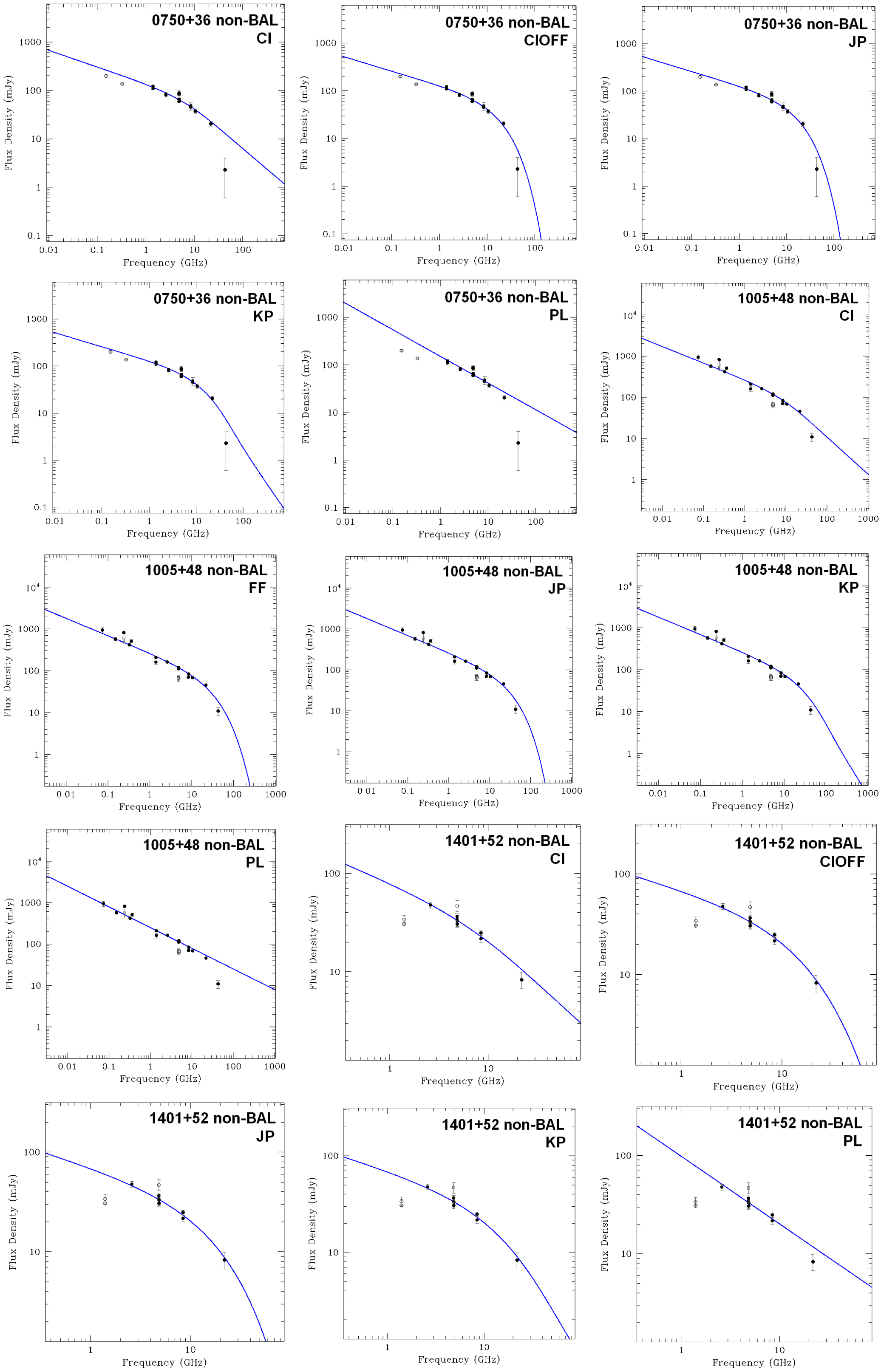

Fig. 5.9 Continued

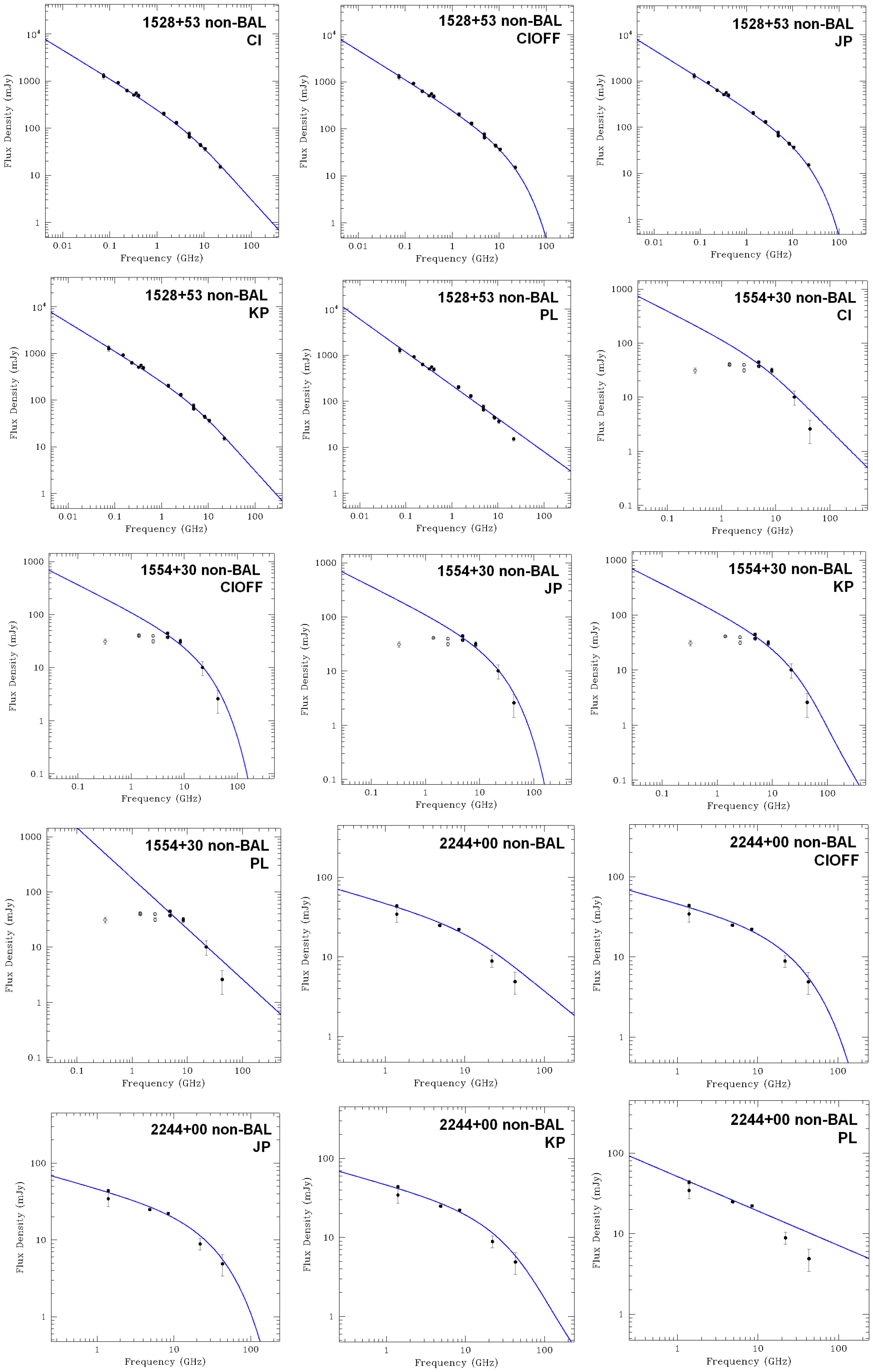

Fig. 5.9 Continued

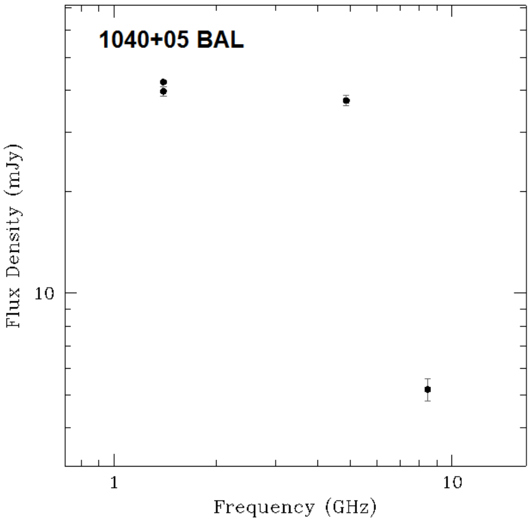

Figure 5.10: Radio spectrum of 1040+05

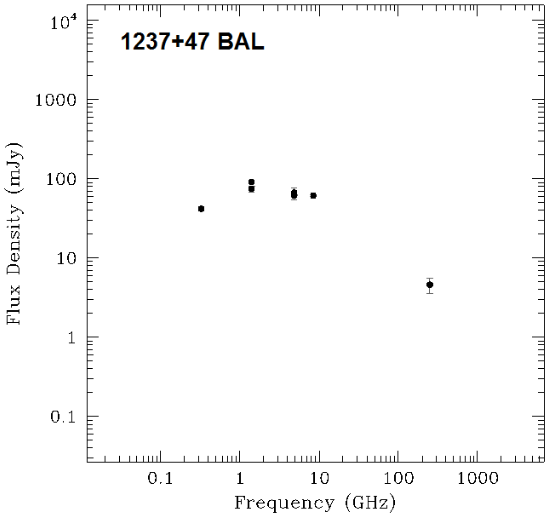

Figure 5.11: Radio spectrum of 1237+47

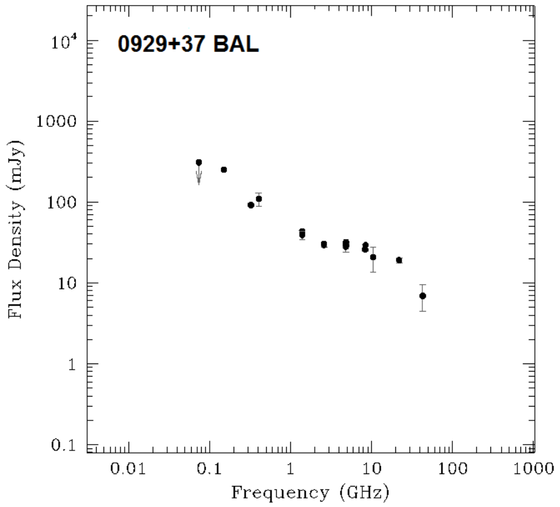

Figure 5.12: Radio spectrum of 0929+37

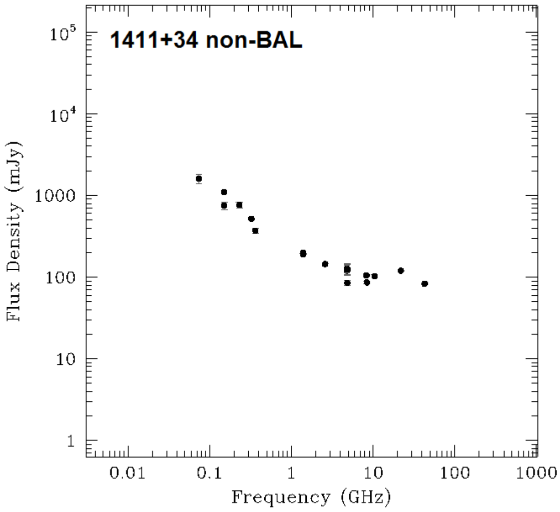

Figure 5.13: Radio spectrum of 1411+34

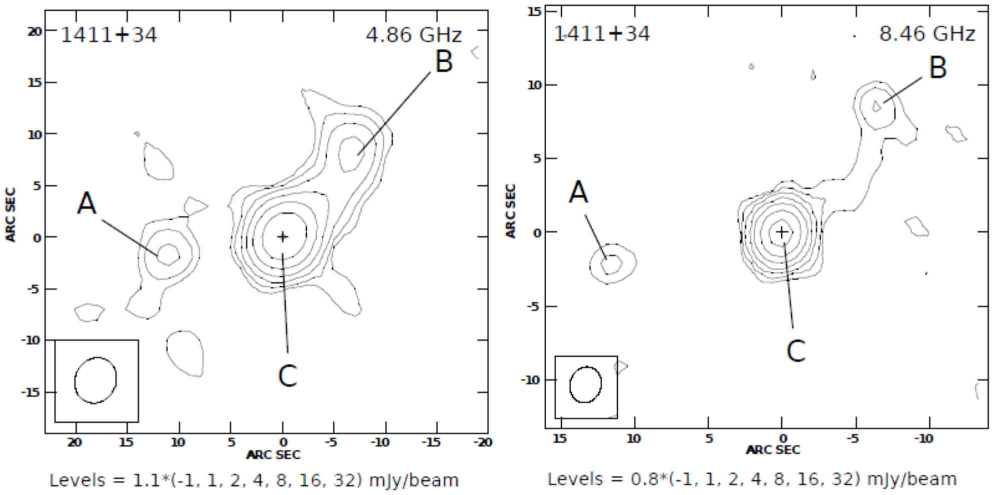

Figure 5.14: VLA-maps at 4.6 and 8.4 GHz for source 1411+34 (Bruni et al. 2012)

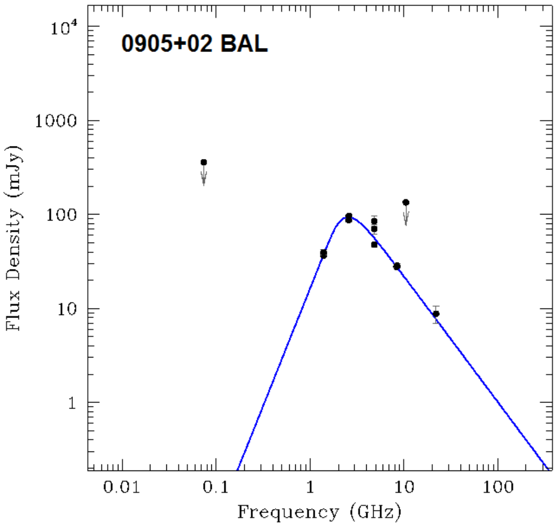

Figure 5.15: Radio spectrum of 0905+01

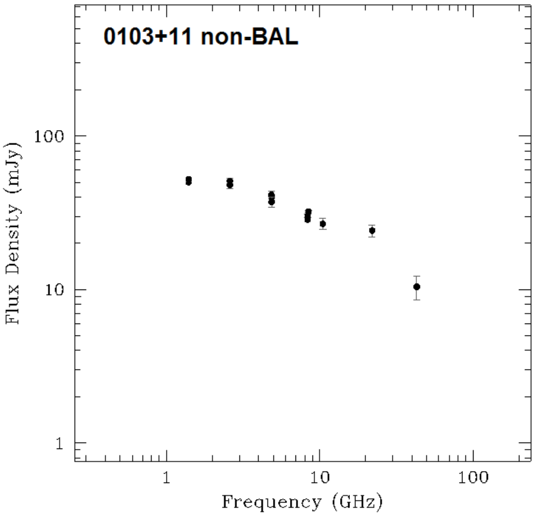

Figure 5.16: Radio Spectrum of 0103+11.

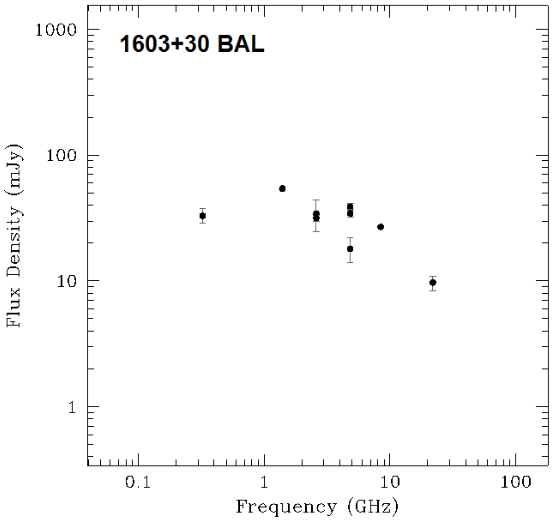

Figure 5.17: Radio spectrum of 1603+30

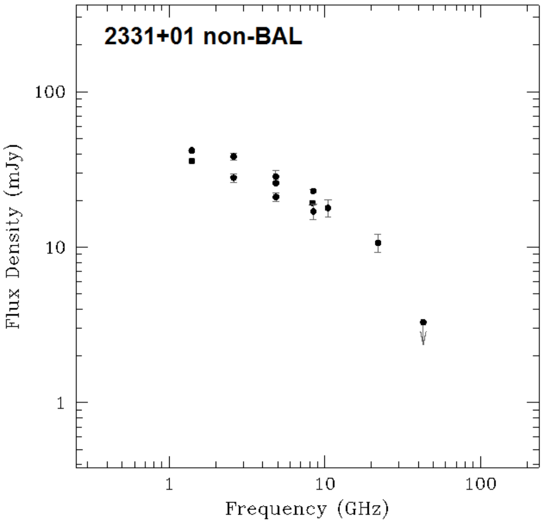

Figure 5.18: Radio spectrum of 2331+01

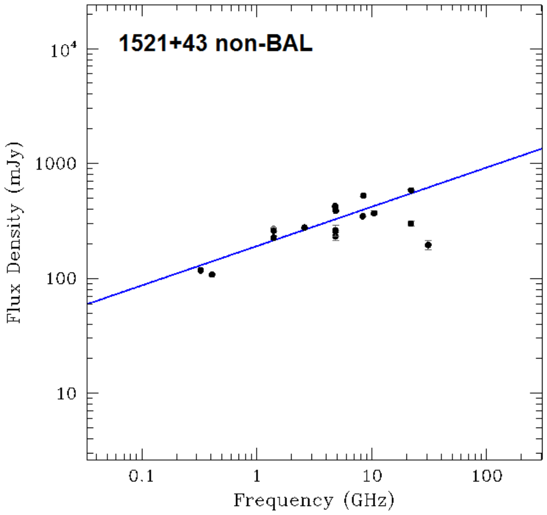

Figure 5.19: Radio spectrum of 1521+43

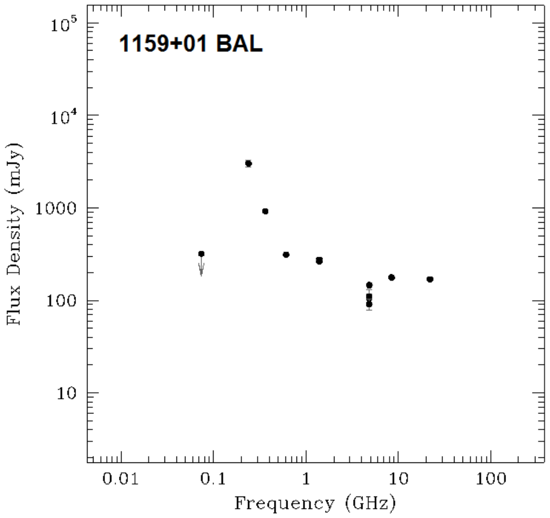

Figure 5.20: Radio spectrum of 1159+01

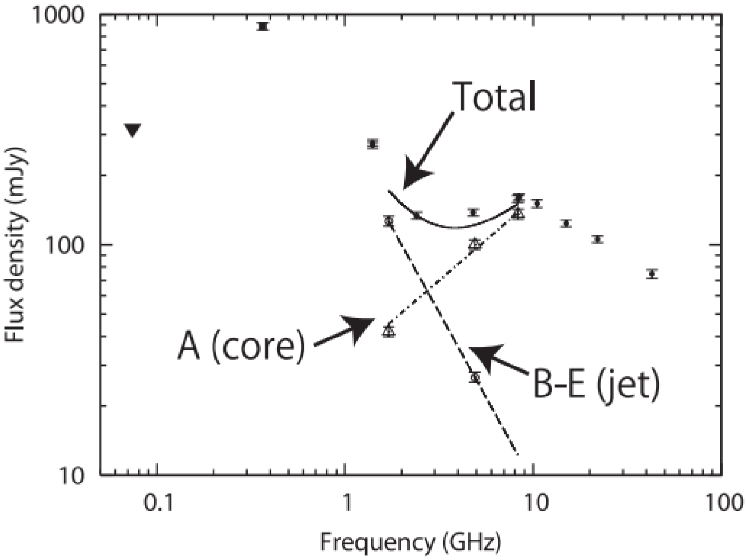

Figure 5.21: Radio spectrum of 1159+0112 by Hayashi et al. (2013 submitted). Observations using VLA (filled circle), Texas survey (filled square) plus their observation using VLBA are shown. Flux density obtained by their observation is decomposed into that of the radio core (open triangle) and jets (open circle). Power law fit to the core flux density (dot-dashed), jet fluux density (dashed), and sum of them (thick) are also illustrated.

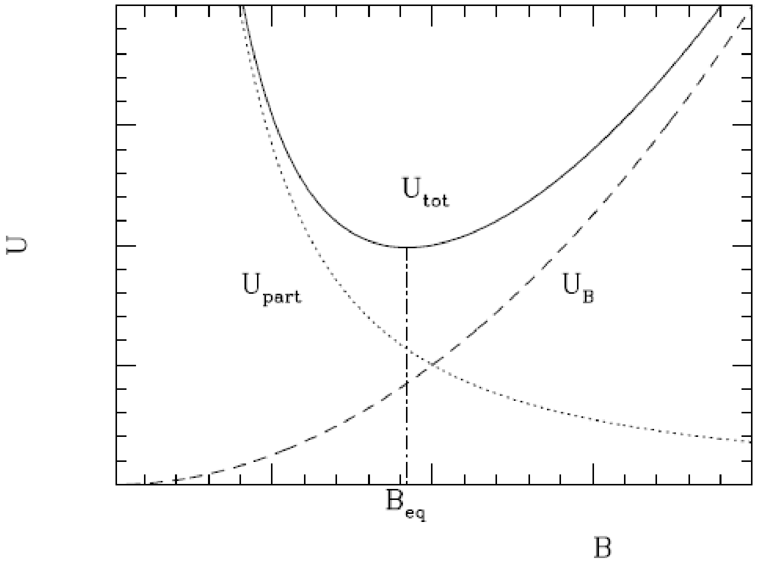

Figure 5.22: Energy content in a radio source (in arbitrary units): the energy in magnetic fields is $U_B \propto B^2$, the energy in relativistic particles is $U_{part} = U_{el} + U_{pr} \propto B^{3/2}$. The total energy content U_{tot} is minimum when the contributions of magnetic fields and relativistic particles are approximately equal (equipartition condition). The corresponding magnetic field is commonly referred to as equipartition value B_{eq}.

ID	Comp	z	freq [MHz]	S [mJy]	Min.axis [arcsec]	Maj.axis [arcsec]	Min.axis [kpc]	Maj.axis [kpc]	B [μG]	B_{CMB} [μG]
0014+01		2.18	22000	4.0	1.18	0.39	9.81	3.28	115.5	62.34
0029-09		2.71	43000	40.0	0.66*	0.41*	5.22*	3.24*	>327	44.73
0033-00	A	1.79	8460	2.5	2.43	1.97	20.54	16.68	24.3	25.29
	C	1.79	8460	10.7	1.79	0.89	15.14	7.55	298.1	34.96
0103-11		2.19	43000	10.4	0.71*	0.40*	5.87*	3.30*	>187	33.07
0124+00		1.85	22000	11.6	1.30	0.31	10.95	2.66	151.1	26.39
0125-00	A	2.28	8460	27.2	5.06	0.68	41.63	5.58	85.3	34.96
	C	2.28	8460	16.5	1.47	0.32	12.07	2.69	298.1	34.96
0152+01		3.17	22000	3.3	1.30	0.72	9.88	5.48	98.9	56.51
0154-00		1.83	43000	7.3	0.69*	0.42*	5.82*	3.54*	>146	26.02
0158-00		2.62	43000	12.4	0.29	0.20	2.38	1.59	432.5	42.58
0750+36		2.03	22000	20.5	0.93*	0.83*	7.77*	6.93*	>119	29.83
1005+48		2.38	43000	10.9	0.65	0.39	5.31	3.24	208.8	37.12
1322+50		1.73	22000	14.3	1.13*	0.81*	9.55*	6.85*	>93	24.22
1333+47		2.62	22000	13.9	0.98*	0.82*	7.82*	6.54*	129.9	42.58
1401+52		2.97	22000	8.3	1.13*	0.79*	8.72*	6.10*	120.9	51.22
1411+34	A	1.82	8460	2.6	2.87	1.41	24.22	11.91	97.9	25.84
	B	1.82	8460	5.3	2.87	1.41	24.22	11.91	35.3	25.84
	C	1.82	8460	85.5	0.61	0.39	5.22	3.32	250.4	25.84
1411+43		3.20	43000	29.6	0.51*	0.41*	3.85*	3.09*	>276	57.33
1502+55		3.32	22000	7.2	0.74	0.25	5.53	1.87	276.5	60.65
1512+35		2.23	43000	16.8	0.48*	0.42*	4.03*	3.48*	>235	33.90
1521+43		2.17	22000	583.7	0.15	0.09	1.24	0.82	1861.9	32.65

Table 5.7: Parameters used for the magnetic field calculation for the non-BAL QSOs sample. In column 1 and 2 the sources and components are specified. Column 3 contains the redshifts. Column 4 and 5 present the highest frequency available to measure the source size and the relative flux density obtained. Columns 6-7 and 8-9 contain the major and minor axis of the source projected area in arcseconds and kpc respectively. Asteriks indicate the sources for which we could not obtain a deconvolved size so the beam size is used as an upper limit of the dimension. Columns 10 and 11 report the intrisinc magnetic fields and equivalent magnetic fields of the CMB calculated during this work respectively.

CMB-equivalent magnetic field

One relevant contribution to the electron energy losses is due to their interaction with the Cosmic Microwave Background (CMB). The photons of the CMB can in fact collide with the jet electron population gaining energy from them. This process takes the name of Inverse Compton Scattering and must be studied in this context in order to understand its importance in the quasar energetic balance. The energy loss by the particles per unit time can be written as follows:

$$-\frac{dE}{dt} = \sigma_T \gamma^2 c u_\gamma$$

where σ_T is the Thomson scattering constant and u_γ is the energy density of the photons in the region of interest. The former expression appears very similar to the synchrotron loss expression. To be able to compare quantitatively these two processes, one can think of associating to the photons energy density an equivalent magnetic field B_{eq}. In case of CMB photons one can write:

$$\frac{B_{CMB}^2}{8\pi} = u_{CMB}(1+z)^4$$

where the term $(1+z)^4$ takes into account the evolution of the CMB energy density with the redshift. Remembering that $u_{CMB} = 0.26\ eV/cm^3$ one can easily find B_{eq} (Murgia et al. 1999):

$$B_{CMB} = 3.25(1+z)^2\ \mu G$$

The importance of the CMB becomes higher for high redshifts. In particular, in case of weak sources, B_{CMB} can compete with the source intrinsic magnetic field.

Assuming hence the total magnetic field to be $B_{TOT} = B_{eq} + B_{CMB}$ we can write the spectral age formula as follows:

$$t_{syn}[Myr] = 1610 \cdot \frac{\sqrt{B_{eq}}}{\frac{2}{3}B_{eq}^2 + B_{CMB}^2} \cdot \frac{1}{\sqrt{(1+z)\nu_{break}}}$$

where B_{eq} and B_{CMB} are in νG and ν_{break} in GHz (Murgia et al. 1999).

As explained in Section 5.1.2, *SYNAGE* could only found a break frequency for 21 sources (13 BAL QSOs and 8 non-BAL QSOs) . For them we could calculate the spectral age using the equipartition magnetic field previously computed. In case of resolved sources we approximated B_{eq} to the mean value of the single components. Results of this computation are shown in Tab. 5.8.

ID	Comp	z	freq [MHz]	S [mJy]	Min.axis [arcsec]	Maj.axis [arcsec]	Min.axis [kpc]	Maj.axis [kpc]	B [μG]	B_{CMB} [μG]
1528+53		2.82	22000	15.1	1.06	0.82	8.30*	6.42*	>136	47.42
1554+30		2.69	43000	2.6	0.69	0.09	5.54	0.78	331.1	44.25
1634+32		2.34	43000	13.9	0.28	0.16	2.29	1.32	470.2	36.25
1636+35		1.91	22000	29.3	0.374	0.123	3.14	1.03	492.5	27.52
1641+33		2.75	22000	26.6	1.17	0.47	9.27	3.77	208.6	45.70
1728+56	A	1.77	22000	4.2	1.40	0.86	11.84	7.28	60.5	24.93
	B	1.77	22000	4.9	0.75	0.35	6.37	2.95	126.4	24.93
	C	1.77	22000	6.3	0.83	0.42	7.05	3.58	118.2	24.93
2109-07		1.88	8460	22.6	1.79	0.72	15.12	6.07	91.7	26.95
2129+00		2.96	43000	8.6	0.7	0.44	5.41	3.40	214.7	50.96
2143+00		2.04	43000	26.3	0.30	0.17	2.54	1.46	476.7	30.03
2238+00		3.47	1400	32.2	23.97	13.7	176.01	100.59	11.2	64.93
2244+00		2.95	43000	4.9	0.74	0.43	5.73	63.33	181.8	50.70
2248-09		2.11	8460	8.1	4.11	2.07	34.17	17.21	32.0	31.43
2331+01		2.64	22000	10.7	1.06	0.83	8.44	6.61	116.9	43.06
2346+00		1.78	43000	16.7	1.87	0.23	15.85	2.00	190.9	25.11
2353-00		1.89	43000	1.9	0.78	0.42	6.56	3.53	98.9	27.14

Tab. **??** Continued

ID	class	t_{syn} CI yr	t_{syn} CIOFF yr	t_{syn} JP yr	t_{syn} KP yr
$0044+00^*$	BAL	2.310^3	2.310^3	1.410^3	1.410^3
$0756+37^*$	BAL	1.110^3		2.110^3	
$0816+48^*$	BAL	5.110^2	3.110^2	3.910^2	3.910^2
0842+06	BAL	$< 4.610^5$		$< 2.510^5$	$< 2.510^5$
$1014+05^*$	BAL	$< 1.210^4$	$< 8.410^3$	$< 8.410^3$	$< 8.410^3$
1054+51	BAL	$< 1.510^6$		$< 2.310^6$	
$1102+11^*$	BAL	$< 4.010^3$		$< 6.910^3$	
1129+44	BAL	$< 6.110^5$			$< 1.610^6$
1159+06	BAL	$< 6.910^5$	$< 4.010^5$	$< 4.710^5$	$< 4.710^5$
1229+09	BAL	3.110^6	2.110^6	5.910^5	5.910^5
$1337-02^*$	BAL	1.410^6	3.510^5	4.710^5	4.710^5
1624+37	BAL	$< 2.010^5$	$< 1.210^5$	$< 1.610^5$	$< 1.610^5$
0154-00	non-BAL	$< 1.710^5$		$< 1.710^5$	$< 1.710^5$
0750+36	non-BAL	$< 3.510^5$	$< 2.110^5$	$< 2.710^5$	$< 2.710^5$
1005+48	non-BAL	1.310^5	7.110^4	7.810^4	7.810^4
1401+52	non-BAL	$< 2.610^5$	$< 1.910^5$	$< 2.010^5$	$< 2.010^5$
1528+53	non-BAL	$< 2.310^5$	$< 1.210^5$	$< 1.410^5$	$< 1.410^5$
1554+30	non-BAL	7.310^4	3.410^4	4.310^4	4.310^4
2244+00	non-BAL	1.210^5	7.710^4	8.810^4	8.810^4

Table 5.8: Computed spectral age for BAL and non-BAL sources with fitted break frequencies. Columns 3-6 indicate the different spectral ages (in unit of years) obtained by using different spectral models (CI, CIOFF, JP, KP). Upper limits are indicated when lower limits on magnetic fields are the only available information. Asterisks indicate the sources for which VLBI measurements have been used.

Discussion

The spectral analysis of both the BAL QSOs and the non-BAL QSOs sample confirms the variety of spectral shapes already found by Bruni et al. (2012). They in fact range from flat to steep power-laws, from purely transparent spectra to self-absorbed ones, to multiple components spectra. The derived magnetic fields are as expected of the order of tens or hundreds of microGauss reaching in the strongest cases peaks of 10 milliGauss. No plain differences in the magnetic field values have been recognized between the two samples. The synchrotron ageing analysis did not yield significant differences either. The computed radiative ages are a range comprised between 0.5 and 500 Kyr proving the youth of the source emission. As shown in Sec. 5.1.2 different spectral models have been used for the fitting and often we have obtained similar results in terms of χ^2 for all of them. Although in principle a CI model would probably match better these sources from a theoretical point of view, since they are expected to be active, we also found cases in which a JP or CIOFF model better described the trend. For a correct interpretation of these findings one always has to remember that, unfortunately, we do not have enough resolution to look at each single component and thus what we observe is a superposition of different electron population emissions. In this context a JP model fit (pure losses) should not be interpreted as indicative of a dying source, but probably only suggests that the dominant component in the total spectrum is a lobe structure which typically suffers from radiative losses. In any case we see from Tab. 5.8 that the final ages for each source do not differ greatly from one model to another.

In drawing any conclusion from this analysis one must be aware of the variety of uncertainties which are present and can sometimes significantly affect the resulting age. Despite that, some of these errors cannot be avoided because of our ignorance on the involved physics. The main assumptions made during the analysis are the equipartition condition and the source shape and size (which is arbitrarily supposed to be circular or elliptical with depth similar to one of the observed axis). Another source of uncertainty is the error in the determination of the break frequency from the fitting procedure. This is quite difficult to estimate in a way which goes beyond the pure mathematical error from the fit. A sensitive, although pessimistic, estimate of the goodness of the fitted break frequency could come from the number of available spectral points in the break region of the spectrum. In our cases this would lead unfortunately to a large error because of the lack of high frequency spectral points. This could be overcome by exploiting the capabilities of the new generation of broad-band instruments (e.g. JVLA) which allow an almost continuous spectral coverage leading to a much better constraint of the spectral shape.

In conclusion, for the time being, the derived ages should be only considered as indicative. More reliable results in this direction could be obtained by studying the source morphologies at VLBI resolutions and by increasing the spectral coverage at high frequency where the power drop has to be fitted. In any case, we can probably safely assert that, even with big errors the computed ages are representative of a set of significantly active and young sources.

5.2 Polarization

The study of the polarization state of radiation can give useful information about the environment of the source. The synchrotron emission from a population of electrons is characterized by a strong intrinsic degree of linearly polarized emission. Despite that, if the magnetic field is not uniform but presents dishomogeneities and turbulences, the linearly polarized radiation from different electrons tend to cancel reducing the net polarization degree to only few percent. When an electromagnetic wave goes through a magnetized plasma a phenomenon called *Faraday Rotation* can also take place. To explain that one can think of the linearly polarized wave as a composition of two circularly polarized waves, right and left respectively. Because of a slightly different refraction index, the two waves travel in the medium with different velocities. In this way, the relative phase between both components changes and the net effect is a progressive rotation of the plane of polarization. In order to study the importance of this effect one can measure the so-called *Rotation Measure* which actually describes the global capacity of a plasma to rotate the polarized vector. Note that this phenomenon alters the polarization plane but not the polarized intensity. When the medium is not homogeneous, the amount of Faraday rotation is different for each different Faraday depth, and the degree of polarisation diminishes in a phenomenon called depolarisation. One usually refers to *intrinsic depolarization* when it happens within the emitting source or to *external depolarization* when it occurs during the path from the source to the observer. For all these reasons the degree of polarization (m) of radiation tells us about the medium and the magnetic field condition within the emitting source.

Further instrumental effects can intervene in decreasing the polarized radiation: the *beam depolarization* and the *bandwidth depolarization*. The first one totally depends on the telescope resolution. In fact, when looking at an extended source which is not uniformly polarized on a smaller scale than the instrument resolving power, contributions coming from different regions within the source will sum up causing the final polarized flux density to appear less than the real one. Since this effect actually depends on the instrument capabilities, it cannot be avoided and nor corrected. The bandwidth depolarization occurs instead when the observing bandwidth is wide enough to have significant RM within the bandwidth. This also causes a decrease of the fractional polarization. In order to overcome this effect, one should prefer observations with multi-channel beckends.

As already discussed in Sec. 4.2.2 data collected using the JVLA were not reduced with success during this work because of technical problems. Future improvements of the CASA software will probably give us the possibility to better deal with the polarization calibration in the next future. For the time being we limit ourselves in presenting the Effelsberg results which unfortunately only consist in upper limits of the fractional polarization as shown in Tab. 5.9 and 5.10. For that, we cannot safely assert whether we are really looking at low-polarization sources or whether the data suffer one of the instrumental effects previously mentioned. Certainly the beam size at 2.7 GHz at the Effelsberg telescope is quite big (265 arcsec) thus, we cannot be sure not to be influenced by some beam depolarization.

Name	$m_{2.6}$	$m_{4.85}$	$S_{8.35}$	$S_{10.5}$
0044+00	<2.4			<16.1
0842+06	<5.1		<8.7	
0849+27	<3.8		<4.7	
0905+02	<1.7			
0929+37	<6.9			
1014+05	<6.3			
1054+51	<4.4			
1102+11	<3.9			
1129+44	<2.0			
1237+47	<2.3			
1304+13	<4.6			
1335+02	<1.8			
1337-02	<3.5			
1603+30	<5.0			
1624+37	<3.4			

Table 5.9: Measured polarization flux density upper limits for the BAL QSOs sample at 2.7 GHz with the Effelsberg telescope.

5.3 Variability

Nowadays AGN are known to be variable across the whole electromagnetic spectrum and it is often possible to see distinct flares in their flux density curves. Many campaigns are now active in various bands to measure and study the phenomenon. Typically short-term campaigns are preferred for high-frequency studies. X-ray and optical flares last indeed from some days to few months. When talking about radio variability instead, the time range broadens to periods of years. By studying the characteristics of the variability observed in different categories of AGN one can try to constrain the physics at the base of these events. The radio band is particularly interesting from this point of view because it is directly linked to the shock development in the jets. The main obstacle of this kind of studies is due to the difficulty of obtaining a complete multifrequency and multiepoch coverage for the sources of interest.

Evidence for quasar radio emission variability was first presented by Dent et al. (1965). Soon thereafter, astronomers began to investigate the phenomenon on bigger quasar sample confirming the findings of Dent et al. (1965). The first attempt of explaining the radio variability observed was made by Rees (1966) invoking relativistic effects within the emitting regions. Further models claimed that the variations were produced by a cloud of spherically and adiabatically expanding plasma emitting incoherent synchrotron radiation

Name	$S_{2.6}$	$S_{4.85}$	$S_{4.86}$	$S_{8.35}$	$S_{8.46}$	$S_{10.5}$
0029-09	<5.2					
0033-00	<7.0	<6.5	<14.9			
0103-11	<6.5		<4.3			
0152+01	<11.0			<42.5		
0154-00	<1.8					
0750+36	<1.5					
1333+47	<7.2					
1528+53	<1.6					
1554+30	<4.5					
1636+35	<2.3					
2129+00	<5.3					
2143+00	<5.2					
2331+01	<7.0					
2346+00	<3.8					
2353-00	<4.7		<7.9			

Table 5.10: Measured polarization flux density upper limits for the non-BAL QSOs sample at 2.7 GHz with the Effelsberg telescope.

(van der Laan 1966; Pauliny-Toth & Kellermann 1966). This kind of model succeeded in giving a qualitative description of many observed features but failed in predicting more quantitative details. At present the most validated scenario overcomes the too semplistic idea of expanding spherical cloud and explains radio flares as due to shocks propagating along the radio jets (Marscher & Gear 1985). These shocks would arise when a minor disturbance in the flow encounters a pressure gradient along the jet. Relativistic beaming effects are also thought to accentuate this variations in case the jet lies just along the observer's line of sight. A standard model which discusses the evolution of a flare must first of all consider a growth stage due to the shock formation and secondly a decay stage when expansion begins to dominate. Sometimes at an intermediate time a plateau can be considered during which energy losses almost compensate the energy gains. Unlike the decay phase which can easily be described with some expansion models, the earliest phase represents a real chellange for models because strongly dependent on the unknown physics of the jet. Moreover delays in frequency are also observed.

In this context, we exploit the multi-epoch observations available to perform a variability analysis comparing the flux densities obtained during this work with those measured by Bruni et al. (2012). As already mentioned in Chapter 3 Bruni et al. (2012) already went through this kind of analysis in their work. Here, we had the possibility to continue it, covering a much longer time interval. Moreover, two sources studied in this work

(1603+30, 1624+37) were also monitored by Montenegro-Montes et al. (2008, MM08) giving thus the possibility to broaden the time coverage reaching a maximum baseline of about 7 years. Details on the various observing campaigns are presented in Tab. 5.11

To perform comparisons between flux densities measured in different epochs one has first of all to define a criterion to follow. In literature many sorts of variability indices have been proposed to carry out this kind of study. Coherently with Bruni et al. (2012) we choose here the *fractional variability index* by Tornikoski et al. (2003):

$$Var_{\Delta S} = \frac{S_{max} - S_{min}}{S_{min}}$$

where S_{max} and S_{min} are the maximum and minimum radio flux densities measured in a time interval at a given frequency. This criterion is mostly appropriate to describe sources with few measurements collected over long intervals of time, with respect to other ones which are used to detect stochastic variability in large data-sets (Gaensler & Hunstead 2000). An estimate of the statistical significance of the source variability was calculated by using the σ_{Var} parameter, defined by Zhou et al. (2006):

$$\sigma_{Var} = \frac{|S_2 - S_1|}{\sqrt{\sigma_1^2 + \sigma_2^2}}$$

Where S_1 and S_2 are the radio flux densities relative to the first and second epoch and σ_1, σ_2 are the corresponding uncertainties.

To perform the comparisons a threshold has to be established, beyond which the source is actually considered intrinsically variable. Torniainen et al. (2005) propose that a source is variable if $Var_{\Delta_S} > 3$ and $\sigma_{Var} > 3$. Salerno et al. (2013) discuss however the possibility that this condition could be too strict to study this kind of objects. In fact, it implies that the observed flux densities have at least to quadruplicate over the elapsed time between the two observation. With this argumentation, they propose a borderline of $Var_{\Delta S} > 0.25$ for the fraction of sources showing $\sigma_{Var} > 4$. This limit corresponds to variations of the flux densities greater than 25%. In Tab. 5.16 we report the sources with significant variability.

As can be noticed by examining the values reported in Tab. 5.16, the most significantly variable sources do not show impressive variations despite the long time interval elapsed between the observations. Probably it is worth mentioning the case of 2331+01 (non-BAL) which, as already noted during the spectral analysis in Sec. 5.1.2, exhibits a systematic flux density decrease at all frequencies measured during this work, indipendently from the telescope as shown in Fig. 5.23. The same can be affirmed for source 2346+00 (see Fig. 5.24).

Regarding the two sources in common with MM08, which have the longest time baselines, we found the following results:

Date	Telescope	Frequency (GHz)	Reference
June-July-October 2005	Effelsberg	4.85, 8.35, 10.5	MM08*
June 2006	Effelsberg	2.6	MM08*
February-March 2006	VLA(A)	8.45, 14.5, 22.5, 43.5	MM08*
December 2007	Effelsberg	2.6, 4.85, 8.35, 10.5	Bruni et al.(2012)
September 2008	Effelsberg	2.6, 4.85, 8.35, 10.5	Bruni et al.(2012)
July 2009	Effelsberg	2.6, 4.85, 8.35, 10.5	Bruni et al.(2012)
July 2009	VLA (C)	1.4, 4.86, 8.46, 22.5, 43.3	Bruni et al.(2012)
March-April 2011	EVLA (B)	4.86, 8.46	this work
September 2011	Effelsberg	2.6, 4.85, 8.35, 10.5	this work
March 2012	Effelsberg	2.6	this work

Table 5.11: Summary of the observations. *Montenegro-Montes et al. (2008)

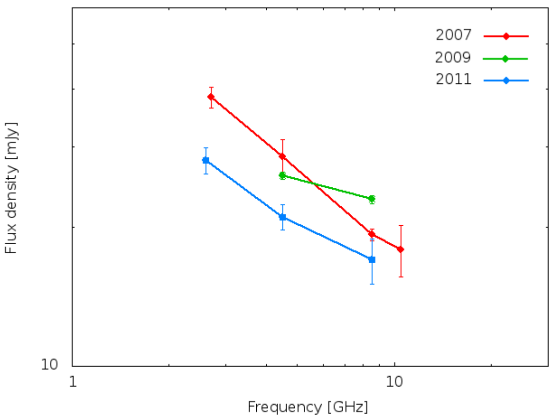

Figure 5.23: Radio variability of 2331+01

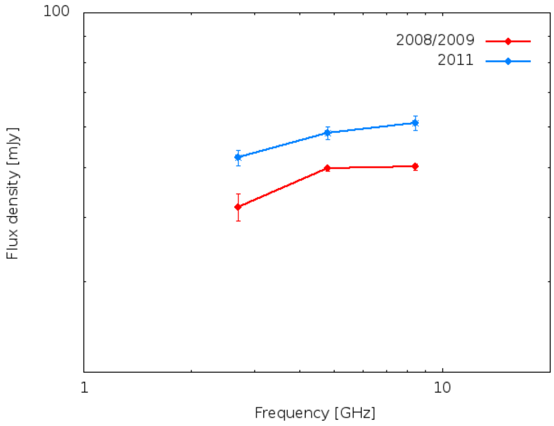

Figure 5.24: Radio variability of 2346+00

- For source 1603+30 we measured quite important variability as shown in Tab. 5.17. This trend is confirmed both by Bruni et al. (2012) and by MM08 who first indicated the source as variable (significance 4.2 and fractional variability 22%) performing comparisons between the flux densities from their data and those from Becker et al. (2000).

- For source 1624+37 we could only compare the 2.7 GHz flux density, confirming the stability observed by Bruni et al. (2012). The flux density at 2.7 GHz has actually changed by a negligible amount, i.e. from a value of $33.5 \pm 1.6 mJy$ measured in June 2006 to a value of $36.6 \pm 1.7 mJy$ measured in March 2012.

On the basis of the available data one can in conclusion assert that no strong signs of variability is observed for both BAL QSO sources and non-BAL sources. Indeed values

ID	$Var^{2.6}_{\Delta S}$	$\sigma^{2.6}_{Var}$	time	$Var^{4.85}_{\Delta S}$	$\sigma^{4.85}_{Var}$	time	$Var^{4.86}_{\Delta S}$	$\sigma^{4.86}_{Var}$	time
0044+00	0.02	0.39	3.6 yr				0.06	0.71	1.6 yr
0842+06	0.22	3.33	3.6 yr				0.19	6.65	1.6 yr
0849+27	0.09	1.67	3.6 yr						
0905+02	0.10	2.38	3.5 yr						
0929+37	0.03	0.36	2.8 yr				0.04	1.74	1.6 yr
1014+05	0.12	1.22	2.0 yr						
1054+51	0.003	0.03	4.2 yr						
1102+11	0.16	3.65	2.0 yr						
1103+11							0.11	1.50	1.6 yr
1129+44	0.03	1.07	4.2 yr						
1237+47									
1304+13	0.13	1.27	2.7 yr						
1327+03	0.02	0.65	3.6 yr				0.05	0.86	1.6 yr
1335+02	0.12	4.20	4.2 yr						
1337-02	0.02	0.48	2.0 yr				0.12	2.56	1.6 yr
1404+07							0.06	1.19	1.6 yr
1603+30	0.08	0.26	2.0 yr				0.01	0.26	1.6 yr
1624+37	0.03	0.37	4.2 yr						

Table 5.12: Fractional variability index and corresponding significance for the BAL QSO sample at 2.7 GHz, 4.5 GHz (Effelsberg) and 4.6 GHz (VLA).Comparisons refer to flux densities measured in Bruni et al. (2012) and in this thesis.

of $Var_{\Delta S}$ no greater than 0.37 have been measured but quite always with significance σ_{Var} lower than 4. None of the examined sources can be however classified as variable even considering the revised parameters by Salerno et al. (2013, submissed). The main difficulty in discussing such values is mainly linked to the possible interference of many external factors which can actually modify the flux density observed misleading the interpretation. First of all, differences in resolution and sensitivity between single-dish and interferometric telescopes should not be forgotten in the comparisons. Moreover going to higher frequencies we expect the weather to increase its negative influence on the observations thus modifying the astronomical signal. Despite that, it would probably be worthwile going on with the observational campaign in the next years in order to carry on the monitoring program. In fact, Salerno et al. (2013, submitted) find a small BAL QSOs fraction to be variable thus encouraging in continuing this kind of study.

ID	$Var^{8.35}_{\Delta S}$	$\sigma^{8.35}_{Var}$	time	$Var^{8.46}_{\Delta S}$	$\sigma^{8.46}_{Var}$	time	$Var^{10.5}_{\Delta S}$	$\sigma^{10.5}_{Var}$	time
0044+00				0.04	0.29	1.6 yr	0.30	1.49	3.6 yr
0842+06									
0849+27	0.01	0.25	3.6 yr						
0905+02									
0929+37				0.03	0.8	1.6 yr			
1014+05				0.11	1.55	1.6 yr			
1054+51									
1102+11				0.13	0.82	1.6 yr			
1103+11				0.13	0.78	1.6 yr			
1129+44									
1304+13									
1327+03				0.01	0.14	1.6 yr			
1335+02									
1337-02				0.10	1.24	1.6 yr			
1404+07				0.03	0.40	1.6 yr			
1603+30				0.01	0.4	1.6 yr			
1624+37									

Table 5.13: Fractional variability index and corresponding significance for the BAL QSO sample at 8.3 GHz, 10.5 GHz (Effelsberg) and 8.4 GHz (VLA). Comparisons refer to flux densities measured in Bruni et al. (2012) and in this thesis.

ID	$Var^{2.6}_{\Delta S}$	$\sigma^{2.6}_{Var}$	time	$Var^{4.85}_{\Delta S}$	$\sigma^{4.85}_{Var}$	time	$Var^{4.86}_{\Delta S}$	$\sigma^{4.86}_{Var}$	time
0029-09	0.23	2.56	2.0 yr				0.08	1.03	1.6 yr
0033-00	0.06	0.61	2.0 yr	0.62	3.36	2 yr			
0103-11	0.06	0.90	2.0 yr				0.08	1.08	1.6 yr
0152+01									
0154-00	0.009	0.50	2.8 yr						
0158-00							0.15	3.3	1.6 yr
0750+36							0.09	1.98	1.6 yr
1333+47							0.19	2.71	1.6 yr
1401+52							0.08	1.01	1.6 yr
1528+53	0.03	0.51	3.6 yr				0.09	1.17	1.6 yr
1554+30	0.26	2.60	2.0 yr				0.14	2.71	1.6 yr
1636+35	0.04	1.30	2.8 yr						
2129+00	0.16	2.42	3.6 yr				0.07	2.54	1.6 yr
2143+00	0.08	0.98	2.0 yr				0.03	1.04	1.6 yr
2331+01	0.37	3.86	3.6 yr				0.22	3.44	1.6 yr
2346+00	0.24	3.34	2.8 yr				0.17	5.09	1.6 yr

Table 5.14: Fractional variability index and corresponding significance for the non-BAL QSO sample at 2.7 GHz, 4.5 GHz (Effelsberg) and 4.6 GHz (VLA). Comparisons refer to flux densities measured in Bruni et al. (2012) and in this thesis.

ID	$Var^{8.35}_{\Delta S}$	$\sigma^{8.35}_{Var}$	time	$Var^{8.46}_{\Delta S}$	$\sigma^{8.46}_{Var}$	time	$Var^{10.5}_{\Delta S}$	$\sigma^{10.5}_{Var}$	time
0029-09	-	-	-	0.65	3.89	1.6 yr	-	-	-
0033-00	0.07	1.06	2.0 yr	-	-	-	-	-	-
0103-11	0.05	1.32	2.0 yr	-	-	-	-	-	-
0152+01	-	-	-	0.33	1.62	1.6 yr	-	-	-
0154-00	-	-	-						
0158-00	-	-	-	0.21	1.14	1.6 yr	-	-	-
0750+36	-	-	-	0.02	0.13	1.6 yr	-	-	-
1333+47	-	-	-	0.05	0.42	1.6 yr	-	-	-
1401+52	-	-	-	0.14	1.53	1.6 yr	-	-	-
1528+53									
1554+30	-	-	-	0.05	0.44	1.6 yr	-	-	-
1636+35									
1728+56	-	-	-	0.07	0.96	1.6 yr	-	-	-
2129+00	-	-	-	0.22	5.81	1.6 yr	-	-	-
2143+00	-	-	-	0.25	6.98	1.6 yr	-	-	-
2331+01	-	-	-	0.35	3.05	1.6 yr	-	-	-
2346+00	-	-	-	2.29	20.61	1.6 yr	-	-	-

Table 5.15: Fractional variability index and corresponding significance for the non-BAL QSO sample at 8.3 GHz, 10.5 GHz (Effelsberg) and 8.4 GHz (VLA). Comparisons refer to flux densities measured in Bruni et al. (2012) and in this thesis.

ID	2.7 GHz				4.5 GHz				8.5 GHz			
	S_1	S_2	σ_{Var}	$Var_{\Delta S}$	S_1	S_2	σ_{Var}	$Var_{\Delta S}$	S_1	S_2	σ_{Var}	$Var_{\Delta S}$
0842+06	45.7	37.2	3.33	0.22	29.5	24.7	6.65	0.19	-	-	-	-
1335+02	96.9	86.5	4.20	0.12	-	-	-	-	-	-	-	-
0029-00	33.5	41.1	2.56	0.23	38.6	41.9	1.03	0.08	-	-	-	-
2129+00	33.2	38.7	2.42	0.16	32.8	30.4	2.54	0.07	27.4	22.4	5.81	0.22
2331+01	38.4	28.0	3.86	0.37	25.9	21.1	3.44	0.22	23.0	17.0	3.05	0.35
2346+00	41.9	52.2	3.34	0.24	49.7	58.4	5.09	0.17	50.1	61.0	5.06	0.21

Table 5.16: Sources showing the most significant variability associated to the highest significances. S_1 stands for the flux density observed in the more distant epoch by Bruni et al. (2012) while S_2 represents the more recent one reduced during this work.

Frequency (GHz)	S_1	S_2	σ_{Var}	$Var_{\Delta S}$	Elapsed time (yr)
2.7	22.8 ± 1.7	31.7 ± 1.7	3.6	0.39	5.4
4.6	26.1 ± 0.7	35.1 ± 0.9	7.83	0.23	6.5
8.4	22.1 ± 0.3	27.3 ± 0.8	6.1	0.24	5.1

Table 5.17: Variability parameters for source 1603+03 calculated comparing flux densities by MM08 (S_1) and the ones measured during this thesis (S_2). 2.7 GHz flux densities are from Effelsberg single dish and 4.6, 8.4 GHz are from VLA/JVLA.

Chapter 6

Conclusions

Since their discovery, Broad Absorption Line Quasars (BAL QSOs) represent a great challenge in the context of the Active Galactic Nuclei (AGN) unified model. At present in fact, none of the ongoing studies is able to point out the key argument to justify their difference with respect to the normal quasar population.

In this thesis we tried to shed some light on their nature investigating the spectral shapes and ages, as well as the variability properties of a sample of radio-loud BAL QSOs selected by Bruni et al. (2012). To do that we combined measurements from literature with those collected by the multi-frequency observational campaign by Bruni et al. (2012), as well as new data reduced during this thesis. With this work we aimed at finding any indication which could give support to one of the two mostly accepted interpretative scenarios: the orientation and the evolutionary scenario. The main investigations are here briefly summarized.

- The spectral analyses of both the BAL QSO and the non-BAL QSOs sample confirm the variety of spectral shapes already found by Bruni et al. (2012). They range from flat to steep power-laws, from purely transparent spectra to self-absorbed ones, to multiple component spectra. These heterogeneous findings do not particularly support any of the previously mentioned scenarios. Indeed, different spectral shapes are indicative of both heterogeneous orientations and ages. Moreover, spectral components at low frequencies, which are sometimes found, also suggest the presence of a more extended and older component drawing the line at the source total age. One should remember though that the sources can also have experienced a recurrent radio activity thus it is well possible that an older component can be present associated to a younger one.

- The derived magnetic fields resulted, as expected, of the order of tens or hundreds of microGauss reaching in the strongest cases peaks of about 10 milliGauss. No plain differences in their values have been recognized between the two samples suggesting similar physical conditions.

- For 12 BAL QSOs and 7 non-BAL QSOs the spectral fitting determined a break frequency allowing us to compute the spectral ages of the source. The synchrotron ageing analysis did not yield though significant differences either. The computed radiative ages are all in the range between 0.5 to 500 Kyr for both samples. Compared with the typical age of an old radio-source (tens of Myr), the computed ages are representative of a rather young class of sources. It is wortwhile noting that among all sources, the smallest ages (0.5-1 Kyr) have been found for some BAL QSOs when using VLBI measurements. This suggests that an instrumental bias could be present and we cannot exclude that VLBI observations of non-BAL QSOs could lead to the same values. However, the two classes of object do not present clear differences in their age distribution. The main limits of our ageing results often lie in a too thin spectral coverage, especially at the highest frequencies, affecting the goodness of the spectral fits from which the break frequency information is extracted. These problem could be overcome in the next future by exploiting the capabilities of the new generation of broad-band instruments (e.g. JVLA, LOFAR) which allow an almost continuous spectral coverage leading to a much more easy and reliable spectral fitting. Moreover, instruments like ALMA, which operate in the millimeter regime, could be an interesting opportunity to improve the coverage of the highest spectral tail of the spectrum. They could actually help also in recognizing the break frequency for sources which show a power-law trend up to high frequencies. Moreover, the lack of VLBI information did not allow a precise spectral study for each source component, restricting our analysis to the global power spectrum. A significant contribution to the source understanding would then come by increasing the morphological information at VLBI resolutions.

- The variability analysis also did not point out substantial discrepancies between the two samples. All sources show very low flux densitiy variations even over periods of several years suggesting that a polar orientation should not be dominant in our samples. Moreover, the two samples do not appear, also from this point of view, so much different. Despite that, it would probably be worthwile going on with the observational campaign in the next years in order to carry on the monitoring program. In fact, Salerno et al. (2013, submitted) find a small BAL QSOs fraction to be variable.

- Thanks to our new EVLA data, during this work, we also had the possibility to test some of the most recent routines of the CASA software to obtain the polarization measurements. To this day, some technical problems prevented us from completing

> the calibration procedure. Future improvements of the software will give us the possibility to conduct further scientific investigations on this topic.

Summarising, the analysis performed in this work on both the BAL QSO and the non-BAL QSOs seems to be in accordance with the majority of recent works which suggest that a combination of evolution and orientation is likely at work, rather than one simple scenario. The BAL phenomenon could probably be present at different stages of the QSO activity, both in the radio-loud and radio-quiet phase, but seen only when the outflows intercept the line of sight of the observer. These outflows could probably be generated from the accretion disk and arise with different orientations. In the end, one can probably assert that, given the variety of observational properties, BAL quasars do not seem to be a well-defined subsample of objects. Despite that, clear indications to solve the BAL nature are still missing.

References

Adelman-McCarthy, J.K., Agueros, M.A., Allam, S.S. et al. 2007, AJ Supplement Series, 172, 2, 634 ApJ, 479, L93+

Arav, N. & Li, Z. 1994, ApJ, 427:700-707

Arav, N., Li, Z., Begelman, M.C. 1994, ApJ, 432:62-74

Baars, J.W.M., Genzel, R., Pauliny-Toth, I.I.K. et al. 1977, A&A, 61, 99

Becker R. H., Gregg M. D., Hook I. M., McMahon R. G., White R. L., Helfand D. J., 1997, ApJ, 479, L93+

Becker, R. H., White, R. L. & Helfand, D. J. 1995, ApJ, 450, 559

Becker, R.H., White, R.L., Gregg, M.D. et al. 2000, ApJ, 538, 72

Bengelman, M.C., De Kool,M., Sikora,M., 1991, Apj, 382:416-432

Bolton, R. C.., et al. 2004, MNRAS, 354, 485

Briggs, F. H., Turnsheck, D. A. & Wolfe M. 1984, ApJ, 287, 549

Bruni G., Mack K.-H., Salerno E., et al., 2012, A&A, ||||||||

Cano-Díaz,M., Maiolino,R., Marconi,A. et al. 2012, A&A 537, L8

Cohen, A.S., Lane, W.M., Cotton, W.D. et al. 2007, AJ, 134, 1245

Condon, J. J., Cotton, W. D., Greisen, E.W. et al. 1998, AJ, 115, 1693

Crenshaw, D.M., Kraemer, S.B. & George, I.M., 2002, "Mass outflow in AGN: new perspectives", ASP conference Series, vol. 255

de Kool, M., Begelman, M. C. 1995, ApJ, 455:448-455

de Kool, M., 1997, in "Mass Ejection from Active Galactic Nuclei", ASP Conference Series, vol. 128, p. 233

Di Matteo, T., et al., 2005, Nature, 433,604

DiPompeo, M.A., Brotherton, M.S., De Breuck, C. 2012, Draft version

Douglas, J.N., Bash, F.N. & Bozyan, F.A. 1996, AJ, 111, 5, 1945

Dunn, J. P., Arav, N. et al. 2012, ApJ, 750:143 (8pp)

E. Wright & R. Otrupcek 1990

Elvis, M., Wilkes, B.J., McDowell, J.C. et al. 1994, ApJS, 95, 1

Elvis, M. 2000, ApJ, 545, 63

Emmering, R.T., Blandford, R.D., Shlosman, I., 1992, Apj, 385:460-477

Fanaroff, B.L. & Riley, J.M., 1974, MNRAS, 167, S.C., 31

Ficarra, A., et al. 1985, A&AS, 59, 255

Ghosh, K.K. & Punsly, B. 2007, ApJ, 661, 139

Gregory, P. C., et al. 1996, ApJS, 103, 427

Hales, S. E. G., et al. 1988, MNRAS, 234, 919

Hall, P. B., Anderson, S. F., Strauss, M. A. et al. 2002, ApJS, 141, 267

Hewett, P.C. & Foltz, C.B. 2003, AJ, 125, 1784

Hovatta T., Tornikoski M., Lainela M., Lehto H.J. et al., 2007 A&A, 469, 899

Klein, U., Mack, K.-H., Gregorini, L. et al. 2003, A&A, 406, 579

Knigge,C., Scaringi,S., Goad,M.R., & Cottis, C.E., 2008, Mon. Not. R. Astron. Soc. 386, 1426Ű1435

Korista, K., Hamann, F. et al. 1996, ApJ, 461:641-656

Konigl, A. & Kartje, J. F. 1994, ApJ, 434:446-467

Large, M. I., et al. 1991, Observatory, 111, 72

Larionov, M. G., et al. 1994, A&AS, 106, 119

Lawrence, C. R., et al. 1983, ApJS, 51, 67

Lipari, S.L. & Terlevich, R.J. 2006, MNRAS, 368, 1011

Moe, M., Arav, N. et al. 2009, ApJ, 706:525Ű534

Montenegro-Montes, F.M., Mack, K.-H., Benn, C. et al. 2008b, PoS (IX EVN Symposium) 019

Montenegro-Montes, F.M., Mack, K.-H., Vigotti, M. et al. 2008a, MNRAS, 388, 1853

Munro, R. E. B., 1971b, Australian J. Phys., 24, 617

Murgia,M., Fanti, C., Fanti, R., Gregorini, L., Klein,U., Mack,K.H., & Vigotti,M., 1999 A&A 345, 769Ű777

Murray, N., Chiang, J., Grossman, S.A., Voit, G.M., 1995, ApJ, 451, 498

Proga D., Stone J. M., Kallman T. R., 2000, ApJ, 543, 686

Punsly, B. 1999a, ApJ, 527, 609

Punsly, B. 1999b, ApJ, 527, 624

Rengelink R. B., Tang Y., de Bruyn A. G. et al., 1997, A&AS, 124, 259

Riley, J. M., et al. 1999a, MNRAS, 306, 31; 1999b, MNRAS, 307, 293

Sanders D. B., Soifer B. T., Elias J. H., Neugebauer G., Matthews K., 1988, ApJ, 328, L35

Schneider, D.P., Hall, P. B., Richards, G. T. et al 2007, AJ, 134, 102

Stocke, J.T., Morris, S.L., Weymann, R.J. et al. 1992, ApJ, 396, 487

Voit,G.M., Weymann,R.J., Korista,K.T., 1993, Apj, 413:95-109

Weymann, R.J., Morris, S.L., Foltz, C.B. et al. 1991, ApJ, 373, 23

Wills, B.J. 2009 ASP Conference Series, Vol. 419

Wright, A. E., Griffith, M. R., Burke, B. F., & Ekers, R. D. 1994, ApJS, 91, 111

Wright, A., E., et al. 1996, ApJS, 103, 145

Wu, K. K.S., et al., 2000, MNRAS, 318,889

Zhang, X., et al. 1997, A&AS, 121, 59

Zhou, H., Wang, T., Wang, H. et al. 2006, ApJ, 639, 716